CENTER FOR RADAR ASTRONOMY

STANFORD ELECTRONICS LABORATORIES
DEPARTMENT OF ELECTRICAL ENGINEERING
STANFORD UNIVERSITY · STANFORD, CA 94305

RADIO SCINTILLATIONS OBSERVED DURING ATMOSPHERIC OCCULTATIONS OF VOYAGER: INTERNAL GRAVITY WAVES AT TITAN AND MAGNETIC FIELD ORIENTATIONS AT JUPITER AND SATURN

by

David P. Hinson

November, 1983

Scientific Report No. D208-1983-1

Prepared under
Jet Propulsion Laboratory contract JPL 953618 and
NASA grant NGL 05-020-014

RADIO SCINTILLATIONS OBSERVED DURING ATMOSPHERIC OCCULTATIONS OF VOYAGER: INTERNAL GRAVITY WAVES AT TITAN AND MAGNETIC FIELD ORIENTATIONS AT JUPITER AND SATURN

By

David P. Hinson

November, 1983

Center for Radar Astronomy

Stanford Electronics Laboratories

Stanford University, CA 94305

The material in this report originally was submitted to the Department of Electrical Engineering of Stanford University as a dissertation fulfilling a requirement for the degree of Doctor of Philosophy. Additional copies can be obtained from the Center for Radar Astronomy or University Microfilms, Ann Arbor, Michigan. The research was supported by the Voyager Project, and the NASA Office of Space Science under grants NGL 05-020-014 and NAGW 152.

ABSTRACT

The exploration of the outer solar system using Voyagers 1 and 2 included dual-wavelength radio observations during occultations of the spacecraft by Jupiter, Saturn, and Titan. One of several areas of research based on these observations involves the way that refractive irregularities in the atmospheres of these planets caused amplitude and phase scintillations at both wavelengths (3.6 and 13 cm).

A new technique has been developed and applied in order to objectively analyze the radio scintillations observed during planetary occultations of Voyager. In this method, temporal spectra of the weak fluctuations in amplitude and phase are interpreted using the theory for scattering from a random distribution of anisotropic irregularities embedded in a thin screen. Comparisons between measured spectra and the theory produce least-squares solutions for four parameters which characterize the underlying atmospheric scattering structures: (1) the axial ratio, (2) the orientation, (3) the power-law exponent of the spatial spectrum, and (4) the magnitude of the spatial variations in refractive index. The covariance matrix of the solutions is calculated by propagation of errors.

For Jupiter and Saturn, this study considers only data pertaining to irregularities in the upper ionospheres. At both planets, scattering was observed from irregularities of approximate size 2 to 100 km. Within this size interval, the three-dimensional spatial spectrum obeys an inverse power law; further, all observed irregularities appear to be anisotropic. Magnetic field orientations in the ionospheres of Jupiter and Saturn were inferred from the direction of alignment of the

irregularities. The occultation measurements conflict with the predictions of Jovian magnetic field models, but generally confirm current models of Saturn's field.

During the occultation of Voyager 1 by Titan, refractive irregularities of size 0.2 to 2 km distributed throughout the lowest 90 km of the atmosphere caused appreciable signal fluctuations. Analysis of measured spectra yielded evidence of horizontal variations in gas density, and hence dynamics. Above 25 km, the altitude profile of intensity scintillations closely agrees with the predictions of a theory based on the characteristics of freely propagating internal gravity waves. These observations confirm the presence on Titan of atmospheric gravity waves, possibly driver by a convective region near the surface. The net upward flux of wave energy is approximately $2 \cdot 10^{-3}$ W m^{-2} -- too small to affect the thermal structure of Titan's lower atmosphere. An upper bound on the net upward flux of horizontal momentum is roughly $3 \cdot 10^{-3}$ N m^{-2}; the transport of momentum by gravity waves could be important in maintaining the zonal stratospheric circulation.

ACKNOWLEDGMENT

I am indebted to G. L. Tyler for the guidance and support that he patiently provided throughout many years while supervising this research. I gained valuable insight through numerous discussions with V. R. Eshleman, who also offered many useful comments as the second reader of this manuscript. B. K. Reid served as the third reader.

My progress toward understanding Titan's atmosphere was greatly assisted by G. F. Lindal, who supplied the results of his analysis of the vertical structure of the neutral atmosphere. I also thank N. F. Ness for helpful discussions concerning the magnetic fields of both Jupiter and Saturn. The efforts of D. N. Sweetnam, R. A. Simpson, M. A. Plume, and F. A. Orabona toward data analysis simplified my task. Finally, the members of the Voyager Radio Science Team and the personnel of the NASA Deep Space Network deserve considerable credit for successfully obtaining these data.

This work was supported by the Voyager Project, and by the NASA Office of Space Science under grants NGL 05-020-014 and NAGW 152.

TABLE OF CONTENTS

ILLUSTRATIONS

TABLES

SYMBOLS

$A(t)$	amplitude of the signal received at time t during a radio occultation experiment
$a(t)$	normalized version of $A(t)$ (see equation 3.1)
$B_\chi(\vec{r}_1,\vec{r}_2)$	spatial autocovariance of log-amplitude, $\chi(\vec{r})$, at positions $\vec{r}_1$ and $\vec{r}_2$ (see equation A9)
$B_\phi(\vec{r}_1,\vec{r}_2)$	spatial autocovariance of phase, $\phi(\vec{r})$, at positions $\vec{r}_1$ and $\vec{r}_2$ (see equation A10)
$B_{\chi\phi}(\vec{r}_1,\vec{r}_2)$	spatial cross covariance of $\chi(\vec{r})$ and $\phi(\vec{r})$ at positions $\vec{r}_1$ and $\vec{r}_2$ (see equation A11)
$B_n(\xi,\eta,\zeta)$	spatial autocovariance of refractive index, $n(\vec{r})$; B_n is assumed to be locally homogeneous so that it depends only on the vector separating the observation points (see equation A12)
$\vec{B}$	planetary magnetic field
$C_{aa}(f_k)$	measured discrete spectrum of fluctuations in a(t) at sample frequency f_k (see equation 3.2a)
$C_{\phi\phi}(f_k)$	measured discrete spectrum of fluctuations in $\phi(t)$ at sample frequency f_k (see equation 3.2a)
$C_{a\phi}(f_k)$	measured discrete cross spectrum of fluctuations in a(t) and $\phi(t)$ at sample frequency f_k (see equation 3.2b)
$C_{ii}(f_k)$	measured discrete spectrum of fluctuations in i(t) at sample frequency f_k
D	distance between the spacecraft and the visible limb of the occulting planet (see Figures A1 and D1)
d, e, f	numerical factors that determine the degree of anisotropy of the scattering irregularities (see equation 2.3)
$\vec{E}_o(\vec{r})$	complex electric field in the absence of scattering effects during a radio occultation experiment

$\vec{E}_s(\vec{r})$	complex electric field due to scattering during a radio occultation experiment
$E'(\vec{r})$	normalized scalar version of $\vec{E}_s$ (see equation A8)
e/f	axial ratio of scattering irregularities (see discussion following equation 2.3)
f(t)	frequency of the signal received at time t during a radio occultation experiment
$\vec{g}$	gravitational acceleration
g	magnitude of $\vec{g}$
g_3^o	axisymmetric octupole coefficient in a spherical harmonic representation of a magnetic field
H	atmospheric scale height
I(t)	intensity of the signal received at time t during a radio occultation experiment
i(t)	normalized version of I(t) (see equation 3.4)
k	free-space radio wavenumber; $2\pi/\lambda$
L	thickness of scattering volume (see Figure A1)
ℓ	dimension of the smallest irregular structure that contributes appreciably to $\vec{E}_s$ (within signal-to-noise limitations)
$N_e(\vec{r})$	number density of free electrons at position $\vec{r}$
$\delta N_e(\vec{r})$	spatial variation of $N_e(\vec{r})$ away from the local average value
$n(\vec{r})$	refractive index at position $\vec{r}$
$n_o(r)$	local average value of $n(\vec{r})$; assumed to be spherically symmertical
$n_t(\vec{r})$	spatial variation of $n(\vec{r})$ away from $n_o(r)$ due to turbulence or waves
p	inverse power-law exponent of Φ_n (see equation 2.3 or A17)

Q	normalization constant of Φ_n that is proportional to the variance of refractive index, $\langle n_t^2 \rangle$ (see equation 2.3)
$R_\chi(\tau)$	temporal covariance of fluctuations in χ with time delay τ (see equation A29)
$\vec{r}$	position vector referred to the center of the occulting planet
r	magnitude of $\vec{r}$
T	temperature, Kelvin
δT	temperature fluctuation associated with atmospheric waves
t	time
δt	time interval between discrete samples
u_h, u_v	horizontal and vertical components, respectively, of fluid velocity associated with atmospheric waves
v_y, v_z	components of spacecraft velocity that are perpendicular to the direction to earth
$\vec{v}_\star$	transverse raypath velocity in the phase screen (see Figures 2.1 and 2.2)
$v_\star$	magnitude of $\vec{v}_\star$
$w_\chi(\omega)$	theoretical spectrum of fluctuations in log-amplitude, χ, at frequency ω (see equations A30, A36, and A41)
$w_\phi(\omega)$	theoretical spectrum of fluctuations in phase, ϕ, at frequency ω (see equations A37 and A42)
$w_{\chi\phi}(\omega)$	theoretical cross spectrum of fluctuations in χ and ϕ at frequency ω (see equations A38 and A43)
$w_i(\omega)$	theoretical spectrum of fluctuations in intensity, $i(t)$, at frequency ω (see equation A49)
x, y, z	Cartesian components of $\vec{r}$; see Figures 2.1 and 2.2 and Section A.4 for definitions of coordinates

Γ	magnetic field orientation (see Figure 6.1)
γ	orientation of $\vec{v}_*$ in phase-screen coordinates (see Figures 2.1 and 2.2)
Δ	orientation of $\vec{v}_*$ with respect to $\vec{r}$ at ray periapsis as viewed from earth (see Figure 6.1)
θ	potential temperature
$\vec{\kappa}$	wave vector of refractive irregularities (see equation A12)
κ	magnitude of $\vec{\kappa}$
κ_x, κ_y, κ_z	Cartesian components of $\vec{\kappa}$
κ_0	wave number corresponding to the outer scale of refractive irregularities
$\vec{\kappa}_\perp$	component of $\vec{\kappa}$ that is perpendicular to the path of radio-wave propagation
λ	free-space radio wavelength
ξ, η, ζ	Cartesian components of the spatial separation of the observation points for covariance functions
Π	parameter characterizing the static stability of an atmosphere (see equation 7.2)
ρ	mass density of a quiescent atmosphere
$\delta\rho$	density fluctuation associated with atmospheric waves
σ_i^2	variance of normalized intensity i(t)
σ_r^2	residual of fit of theory to measured spectrum (see equation 3.5)
$\Phi_n(\kappa_x,\kappa_y,\kappa_z)$	three-dimensional spectrum of spatial variations in refractive index (see equations 2.3 and A12)
$\phi(t)$	phase of the signal received at time t during a radio occultation experiment
$\phi(\vec{r})$	spatial function of signal phase during a radio occultation experiment (see equation A8)

ϕ_y, ϕ_z	factors that determine the fractional intensity in a radio occultation experiment (see Appendix D)
$\chi(\vec{r})$	log-amplitude of a signal during a radio occultation experiment (see equation A8)
ψ	orientation of anisotropic refractive irregularities in the neutral atmosphere (see Figure 2.3)
ω	angular frequency of fluctuations in signal amplitude and phase
ω_c	break frequency in $w_\chi(\omega)$ (see equation C6)
$\langle\ \rangle$	angle brackets denote statistical averages or time averages, as appropriate

CHAPTER 1

INTRODUCTION

1.1 Background

Following their launch in 1977, the two Voyager spacecraft successfully explored the Jovian and Saturnian systems. Kohlhase and Penzo [1977] previously described the overall mission objectives, while Stone and Lane [1979a, b] and Stone and Miner [1981, 1982] summarized the preliminary results. Of interest here are several aspects of the experiments conducted through use of microwave radio signals transmitted by the spacecraft, and received on the earth.

A number of properties of a planetary atmosphere can be measured by the radio occultation method, using the radio link between the earth and a spacecraft which is occulted by the planet. (For a detailed discussion of this measurement technique and its potential, see Eshleman [1973].) For this reason, the Voyager missions to the outer planets included radio occultations of both spacecraft by Jupiter and Saturn, and a Voyager 1 occultation by Titan [Eshleman et al., 1977]. Through analysis of the dual-wavelength (3.6 and 13 cm) radio data from the Voyager occultations by Jupiter, Eshleman et al. [1979b, c] and Lindal et al. [1981] deduced altitude profiles for several quantities which characterize the atmosphere. These include the gas refractivity, molecular number density, pressure, temperature, and microwave absorption in the neutral atmosphere, as well as the average electron density in the ionosphere. Using data from subsequent Voyager occultations, Tyler et al. [1981a, 1982] derived analogous, though preliminary, results for Saturn's atmosphere and ionosphere. Analysis

of the effect of Titan's atmosphere on the two radio signals transmitted by Voyager 1 produced detailed altitude profiles for the neutral atmosphere, and showed that there was neither a detectable free electron density in the ionosphere nor perceptible microwave absorption by atmospheric gases [Tyler et al., 1981a; Lindal et al., 1983]. These results all pertain to the average structure of the planetary atmospheres.

During each Voyager occultation, the radio receiver moved through the diffraction pattern associated with refractive irregularities in the occulting planet's atmosphere. Rapid signal fluctuations occurred at both wavelengths as a result. These ubiquitous scintillations are a distinctive feature of the Voyager occultation measurements, and thus are incentive to further study. Consequently, the present research was directed toward a primary objective -- to infer characteristics of the atmospheric structures through analysis of the weakly-scattered radio signals. To anticipate the principal results, properties of the refractive irregularities were determined from the occultation data, and yielded new constraints for models of the Jovian and Saturnian magnetic fields, as well as a first-order characterization of small-scale dynamics in the atmosphere of Titan.

Scintillations are commonly observed during occultations of spacecraft radio sources by planetary atmospheres [for example, see Woo et al., 1980a, or Woo and Yang, 1978], and are also a persistent feature of stellar occultations [for example, see French et al., 1983, or Elliot, 1979]. Despite significant progress in developing a theory for weak scattering by atmospheric irregularities [Haugstad 1978a, b, 1979; Hubbard et al., 1978], prior to this study there existed no systematic

and objective procedure for applying the theory toward analysis of the signal fluctuations. Consequently, this research was motivated by a second important objective -- to establish a rigorous methodology for attacking this type of problem.

1.2 Organization

After a discussion of the refractive index of planetary atmospheres at microwave frequencies, Chapter 2 proposes physical models for the refractive irregularities in the ionosphere and neutral atmosphere. These models serve to characterize the atmospheric scattering structures, and are used subsequently to compute theoretical scintillation spectra for comparison with the Voyager occultation measurements. In order to complete the development of the theory, Appendix A derives the formulas for weak scattering of microwaves from a slightly irregular refracting atmosphere. The results in Appendix A are not original, but are included for convenience and as background for subsequent discussions. Appendix B establishes the limit of validity for the single-scattering results, and Appendix C provides a physical interpretation of the mathematical formulas.

Chapter 3 describes a new technique for systematically analyzing and interpreting the radio scintillations observed during planetary occultations. Through use of conventional methods of spectral data analysis and the existing weak-scattering theory, this procedure yields least-squares solutions for parameters which characterize the atmospheric scattering structures. The covariance matrix of the solutions is calculated by propagation of errors in order to evaluate the measurement uncertainties; as demonstrated in Appendix E, these uncertainties are realistic and not simply formal.

This new procedure was applied in processing the dual-wavelength data from the Voyager radio occultations by Jupiter, Saturn, and Titan. Chapters 4 and 5 report new results concerning the plasma irregularities in the upper ionospheres of Jupiter and Saturn. In Chapter 6, the measured orientation of the irregularities is used to infer the magnetic field direction at several locations in the ionospheres of these two planets; the occultation measurements are compared with the predictions of current Jovian and Saturnian field models. On the basis of evidence derived from the Voyager 1 occultation data, Chapter 7 reports the discovery of internal gravity waves in Titan's upper atmosphere. Wave parameters, including the vertical fluxes of energy and momentum, are estimated, and the source of the gravity waves is considered.

Finally, Chapter 8 summarizes the results and provides suggestions for future research.

1.3 A Note on Terminology

The conventional terminology for atmospheric waves is somewhat confusing; a comment on the notation used here is therefore in order. In conformity with common usage in the literature, atmospheric waves in which gravity provides the predominant restoring force will be referred to as "internal gravity waves." These waves are not confined to any fluid interface, but instead propagate freely through the atmosphere. Gossard and Hooke [1975, pp. 13-14] discuss the terminology in detail, and offer the more descriptive phrase "buoyancy waves" in referring to this type of fluid motion. It should be emphasized that the atmospheric waves considered here are unrelated to the gravitational radiation predicted by the general theory of relativity.

1.4 Contributions

The contributions by the author in the course of this research can be summarized as follows.

(1) An objective procedure was developed for systematically analyzing the signal fluctuations observed during planetary occultations. This new approach is more accurate and complete than previous methods.

(2) When applied to the Voyager radio occultation data, this procedure yielded new results concerning the morphology of Jupiter's ionospheric irregularities. Furthermore, the magnetic field orientation in the ionosphere was inferred from the alignment of anisotropic plasma structures. These occultation measurements were compared with the predictions of current Jovian magnetic field models; significant discrepancies were found.

(3) New results concerning Saturn's ionosphere and magnetic field, analogous to those at Jupiter, were derived from the Voyager radio occultation data. However, in this case, the inferred magnetic field orientations corroborate present Saturnian field models.

(4) Through analysis of the Voyager 1 radio occultation data, freely-propagating internal gravity waves were discovered in the upper atmosphere of Titan. Gravity-wave parameters, including the vertical fluxes of energy and momentum, were estimated. These results were applied to assess the importance of dynamics in determining the average thermal structure and circulation of Titan's atmosphere.

CHAPTER 2

MODELS FOR REFRACTIVE IRREGULARITIES IN PLANETARY ATMOSPHERES

2.1 Introduction

During each of the Voyager radio occultations by Jupiter, Saturn, and Titan, signal fluctuations occurred at both wavelengths as a result of scattering from refractive irregularities in the atmospheres of these planets. With the objective of constructing a theory for interpretation of these data, this chapter discusses the refractive index of atmospheres at microwave frequencies (Section 2.2), and proposes physical models for the refractive irregularities in the ionosphere (Section 2.3.1) and in the neutral atmosphere (Section 2.3.2). These models contain five free parameters which characterize the morphology of the scattering structures. When combined with the formulas in Appendix A, the models provide a basis for computing theoretical scintillation spectra. In later chapters, measured spectra are compared with the theory in order to determine solutions for the free parameters.

2.2 The Refractive Index of Planetary Atmospheres at Microwave Frequencies

As discussed in Appendix A, the radio frequencies used for the Voyager occultations (2295 MHz and 8415 MHz) are much larger than the electron gyrofrequency, the plasma frequency, and the electron collision frequency in the ionosphere of Jupiter or Saturn.

In this case, the refractive index $n(\vec{r})$ in the ionosphere is related to the electron density through [Eshleman, 1973]

$$n(\vec{r}) = 1 - N_e(\vec{r}) \cdot V_e = 1 - N_e(\vec{r}) \frac{r_e \lambda^2}{2\pi} \quad . \tag{2.1}$$

Here, $N_e(\vec{r})$ is the concentration of free electrons, V_e is the refractive volume of one electron, $r_e = 2.82 \cdot 10^{-15}$ m is the classical electron radius, λ is the radio wavelength, and the origin for the position vector $\vec{r}$ is at the center of the planet. In the expression above, a small correction which leads to Faraday rotation has been ignored. As the Voyager spacecraft transmitted signals in right-hand circular polarization, this approximation is acceptable. Note, however, that measurements of Faraday rotation are planned as part of an occultation experiment in a future investigation of the Jovian system using the Galileo orbiter, which will transmit one signal in linear polarization, and another in circular polarization [private communication, H. T. Howard, 1983].

In the neutral atmosphere, the refractive index of a mixture of gases including a suspension of dust particles or condensates can be expressed as [Eshleman, 1973]

$$n(\vec{r}) = 1 + \frac{3}{2} N_p(\vec{r}) V_p \frac{(n_p^2 - 1)}{(n_p^2 + 2)} + \sum_j N_j(\vec{r}) V_j \quad , \tag{2.2}$$

where the parameters $N_p(\vec{r})$, V_p, and n_p are the number density, volume, and refractive index of the suspended particles, and the summation is over the various constituents with number densities $N_j(\vec{r})$, and constants of proportionality V_j. For nonpolar gases, V_j appears to be independent

of concentration, temperature, and pressure [e.g., Tyler and Howard, 1969]. This formula remains valid under general atmospheric conditions when the mutual separation of the suspended particles is small compared to λ.

2.3 Physical Models for Refractive Irregularities

The preceding section considered the principal contributions to refractivity in planetary ionospheres and atmospheres; here, models for the spatial variations in refractive index are proposed. Notice that in deriving theoretical expressions for the weak-scattering scintillation spectra in Appendix A, the refractive index in the phase screen was described as a locally homogeneous random field. In this case, the theoretical spectra (equations A36-A38 and A41-A43) depend only on the three-dimensional spatial spectrum of refractive index, Φ_n (see equation A12), which constitutes a complete statistical description of the refractive irregularities for occultation measurements. The sections that follow describe models for Φ_n appropriate in the ionosphere and the neutral atmosphere, and define the variables and coordinate systems that are used in subsequent chapters. For a discussion of the physical significance of Φ_n, the reader is referred to Tartarskii [1971, pp. 1-46] or Yaglom [1962].

2.3.1 Ionospheric Irregularities.

It is useful to consider the terrestrial ionosphere in order to construct a theoretical model for the ionospheric irregularities at Jupiter and Saturn. In the earth's upper ionosphere, the spatial spectrum of irregularities in electron density obeys a power law for length scales ranging from the ion gyroradius (a few meters) to the ionospheric scale height (a few tens of kilometers)

[Yeh and Liu, 1982; Booker, 1979; Rufenach, 1972, 1974; Dyson et al., 1974; Phelps and Sagalyn, 1976]. In addition, the irregularities are anisotropic and "field aligned" -- the correlation length of these structures is largest along the direction of the earth's magnetic field [Spencer, 1955; Singleton, 1970a; MacDougall, 1981]. By analogy, the irregularities at Jupiter and Saturn are expected to possess these same characteristics for two reasons. First, the magnetic field in the terrestrial ionosphere [Langel et al., 1980] is comparable in magnitude to Saturn's field [Connerney et al., 1982], but is greatly exceeded by Jupiter's field [Acuna and Ness, 1976]. Hence, the magnetic field is expected to constrain the motion of charged particles in the upper ionospheres of these two planets in the same manner as it does at the earth. Second, the size of the irregularities observed at Jupiter and Saturn (see Chapters 4 and 5) was well within the bounds of the ion gyroradius ($\approx$ 1 meter) and the ionospheric scale height ($\approx 10^3$ km) [Eshleman et al., 1979b, c; Tyler et al., 1981a, 1982]. Consequently, an anisotropic (field-aligned), power-law spatial spectrum was used in computing theoretical scintillation spectra for comparison with the measurements at Jupiter and Saturn. In a Cartesian coordinate system aligned with the principal axes of the irregularities, this spatial spectrum Φ_n is expressed as [cf. Singleton, 1970b; Rino and Fremouw, 1977]

$$\Phi_n(\kappa_1, \kappa_2, \kappa_3) = \frac{Q}{[1 + \kappa_o^{-2}(d^2\kappa_1^2 + e^2\kappa_2^2 + f^2\kappa_3^2)]^{p/2}} \quad , \qquad (2.3)$$

where Q is a normalization constant that is proportional to the variance of refractive index, $\langle n_t^2 \rangle$; $2\pi/\kappa_o$ corresponds to the outer scale;

κ_1, κ_2, and κ_3 are the components of the wave vector; d, e, and f are numerical factors that determine the degree of anisotropy; p is the power-law exponent; and the κ_2-direction is parallel to the magnetic field, $\vec{B}$.

For simplicity, it is assumed that the irregularities are symmetrical with respect to rotations about the magnetic field direction, so that d = f. In this case, the correlation lengths of the ionospheric irregularities along the magnetic field and perpendicular to this direction are in the ratio e/f [cf. Singleton, 1970b]. Large axial ratios (e/f >> 1) correspond to highly elongated field-aligned structures, smaller axial ratios characterize irregularities with ellipsoidal shapes, and e/f = 1 for isotropic irregularities. With the proper choice of the principal axis, the irregularities can always be represented by an axial ratio e/f $\geq$ 1.

The appropriate scattering theory for the ionospheric occultations considered here is the one derived in Sections A.2 and A.3, where the average refractive index in the phase screen is homogeneous; for present purposes differential refraction had a negligible effect. In computing the theoretical spectra (equations A36-A38), Φ_n must be expressed in the (κ_x, κ_y, κ_z) coordinate system defined in Section A.4 and shown in Figure 2.1. In this system, κ_x is parallel to the direction of radio-wave propagation, and κ_y is parallel to the projection of the magnetic field onto the phase screen. The transformation gives

$$\Phi_n(\kappa_x=0,\ \kappa_y,\ \kappa_z) = \frac{Q}{[1 + \kappa_0^{-2}(e'^2\kappa_y^2 + f^2\kappa_z^2)]^{p/2}} \quad . \qquad (2.4)$$

As shown in Appendix A, refractive variations along the direction of

propagation do not affect the signal scattered at small angles; hence, κ_x is set equal to zero in the argument of Φ_n (see equations A36-A38). Rino and Fremouw [1977] previously used a power spectrum of this form to describe irregularities in the earth's ionosphere.

The parameter e' is related to e, f, and the angle, Λ, between the $\vec{B}$ and the phase screen through $e'^2 \equiv e^2\cos^2(\Lambda) + f^2\sin^2(\Lambda)$. However, the effect of Λ is neglected here, since for the Voyager occultations by Jupiter and Saturn it is so small that $e' \approx e$.

For a phase screen with a homogeneous average refractive index, only the relative orientations of the raypath velocity in the phase screen, $\vec{v}_\star$, and the principal axis of the irregularities affect the scattering (cf. Appendix A). Hence, the phase screen coordinates defined in Figure 2.1 are convenient for representing the irregularities: a single angle, γ, specifies the unknown orientation of the principal axis, κ_y, relative to $\vec{v}_\star$. A total of five free parameters (Q, p, e/f, κ_0, and γ) constitute the theoretical description of the ionospheric irregularities.

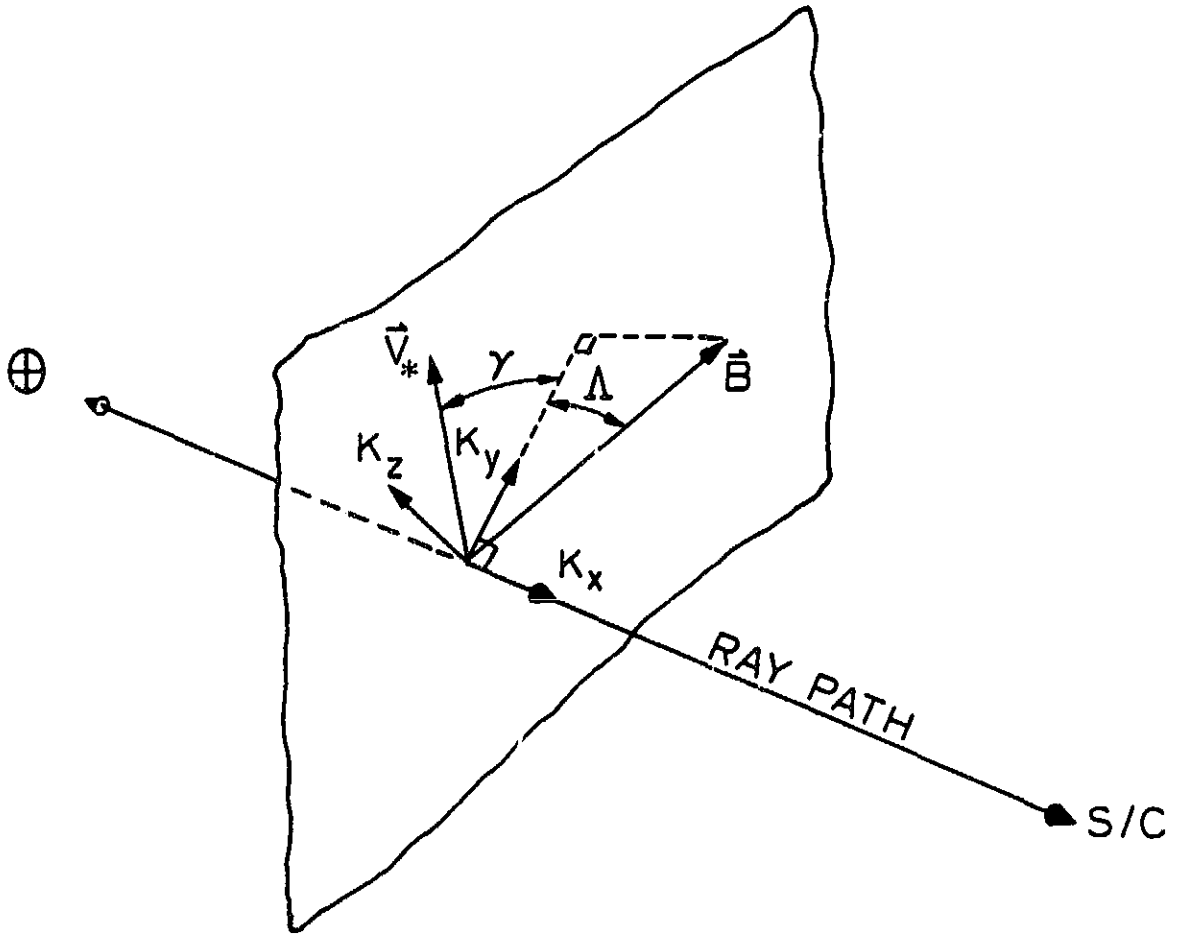

Figure 2.1 Schematic of phase screen for the case of scattering from ionospheric irregularities (Sections A.2 and A.3). In this coordinate system, κ_x is parallel to the direction of radio-wave propagation and perpendicular to the screen. The magnetic field, $\vec{B}$, intersects the screen at angle Λ, and κ_y is parallel to the projection of $\vec{B}$ onto the screen. The angle γ specifies the orientation of the principal axis of the irregularities, κ_y, relative to the raypath velocity, $\vec{v}_*$; note that $\vec{v}_*$ is perpendicular to κ_x. From the point of view of a terrestrial observer, $\vec{v}_*$, κ_y, and κ_z are in the plane of the sky.

2.3.2 Refractive Irregularities in the Neutral Atmosphere. In order to interpret the scintillations observed during the occultation of Voyager 1 by Titan, the spectrum of refractive irregularities in the neutral atmosphere is modeled using a formula analogous to equation 2.3. The motivation for choosing a power-law spectrum comes from observations of the earth's atmosphere [Vinnichenki, 1970] and theoretical considerations [Tatarskii, 1971, p. 46-102]. This type of spectrum is believed to be valid under many circumstances for describing the irregularities that result from either turbulence or a superposition of internal gravity waves [Dewan, 1979].

To account for the important influence of Titan's finite atmospheric scale height, the scattering theory must include the effect of Fresnel zone distortion; consequently, the formulas derived in Sections A.5 and A.6 (equations A41-A43) are appropriate for these calculations. Some slight modification of Φ_n from the previous form is needed. In this case, Φ_n must be expressed in the $(\kappa_x, \kappa_y, \kappa_z)$ coordinates defined in Section A.4 and shown in Figure 2.2, where κ_x is parallel to the direction of radio-wave propagation, but κ_y is now parallel to the visible limb of the planet at the occultation point:

$$\Phi_n(\kappa_x = 0, \kappa_y, \kappa_z) = \frac{Q}{\left[1 + \kappa_o^{-2}(A\kappa_y^2 + B\kappa_y\kappa_z + C\kappa_z^2)\right]^{p/2}} \quad . \quad (2.5)$$

The parameters A, B, and C are related to e/f and the angle ψ between the principal axis of the irregularities and κ_y through $A \equiv e^2\cos^2(\psi) + f^2\sin^2(\psi)$, $B \equiv 2\,(e^2 - f^2)\,\sin(\psi)\,\cos(\psi)$, and $C \equiv e^2\sin^2(\psi) + f^2\cos^2(\psi)$. As mentioned above, these occultation measurements are insensitive to refractive variations along the

direction of propagation. Consequently, a terrestrial observer can discern only the the orientation of the irregularities in the plane of the sky (y-z plane) as specified by ψ.

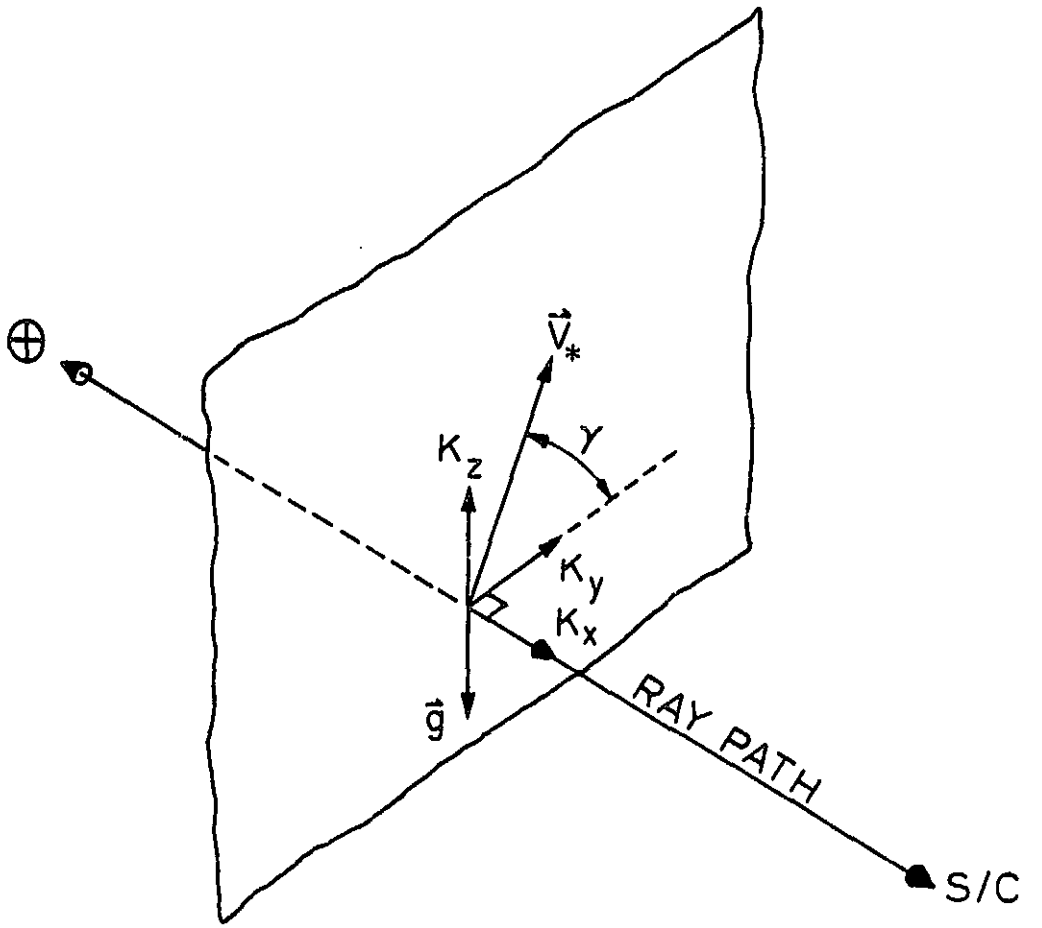

Figure 2.2 Schematic of phase screen for scattering from irregularities in the neutral atmosphere (cf. Sections A.5 and A.6). In this coordinate system, κ_x is parallel to the direction of propagation and perpendicular to the screen; κ_y is parallel to the visible limb of the planet at the occultation point; and κ_z coincides with the vertical direction, opposite to the gravitational acceleration, $\vec{g}$. The angle γ specifies the known orientation of the raypath velocity, $\vec{v}_*$, with respect to the limb of the planet, κ_y. Note that $\vec{v}_*$ and $\vec{g}$ are perpendicular to κ_x.

Figure 2.3 shows a diagram of "typical" refractive irregularities as viewed from earth. The two characteristic dimensions of the structures (parallel and perpendicular to the direction indicated by ψ) are in the ratio e/f. For example, when $\psi = 0$, large axial ratios ($e/f \gg 1$) correspond to layer-like structures with little horizontal variation, smaller axial ratios ($e/f \gtrsim 1$) characterize irregularities with both horizontal and vertical variations, and $e/f = 1$ for isotropic irregularities.

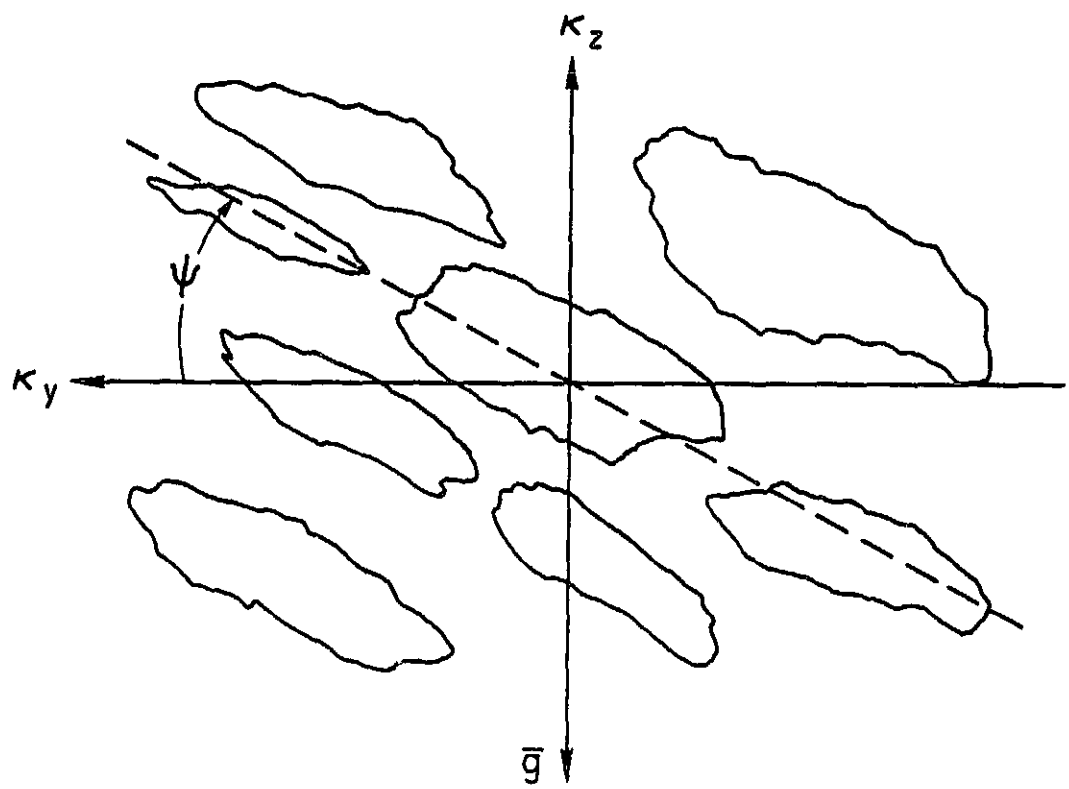

Figure 2.3 Typical irregular structures in a planetary atmosphere from the point of view of a terrestrial observer. The angle ψ gives the orientation of the principal axis with respect to the visible limb of the planet.

Models for Refractive Irregularities

As in the representation of ionospheric irregularities, the free parameters in the model for Φ_n in the neutral atmosphere include Q, p, e/f, and κ_0. However, for scattering from the neutral atmosphere, where Fresnel zone distortion is appreciable, both the relative and absolute orientations of $\vec{v}_*$ and the principal axis affect the scattering, so that two angles are required to specify the geometry. In this case, γ indicates the known direction of $\vec{v}_*$, while ψ specifies the unknown orientation of the principal axis; both angles are measured relative to κ_y. These five free parameters (Q, p, e/f, κ_0, and ψ) constitute the theoretical description of irregularities in the neutral atmosphere.

CHAPTER 3

DATA ANALYSIS AND INTERPRETATION

3.1 Introduction

This chapter describes a new procedure for the systematic analysis and interpretation of radio scintillations observed during planetary occultations. Through the use of conventional methods for spectral data analysis along with the well-developed weak-scattering theory, this procedure yields results which are more accurate and complete than those reported previously (see Section 4.1 for a comparison with the method used to analyze data from the occultations of the Pioneer spacecraft by Jupiter). The present technique, which employs a rigorous scattering theory, has evolved from the approach developed by Tyler et al. [1981b], where an approximate theory was applied to interpret observations of radio-wave scattering from the solar corona.

3.2 Fundamental Measurements

The radio signals used for the Voyager occultation measurements were derived from a highly stable, radiation shielded, quartz oscillator carried by the spacecraft. Two unmodulated signals were transmitted in right-hand circular polarization through the 3.7-m spacecraft antenna, one at 13-cm wavelength (26 W) and a second at 3.6-cm wavelength (12 W), and received with the NASA Deep Space Network (DSN) 64-m antenna tracking stations. The spacecraft and other radio equipment used in this experiment has been described in more detail elsewhere [Eshleman et al., 1977].

The DSN tracking stations coherently sampled and recorded the signals received from Voyager for later processing. After delivery to Stanford, the data were first digitally filtered to bandwidths of about 1 kHz. Then, a previously developed method [Lipa and Tyler, 1979] was applied to estimate the instantaneous frequency, $f(t)$, and amplitude, $A(t)$, of each received signal from a sequence of power spectra of the filtered data. The measurements of $A(t)$ are unbiased in that the procedure accounts for the average effect of system noise. Values of $f(t)$ and $A(t)$ were typically computed at intervals $\delta t = 0.05$ s, although the sampling rates varied among occultations as a result of differences in the recording bandwidth of the DSN equipment and the occultation geometry. The specific sampling rates will be given in connection with the discussions in Chapters 4, 5, and 7. All subsequent processing steps were based on these measured values of $f(t)$ and $A(t)$.

To illustrate certain signal characteristics, it is useful to consider the data concerning Jupiter's ionosphere which were obtained at Voyager 1 occultation immersion. The time history of scintillations can be displayed on an Argand diagram by plotting the normalized phasors $[A(t)/\langle A\rangle]\cdot\exp[j\phi(t)]$ in the complex plane. The normalizing value $\langle A\rangle$ represents an average over time, while the fluctuations in signal phase $\phi(t)$ were obtained by fitting a quadratic curve to measurements of $f(t)$ over periods of 6.6 s and integrating the residuals. The quadratic detrending of $f(t)$ before integration removes the effects of spacecraft motion relative to the DSN station from $\phi(t)$. In the absence of noise, a signal that had propagated through an ionosphere without refractive irregularities would appear as a constant unit vector along the positive real axis.

Figure 3.1A shows such a plot of 128 measurements of amplitude and phase, at 0.051 s intervals, for data preceding Voyager 1 occultation immersion. The fluctuations are indicative of the noise level of the occultation measurements. At the sampling rates considered here, thermal efects at the DSN station and in the earth's atmosphere were the predominant source of amplitude and phase noise at 13 cm, and amplitude noise at 3.6 cm. In addition to the thermal noise sources, instrumental effects -- possibly in the DSN programmed oscillator or the spacecraft oscillator -- contributed appreciably to the phase noise at 3.6 cm.

Figure 3.1B shows a second plot for data at a later time as the path of propagation from spacecraft to earth traversed Jupiter's upper ionosphere. The increased but still small fluctuations in amplitude and phase at both wavelengths are the result of scattering from refractive irregularities. The effect at the 13-cm wavelength is larger, primarily as a result of plasma dispersion. Figure 3.1C shows a third plot obtained at a slightly later time, and hence with ray periapsis deeper in Jupiter's ionosphere, where stronger spatial variations in free electron density produced a pronounced effect at 13 cm as indicated by the random walk of the (A, ϕ) phasor about the origin. The 3.6-cm signal remained weakly perturbed during the corresponding time.

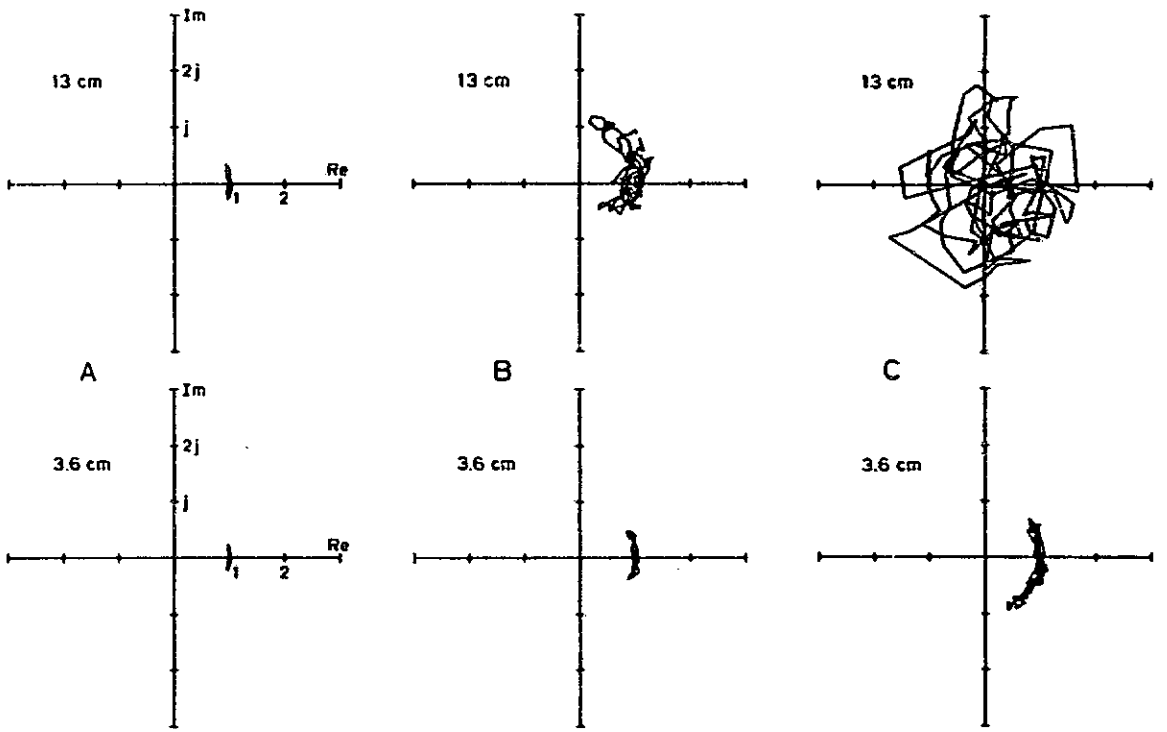

Figure 3.1 Argand diagrams of normalized 3.6-cm and 13-cm signals. Each plot contains 6.6 s of data from Voyager 1 occultation immersion at Jupiter. In the absense of noise, an unperturbed signal would appear as a constant unit vector along the positive real axis. (A) Fluctuations in amplitude and phase resulting from measurement noise before occultation entry. (B) Weak perturbations of both the 3.6-cm and 13-cm signals by refractive irregularities high in Jupiter's ionosphere. (C) Enhanced effects at both wavelengths due to irregularities deep in the ionosphere.

Appendix B sets a limit for the validity of the weak-scattering theory. When this criterion is applied to the results in Figure 3.1, the data at both wavelengths in part B, and at 3.6 cm in part C, are found to satisfy the condition for weak scattering, while the 13-cm data in part C exceed this limit and correspond to strong scattering. In general, for weakly-scattered signals, the phasors remain within a relatively small region in the complex plane; for strong scattering, the distribution of signal phasors has a "random" appearance. In this regard, Argand diagrams provide a useful diagnostic tool for evaluating the signal characteristics. The reader is referred to Flatte [1979] for additional discussion of the interpretation of phasor diagrams, and to Hinson and Tyler [1983] and Hinson [1983] for comparison with occultation results from Titan's neutral atmosphere and Saturn's ionosphere, respectively.

3.3 Spectral Data Analysis

The scintillation data were spectrally analyzed over time intervals in which the fluctuations in amplitude and phase appeared to be statistically similar, or stationary, as determined by inspection of Argand diagrams and the time history of A(t) and f(t). The fluctuations in amplitude were normalized according to

$$a(t) \equiv \frac{A(t) - \langle A \rangle}{\langle A \rangle} \quad , \tag{3.1}$$

and values of $\phi(t)$ were computed as before using the same detrending interval as for determining $\langle A \rangle$.

Discrete sample spectra were computed from the formulas [cf. Jenkins and Watts, 1968, pp. 209-211, 340-344],

$$C_{aa}(f_k) \equiv \frac{1}{m}\left|\sum_{n=0}^{m-1} a(t_n)\,\exp[-j2\pi f_k t_n]\right|^2 ,$$
$$C_{\phi\phi}(f_k) \equiv \frac{1}{m}\left|\sum_{n=0}^{m-1} \phi(t_n)\,\exp[-j2\pi f_k t_n]\right|^2 , \qquad (3.2a)$$

and using the a(t) and $\phi(t)$ measured at the same radio wavelength,

$$C_{a\phi}(f_k) \equiv \frac{1}{m}\left\{\sum_{n=0}^{m-1} a(t_n)\,\exp[j2\pi f_k t_n]\right\}\left\{\sum_{n=0}^{m-1} \phi(t_n)\,\exp[-j2\pi f_k t_n]\right\} , \qquad (3.2b)$$

where $f_k = \frac{k}{m\cdot\delta t}$, $k = 0, 1, 2, \ldots, m-1$.

Here, f_k and t_n represent the m sampling frequencies and times in the discrete Fourier transform pair, and vertical bars denote the magnitude. In order to reduce the bias from detrending, the detrending interval was selected to be $2m\cdot\delta t$ -- twice as long as the time interval for each spectrum. Several sample spectra from within a time interval were averaged to produce smoothed spectra for amplitude, $\overline{C}_{aa}(f_k)$, and phase, $\overline{C}_{\phi\phi}(f_k)$, and the smoothed cross amplitude-phase spectrum, $\overline{C}_{a\phi}(f_k)$. The time interval chosen for a sample spectrum resulted from a compromise between long time intervals, which reduce bias effects and improve frequency resolution, and short intervals, which allow more smoothing and reduce the variance [Jenkins and Watts, 1968, pp. 230-257]. Typically, eight sample spectra, each computed from m = 128 time domain samples, were averaged to produce each smoothed result.

The cross spectrum provides a measure of the relative size and phase of correlated fluctuations at each frequency in two stochastic processes. Of particular interest is the smoothed squared coherency spectrum defined as

$$|\overline{K}_{a\phi}(f_k)|^2 = \frac{|\overline{C}_{a\phi}(f_k)|^2}{\overline{C}_{aa}(f_k) \cdot \overline{C}_{\phi\phi}(f_k)} \quad . \tag{3.3}$$

The squared coherency plays the role of a correlation coefficient defined at each sample frequency f_k, and is used below along with the phase of $\overline{C}_{a\phi}$ to demonstrate the consistency of the data with weak-scattering theory.

In analyzing the scintillations observed during the occultation of Voyager 1 by Titan's neutral atmosphere, two slight deviations from the above procedures were introduced. First, as it is conventional to discuss the intensity, I(t), rather than A(t) during occultations by neutral atmospheres, the spectrum of intensity, $\overline{C}_{ii}$, instead of $\overline{C}_{aa}$ was measured. This change is insignificant for the case of weak scattering, where $\overline{C}_{ii} = 4 \cdot \overline{C}_{aa}$ (see Section A.7). Second, the normalized intensity was computed from

$$i(t) \equiv \frac{I(t) - \langle I(t) \rangle}{\langle I(t) \rangle} \quad . \tag{3.4}$$

Here, the normalization $\langle I(t) \rangle$ represents a least-squares quadratic fit to I(t) over the time period used, and accounts for the gradual changes in I(t) resulting from differential refraction (see Appendix D) and antenna pointing, which were insignificant during the ionospheric occultations. In addition, the fractional variance of intensity, σ_i^2, was calculated for data from the Titan occultation.

3.4 Interpretation of Scintillation Spectra

Smoothed amplitude and phase spectra, obtained by the procedure described in Section 3.3, were used as estimates of the actual spectrum of the data. To a good approximation, the measurements at the discrete sample frequencies are uncorrelated and obey chi-squared statistics [Jenkins and Watts, 1968, pp. 230-257], with typically 15 degrees of freedom for the data analyzed here. Noting that the chi-square approaches a Gaussian distribution with increasing degrees of freedom, the statistics of the measurements can conveniently and accurately be modeled as Gaussian with fractional variance M^{-1}, where M is the number of sample spectra averaged in the smoothed result.

In order to identify the contribution to signal fluctuations that arises from atmospheric scattering, the noise level of the spectra was determined empirically from measurements before immersion and after emersion. These noise levels are indicated, for example, in Figures 4.3, 5.5, and 7.3, below; their appearance can be explained as follows. In the absence of atmospheric scattering, successive temporal measurements of a(t) or f(t) are uncorrelated; hence, the spectra of noise fluctuations in both a(t) and f(t) are white. By applying basic Fourier transform properties to this result, the "power spectrum" of noise fluctuations in $\phi(t)$ has slope -2 on a logarithmic display.

All spectra analyzed in Chapters 4, 5, and 7 exhibit $\langle a^2 \rangle \leq 0.06$, which satisfies the limit for validity of the weak-scattering theory (Appendix B). In order to interpret the weak ionospheric scintillations, theoretical spectra were computed numerically from equations A36-A38 using the expression for Φ_n in equation 2.4 as a model for the refractive irregularities. Alternatively, theoretical spectra

for weak scattering from the neutral atmosphere were computed numerically from equations A41-A43 and 2.5. In the models for Φ_n (equations 2.4 and 2.5 in Section 2.3), the free parameters which characterize the refractive irregularities include: (1) the inverse power-law exponent, p; (2) the axial ratio, e/f; (3) the orientation, specified by γ in the ionosphere, or ψ in the neutral atmosphere; and (4) the strength, Q. (The fifth parameter, κ_o, is discussed below.) The theoretical spectra were fitted to each measured amplitude or phase spectrum in a least-squares sense by varying these four free parameters to minimize the residual

$$\sigma_r^2 \equiv \frac{1}{K-1} \sum_{k=1}^{K} \{ \log_{10}[\overline{C}(f_k)] - \log_{10}[w(f_k)] \}^2 \quad . \qquad (3.5)$$

Here, $\overline{C}(f_k)$ is the measured spectrum, $w(f_k)$ is the theoretical spectrum, and the summation runs over sample frequencies, f_k, for which the scintillation spectra exceeded the noise level by at least 3 dB. In some cases computational convenience led to larger values for this cutoff. Notice that the spectra are compared in the log domain, where the measurements at all sample frequencies have the same variance. The values of the parameters at the minimum were taken as characteristic of the irregularities, which requires a homogeneous Φ_n over the atmospheric region corresponding to one spectrum.

As a test of these solutions for parameters, spectra were analyzed by first subtracting the noise level and then fitting the theoretical spectra. The parameter estimates were found to be insensitive to this change in procedures, and hence to the measurement noise.

Within the limitations imposed by experimental geometry and the method of data analysis, no evidence for an outer scale, $2\pi/\kappa_o$, was found in any case. Consequently, all theoretical spectra were calculated from the formulas of Chapter 2 and Appendix A in the limit where $\kappa_o \to 0$; this parameter then had a negligible effect on the theory over the range of measurement frequencies.

The variance of refractive index was determined from (see equation A12)

$$\langle n_t^2 \rangle = \iiint \Phi_n(\kappa_x,\kappa_y,\kappa_z)\, d\kappa_x\, d\kappa_y\, d\kappa_z \quad , \tag{3.6}$$

where $n_t(\vec{r})$ represents the variations in refractive index away from the spatial average, and the parameters of Φ_n were determined from the data. The limits of integration were restricted to the range of wave vectors which could be detected, so measured values of $\langle n_t^2 \rangle$ given below apply only to this range. Using the formulas in Section 2.2 (equations 2.1 and 2.2), $\langle n_t^2 \rangle$ can be related to variations in free electron concentration in the ionosphere or fluctuations in particle densities in the neutral atmosphere, as appropriate.

The covariance matrix of the solutions for the four parameters, [Cov], was computed by standard propagation of errors [Brandt, 1970, pp. 196-212] using the theoretical expressions in equations A36 and A37 or A41 and A42 as models for the process. The general form of the matrix is

$$[\mathrm{Cov}] = \sigma_r^2 [\bar{\bar{P}}^T\, \bar{\bar{P}}]^{-1} \quad . \tag{3.7}$$

Here, $\overline{P}$ is the m-by-4 matrix of first partial derivatives of the theoretical spectrum with respect to the four parameters at each of the m sample frequencies. The variance of each measured parameter is proportional to σ_r^2 (see equation 3.5). As discussed by Brandt, the diagonal elements of [Cov] can be considered the variance of the four parameter measurements. While the off-diagonal elements are useful in specifying the statistical relationships among the parameters, they are not reported here as they do not give additional information on the uncertainty in any one parameter. All uncertainties given in tables in Chapters 4-7 refer to the standard deviations as calculated from equation 3.7. On the basis of the discussion in Appendix E, these uncertainties are believed to be realistic and not simply formal.

As a test of this procedure for computing uncertainties, the measurements were simulated using a statistical model. Artificial spectra were generated by adding different realizations of uncorrelated Gaussian noise with fixed fractional variance to a theoretical spectrum. Then, each of these spectra was analyzed by the procedure described above to obtain least-squares solutions for parameters. The statistics of the parameter measurements obtained in this way confirmed the predictions of the covariance matrix.

The smoothed cross spectrum, $\overline{C}_{a\phi}$, provides an estimate of the true cross spectrum of two stochastic processes. The variance of the estimate can be reduced through averaging, but also depends on the uncontrollable influence of the coherency spectrum. At frequencies where the coherency is small, the processes are only weakly correlated, and the estimates of $\overline{C}_{a\phi}$ are inherently noisy. This effect resulted in a large variance in $\overline{C}_{a\phi}$ for the present measurements of weak

scattering. Hence, the solutions for parameters obtained from analysis of $\bar{C}_{a\phi}$ were less reliable than solutions derived from $\bar{C}_{aa}$ or $\bar{C}_{\phi\phi}$, and will not be given here. However, for completeness and as a test of the theory, Chapters 4 and 5 include comparisons of theoretical spectra with the experimentally derived squared coherency and phase of $\bar{C}_{a\phi}$.

CHAPTER 4

SPATIAL IRREGULARITIES IN JUPITER'S UPPER IONOSPHERE

4.1 Introduction

Following the first two spacecraft encounters with the Jovian system by Pioneer 10 in December, 1973, and Pioneer 11 in December, 1974 [Hall, 1975; Gehrels, 1976], Voyagers 1 and 2 were used to continue the reconnaissance of Jupiter and its environment during flybys in March and July, 1979 [Stone and Lane, 1979a, b]. The investigations with each of the four spacecraft included radio occultation measurements of Jupiter's ionosphere and neutral atmosphere. Through analysis of the radio data from the occultations of Voyagers 1 and 2, Eshleman et al. [1979b, c] and Lindal et al. [1981] determined vertical profiles of the gas refractivity, molecular number density, pressure, temperature, and microwave absorption in the neutral atmosphere, along with the average electron density in the ionosphere. Results of a similar nature, as derived from the Pioneer radio occultation data, were reported by Kliore and Woiceshyn [1976] and Fjeldbo et al. [1976]. In the present discussion, attention is focused on rapid fluctuations of the radio signals observed during the Voyager occultations by Jupiter's ionosphere.

During the occultations of Pioneers 10 and 11 by Jupiter, ionospheric structures caused scintillations in the radio signal transmitted by the spacecraft and received on the earth. Woo and Yang [1976, 1978] and Woo and Armstrong [1980] analyzed these data and attributed most of the amplitude fluctuations to scattering by anisotropic turbulence. The spectrum of the turbulence appeared to

follow a power law with exponent near the Kolmogorov value of -11/3 [Woo and Yang, 1976, 1978], although subsequent analysis of spectral broadening suggested a value of -3.3 [Woo and Armstrong, 1980]. In addition, the magnetic field orientation in Jupiter's ionosphere was inferred from the measured direction of anisotropy. At one location, the estimate of field orientation agreed with the predictions of a Jovian magnetic field model derived from Pioneer magnetometer data; at three other locations the measurements disagreed with the model by as much as 10° [Woo and Yang, 1978; Smith et al., 1976]. However, Woo and Yang did not indicate the uncertainties of the measurements, so the significance of the differences is unclear.

When comparing the Pioneer and Voyager results concerning ionospheric irregularities, it should be noted that the Voyager data are improved with respect to the Pioneer data for three reasons. First, Voyager observations were obtained simultaneously at two coherently related radio wavelengths (3.6 and 13 cm) instead of the single 13-cm wavelength of the Pioneer data. For the same distribution of plasma irregularities, the 3.6-cm signal is much less susceptible to scattering than the 13-cm signal -- the variance of plasma induced intensity fluctuations was typically 30 times larger at the longer wavelength. Consequently, the 3.6-cm signal was weakly perturbed in regions of the lower ionosphere where the 13-cm signal experienced strong scattering. The short-wavelength signal thereby significantly extended the range of the occultation measurements, since weak scattering is well understood, whereas strong scattering is difficult to interpret. Second, for Voyager at 3.6 cm the signal-to-noise ratio (SNR) was about 100 times greater than for Pioneers 10 and 11. The improved signal revealed more

detail in the measured spectra, which allowed closer comparison between theory and observations (compare Figures 7-10 of Woo and Yang [1978] with Figures 4.3, 4.6, and 4.10 in this chapter). Third, the increased SNR combined with the improved stability of the Voyager radio equipment allowed analysis of fluctuations in signal phase, which was not possible with Pioneer.

There also has been a significant advance in the methods used for analyzing scintillation spectra (Chapter 3). This study established a consistent procedure for evaluating the quality and character of the occultation signals (e.g., Argand diagrams, Section 3.2). Furthermore, four parameters of the theory were determined by the method of least squares, and the measurement uncertainties were calculated by propagation of errors (Section 3.4). Woo and Yang [1976, 1978] did not report the use of an objective method in obtaining a fit of the theory to the measured Pioneer spectra. In addition, they frequently showed the same theoretical parameters in fits of theory to spectra measured at different altitudes (see Woo and Yang [1978], Figures 7-10), which leaves some question as to whether the best fit has been found. Finally, as the uncertainties in final parameters were not given, the Pioneer results were difficult to interpret.

Section 4.2 describes the Voyager occultation measurements; Section 4.3 follows with a discussion of findings for the spatial characteristics of the ionospheric irregularities. Comparisons with the previously published Pioneer results are included where appropriate. Present results, which have been published elsewhere [Hinson and Tyler, 1982], are used subsequently in Chapter 6 to infer magnetic field orientations in Jupiter's ionosphere.

4.2 Experimental Geometry and Measurements

Figure 4.1 shows the view from earth of the Voyager occultations including the two raypath trajectories in the atmosphere. For Voyager 1 (V1), occultation immersion occurred on March 5, 1979, at 10°S, 63°W, with solar zenith angle $\delta = 82°$ (late afternoon). Occultation emersion followed at 0°, 314°W, $\delta = 98°$ (predawn). Voyager 2 (V2) occultation immersion occurred on July 10, 1979, at 65°S, 260°W, $\delta = 88°$ (evening), with emersion at 50°S, 150°W, $\delta = 92°$ (early morning). All longitudes above are expressed in System III, 1965 [Seidelmann and Divine, 1977]. Prior to immersion and immediately following emersion, the radio path from the spacecraft to earth traversed only Jupiter's ionosphere; at these times scintillations of both radio signals were observed at all four locations.

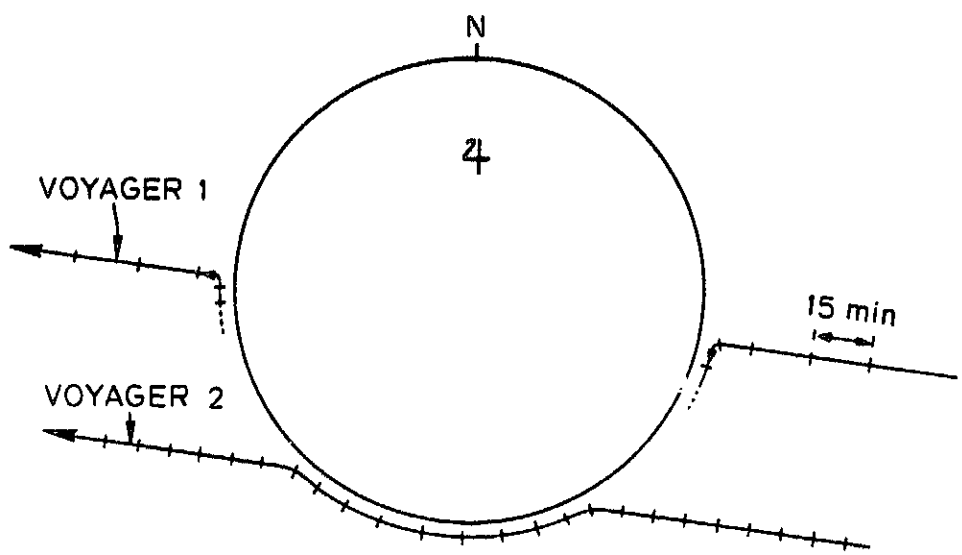

Figure 4.1 Schematic view from earth of the Voyager occultations by Jupiter showing the paths followed by the spacecraft radio images.

Several parameters which characterize the Voyager occultations by Jupiter near immersion and emersion are listed in Table 4.1. Here, $\vec{v}_*$ is the raypath velocity in the plane of the sky, Δ specifies the orientation of $\vec{v}_*$ with respect to Jupiter (see Figure 6.1), D is the distance from the spacecraft to the visible limb of Jupiter, and the Fresnel zone radius is given by $(\lambda D)^{1/2}$, where λ denotes the radio wavelength.

Table 4.1 Geometric parameters that characterize the Voyager occultations by Jupiter near immersion and emersion.

Space-craft	Lat.[1]	Long.[2]	$\lvert\vec{v}_*\rvert$, km/s	Δ, degrees	D, km	Fresnel-zone radius, km	
						13 cm	3.6 cm
V1	10°S	63°W	20.1	175.	$4.45 \cdot 10^5$	7.62	3.98
V1	0°	314°W	20.2	5.	$5.47 \cdot 10^5$	8.46	4.42
V2	65°S	260°W	10.5	122.	$1.35 \cdot 10^6$	13.3	6.94
V2	50°S	150°W	10.5	57.	$1.42 \cdot 10^6$	13.6	7.13

[1]Planetocentric

[2]Sys III, 1965 [Seidelmann and Divine, 1977]

The procedure for preliminary data reduction was described in Section 3.2. At both wavelengths, values of signal frequency, f(t), and amplitude, A(t), were determined each 0.051 s for V1 and 0.102 s for V2 in order that signal parameters would be adequately sampled. Limitations of the radio equipment and observation time resulted in uncertainties in a single estimate of frequency and amplitude of approximately 0.2 Hertz and 2%, respectively. The processing steps in the remainder of this chapter, as well as the Argand diagrams in Figure 3.1, were based on these measured values of f(t) and A(t).

Using the method described in Section 3.3, the fluctuations in phase $\phi(t)$ and normalized amplitude $a(t)$ were reduced to obtain temporal spectra. Theoretical spectra were then fitted to the measurements by the least-squares procedure in Section 3.4, yielding solutions for the four principal parameters that characterize the ionospheric irregularities (cf. Section 2.3.1). The parameter measurements and their uncertainties are discussed below.

4.3 Results

V1 Immersion (10°S, 63°W). The profile of the average electron density in Jupiter's upper ionosphere appears in Figure 4.2. This curve was derived from the measurements during V1 immersion [Eshleman et al., 1979b], and can be extended to lower altitudes using more elaborate inversion techniques [Fjeldbo, 1964].

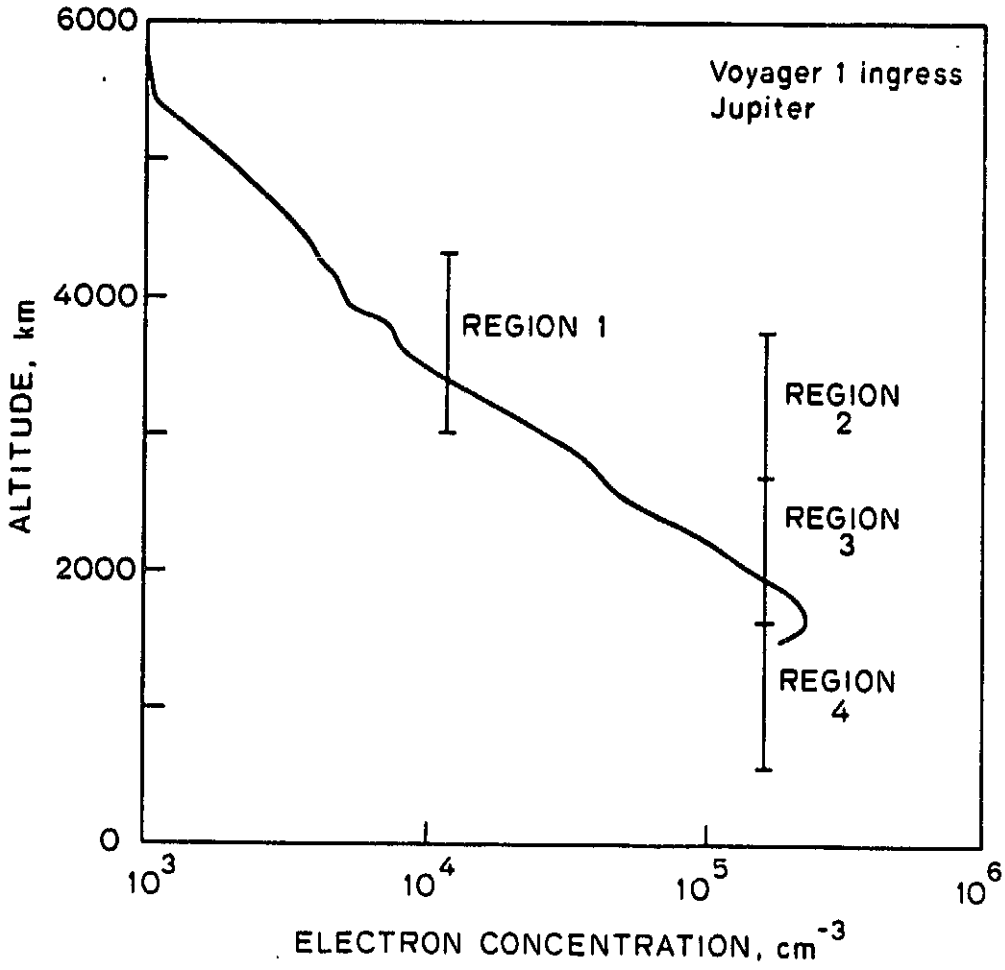

Figure 4.2 Profile of average electron concentration in the upper ionosphere at V1 immersion. Regions 1-4 indicate altitude intervals for computing spectra. These altitudes apply to periapsis of the radio raypath from spacecraft to earth, and are referenced to the 1 mbar level in the neutral atmosphere [profile from Eshleman et al., 1979b].

Weak scattering of the 3.6-cm signal was observed throughout the ionospheric occultation; spectra of 3.6-cm amplitude and phase from the altitude intervals 2, 3, and 4 of Figure 4.2 appear in Figure 4.3. The 13-cm signal experienced strong scattering in the lower ionosphere; since analysis here is restricted to weak scattering, a 13-cm spectrum was computed only over a single high altitude interval, region 1 of Figure 4.2. In the spectra, the indicated noise levels were derived from measurements before immersion (see Section 3.4). No phase spectra are shown for the high altitude smoothing intervals, regions 1 and 2, because noise dominated these measurements. The best fit theoretical spectra computed from equations A36, A37, and 2.4 are shown superimposed in Figure 4.3.

Figure 4.4 displays the observed squared coherency and cross spectrum phase for the two smoothing intervals where both the phase and amplitude spectra were available (regions 3 and 4). The 1-σ uncertainties depend on the squared coherency and are therefore a function of frequency -- one typical value is indicated. The high frequency portion of each spectrum corresponds to measurement noise for which the cross spectrum phase has a random distribution. Using the parameters obtained from analysis of the amplitude and phase spectra (Figure 4.3), the theoretical squared coherency and cross spectrum phase were computed and superimposed on each measured spectrum. The agreement between theory and observations -- especially at the striking shifts in the phase of the cross spectra -- supports the validity of the parameter measurements and the underlying theory.

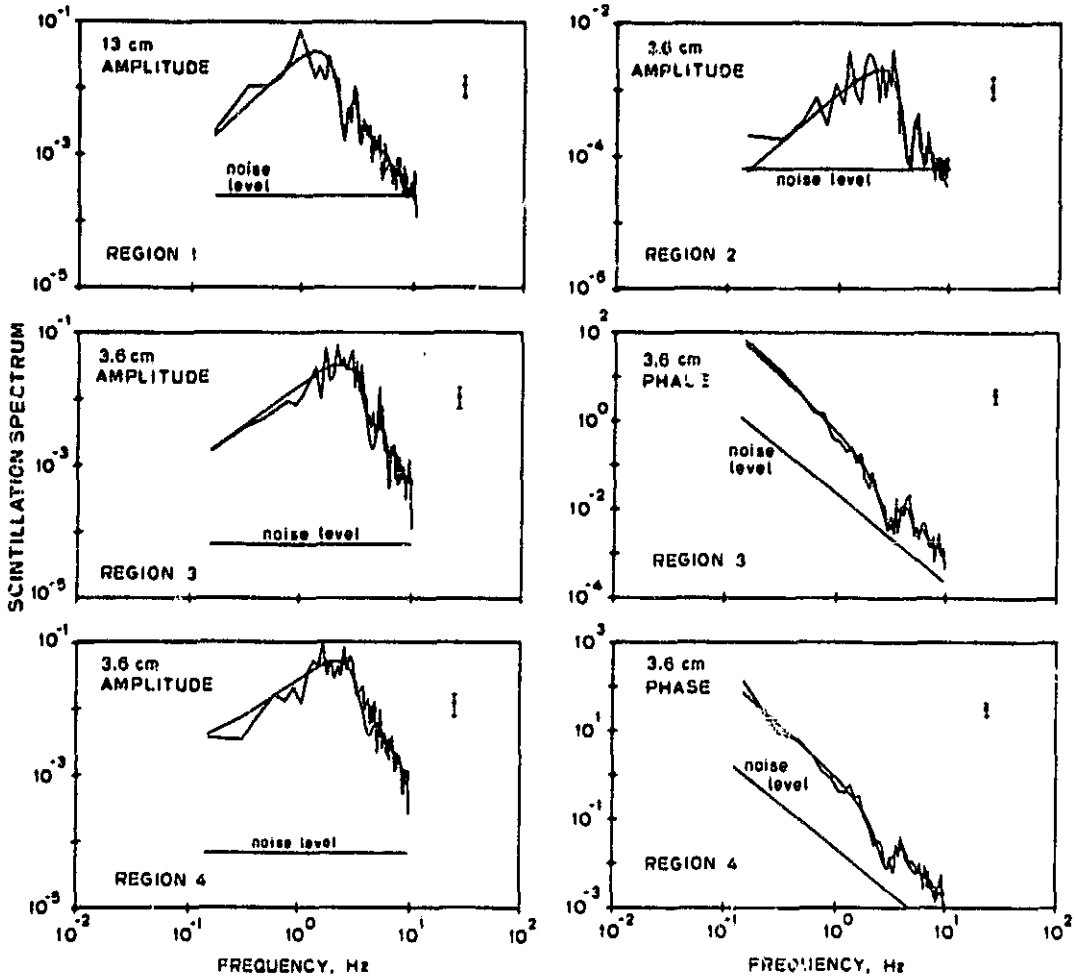

Figure 4.3 Amplitude and phase spectra at 3.6 and 13 cm from the smoothing intervals (regions 1-4) in Figure 4.2. The 1-σ uncertainties in each panel apply at all sample frequencies. Theoretical spectra (smooth curves superimposed) were fitted in a least-squares sense to measured spectra over the frequency range where the amplitude or phase fluctuations due to ionospheric scattering exceeded the noise levels by at least 3 dB.

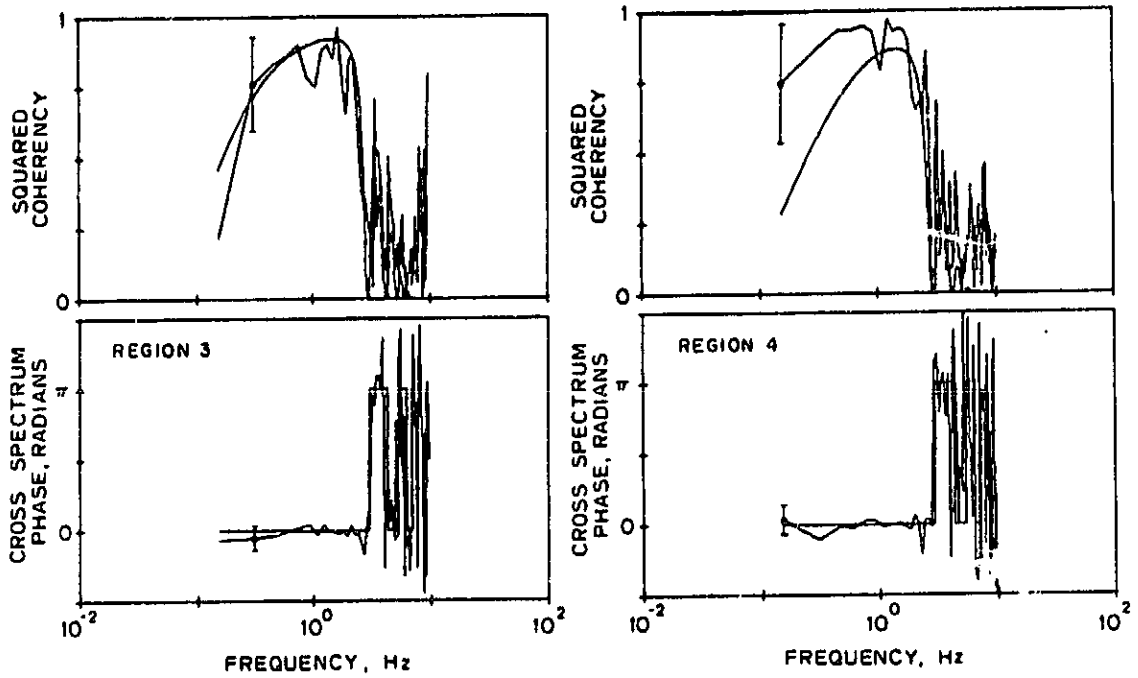

Figure 4.4 Squared coherency and cross spectrum phase at 3.6 cm from regions 3 and 4 of Figure 4.2. The 1-σ uncertainties are indicated at one sample frequency. The high frequency portion of each spectrum corresponds to measurement noise for which the cross spectrum phase has a random distribution. Theoretical curves are superimposed.

The least-squares solutions for ionospheric parameters derived from amplitude and phase spectra are listed in Table 4.2, with the 1-σ uncertainties as calculated by propagation of errors (cf. Section 3.4). The altitude assigned to each measurement corresponds to the center of the appropriate smoothing interval; each measurement should be interpreted as a spatial average over this altitude range. As indicated by the close agreement between theory and measurements in Figure 4.3, the three-dimensional spatial spectrum, Φ_n, closely follows an inverse power law with exponent, p, between 3.3 and 3.7. It is difficult to discern any vertical variation in p because of the measurement uncertainties; however, the axial ratio, e/f, apparently varies with altitude. Strong anisotropy was detected high in the topside ionosphere where collision frequencies are low -- the magnetic field is thought to strongly constrain the motion of charged particles in this region. Randomizing collisions occur more frequently in the lower ionosphere and reduce magnetic field effects; this may explain the decrease in the axial ratios at lower altitudes. The six estimates of γ, the orientation of Jupiter's magnetic field relative to the raypath velocity (see Figure 2.1), are mutually consistent and show no variation with altitude. This was expected, since models of Jupiter's field predict no appreciable variation with radius over the extent of the upper ionosphere.

In the weak-scattering theory applied here, ionospheric irregularities are assumed to obey the Taylor hypothesis so that they can be considered "frozen" on time scales of interest. The only significant time variation results from motion of the radio path across a fixed field of irregularities. For highly anisotropic irregularities,

only the component of ray path motion of magnitude $|\vec{v}_{\perp}| \cdot \sin(\gamma)$ which is perpendicular to the elongated axis will result in signal scintillations (cf. Appendix C). On the basis of this interpretation, irregularities of approximate size 2 to 100 km contribute to scattering over the frequency interval 0.2 to 10 Hz in Figure 4.3. These lower and upper limits result from noise limitations and the length of the measurement time interval, respectively, and do not represent either inner or outer scales. The spatial fluctuations of elecron density, δN_e, were determined from the parameter Q (Section 2.3.1) by using equations 3.6 and 2.1. The values listed in Table 4.2 refer only to irregularities in the stated size interval, and correspond to fractional variations in free electron concentration of about 10 to 15%.

Table 4.2 Characteristics of irregularities in Jupiter's upper ionosphere at V1 immersion.

Height, km	Spectrum type	γ, degrees	Power-law index	Axial ratio	δN_e, cm^{-3}
1200	3.6-cm a(t)	56 ± 2.4	3.6 ± 0.11	4.5 ± 0.8	14000 ± 3000
1200	3.6-cm ϕ(t)	56 ± 1.8	3.4 ± 0.06	4.5 ± 0.8	16000 ± 3000
2200	3.6-cm a(t)	58 ± 1.7	3.7 ± 0.10	6.0 ± 1.3	12000 ± 2000
2200	3.6-cm ϕ(t)	58 ± 1.7	3.5 ± 0.06	4.5 ± 0.8	12000 ± 2000
3200	3.6-cm a(t)	56 ± 1.0	3.6 ± 0.12	10. ± 2.2	2700 ± 500
3600	13-cm a(t)	58 ± 1.6	3.3 ± 0.08	7.5 ± 1.7	1400 ± 300

These measurements can be compared with results derived from Pioneer 10 immersion and Pioneer 11 emersion at latitudes of 27° N and 20° N, respectively. Woo and Yang [1978] concluded that p = 11/3 between altitudes 500 and 3000 km, which is slightly larger than the values in Table 4.2. The discrepancy could be due to the different methods used for obtaining this parameter. The values in Table 4.2 are least-squares solutions for p from analysis of amplitude and phase spectra, whereas Woo and Yang [1978] presumably assigned a value on the basis of theoretical considerations and a visual inspection of measured amplitude spectra. In addition, Woo and Yang reached the same conclusions given above concerning the effect of collisions on the axial ratio. However, the V1 results show that the axial ratio varies with altitude above 1200 km, which differs with the Pioneer observations of constant axial ratio in this region. Finally, Woo and Yang [1978] reported a fractional variation in electron density, $\delta N_e/N_e$, of between 9 and 18% near 1000 km altitude at 27°N. This result depends on the outer scale of the irregularities which they could not measure, but assumed to be 10 km. However, the Voyager phase measurements showed that the outer scale at 10° S was greater than 100 km, for which the Pioneer 10 measurement is scaled to a minimum of between 20 and 39% [Woo and Yang, 1976]; this is significantly larger than observed by V1. In this regard, the method adopted here for specifying $\delta N_e/N_e$ has the advantage of requiring no assumption about the outer scale of the irregularities, which is difficult to obtain. Furthermore, the V1 observations extend the measurement of $\delta N_e/N_e$ to regions of anisotropic irregularities (altitudes of 1200 to 3600 km), while the Pioneer results apply only for isotropic structures (near 1000 km altitude).

V1 Emersion (0°, 314°W). The average electron density for this region of the ionosphere was significantly lower than was measured by V1 at immersion [Eshleman et al., 1979b]. The spatial irregularities in electron density were too weak to produce appreciable scattering of the 3.6-cm signal. However, weak scattering was observed at 13 cm, and amplitude spectra derived from the two smoothing intervals in Figure 4.5 appear in Figure 4.6. The phase spectra for both smoothing intervals were dominated by noise.

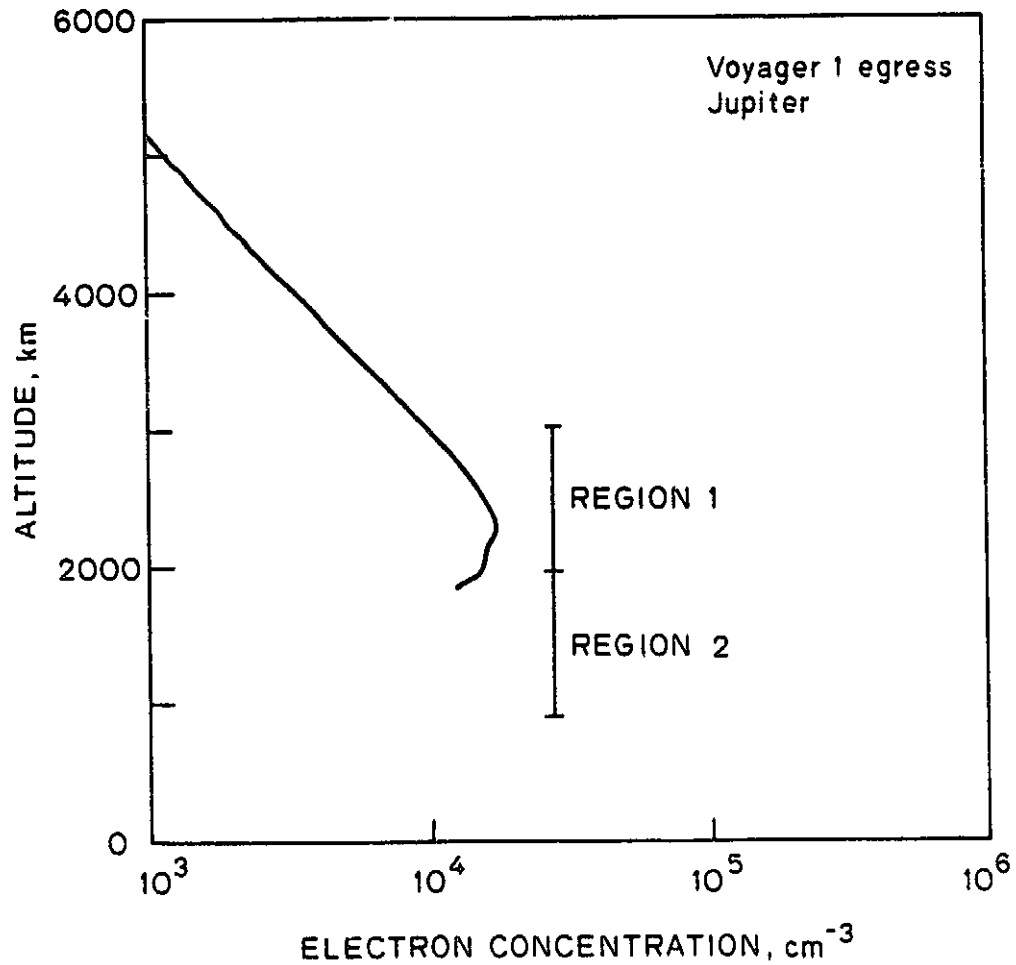

Figure 4.5 Profile of average electron concentration in the upper ionosphere at V1 emersion. Regions 1 and 2 indicate altitude intervals for computing spectra [profile from Eshleman et al., 1979b].

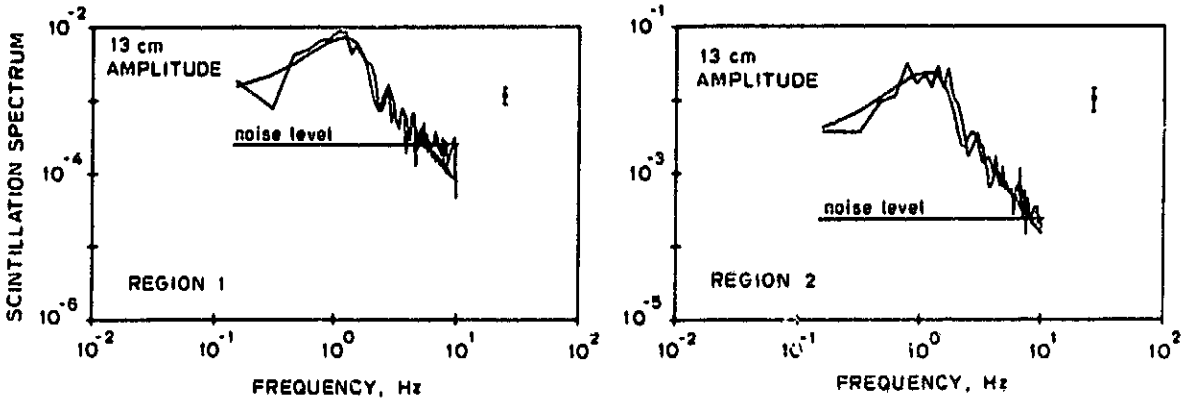

Figure 4.6 Amplitude spectra at 13 cm from the smoothing intervals (regions 1-2) in Figure 4.5. See Figure 4.3 for additional comments.

Table 4.3 Characteristics of irregularities in Jupiter's upper ionosphere at V1 emersion.

Height, km	Spectrum type	γ, degrees	Power-law index	Axial ratio	δN_e, cm^{-3}
1500	13-cm a(t)	62 ± 4.6	3.3 ± 0.13	3.0 ± 0.6	1000 ± 200
2500	13-cm a(t)	68 ± 6.1	3.0 ± 0.19	2.5 ± 0.6	590 ± 100

Table 4.3 lists the least-squares solutions for parameters derived from these two amplitude spectra. The spectrum Φ_n appears to follow an inverse power law, with an exponent of about 3.0 to 3.3. Estimates of magnetic field direction, γ, are mutually consistent. The fluctuations in electron density correspond to fractional variations $\delta N_e/N_e$ of 5 to 10%. Again, the signal fluctuations in this frequency interval result from scattering by ionospheric irregularities of size 2 to 100 kilometers.

V2 Immersion (65°S, 260°W). The 13-cm signal experienced strong scattering as well as multiple-path propagation from steep gradients in electron density; no 13-cm spectra were reduced. The character of the fluctuations at 3.6 cm changed rapidly in this region; the two smoothing intervals in Figure 4.7 indicate the only segments during which the signal fluctuations appeared to be stationary.

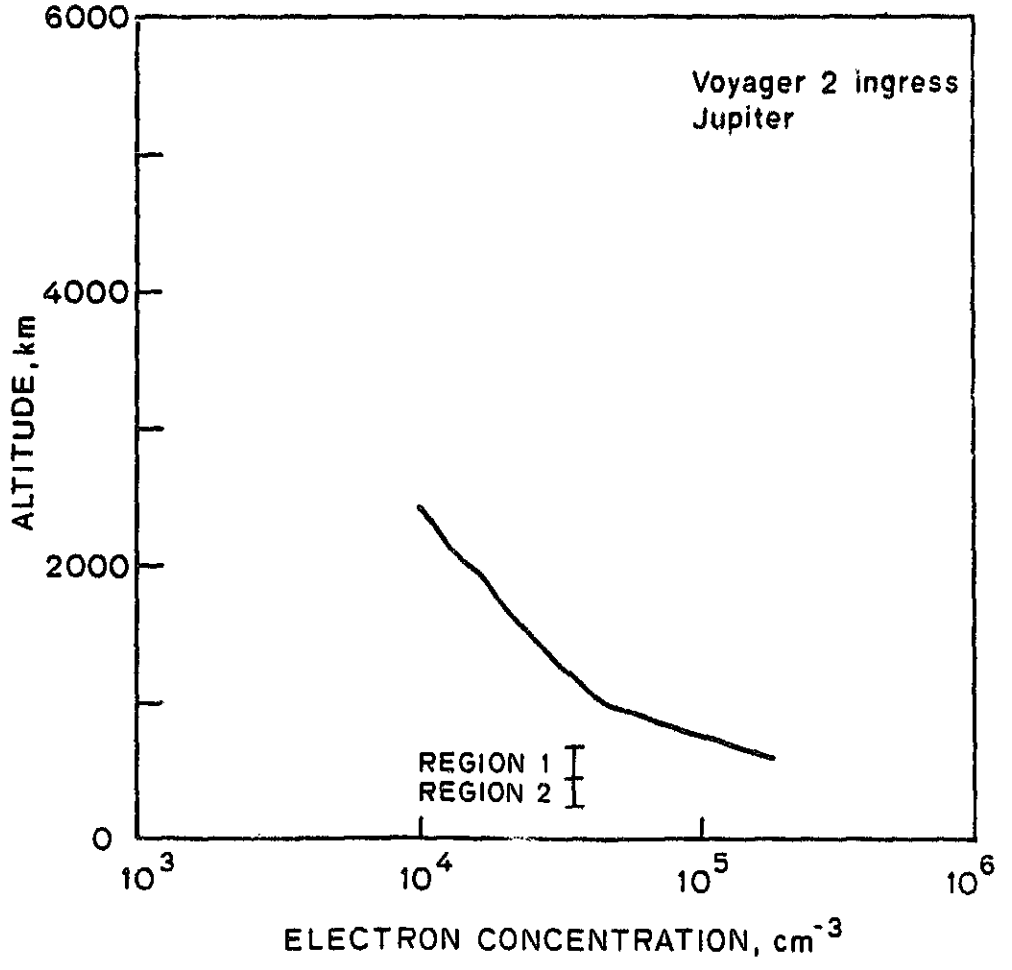

Figure 4.7 Profile of average electron concentration in the upper ionosphere at V2 immersion. Regions 1 and 2 indicate altitude intervals for computing spectra [profile from Eshleman et al., 1979c].

The amplitude and phase spectra at 3.6 cm from these intervals appear in Figure 4.8, except that the phase spectrum of the first interval corresponded to noise and is not shown. Note that the amplitude spectrum obtained in the first interval is not characterisitic of scattering from a power-law distribution of irregularities. At high frequencies, the spectrum levels off at a value well above the noise, possibly as a result of scattering from the disturbances associated with an unstable plasma. In this regard, it is perhaps significant that the ionosphere at V2 immersion lies near the magnetic footprint of the Io flux tube, where particle precipitation may affect the plasma dynamics [M. H. Acuna and N. F. Ness, private communication, 1979; Broadfoot et al., 1979].

The residuals of the best theoretical fits to the spectra from the second smoothing interval were unexpectedly large. Apparently, the plasma irregularities were not statistically homogeneous over the altitude range corresponding to the measurements, so the solutions for parameters derived from these spectra are not reported here. The limited amount of data available and the unique nature of Jupiter's ionosphere in this region restrict further interpretation at this time.

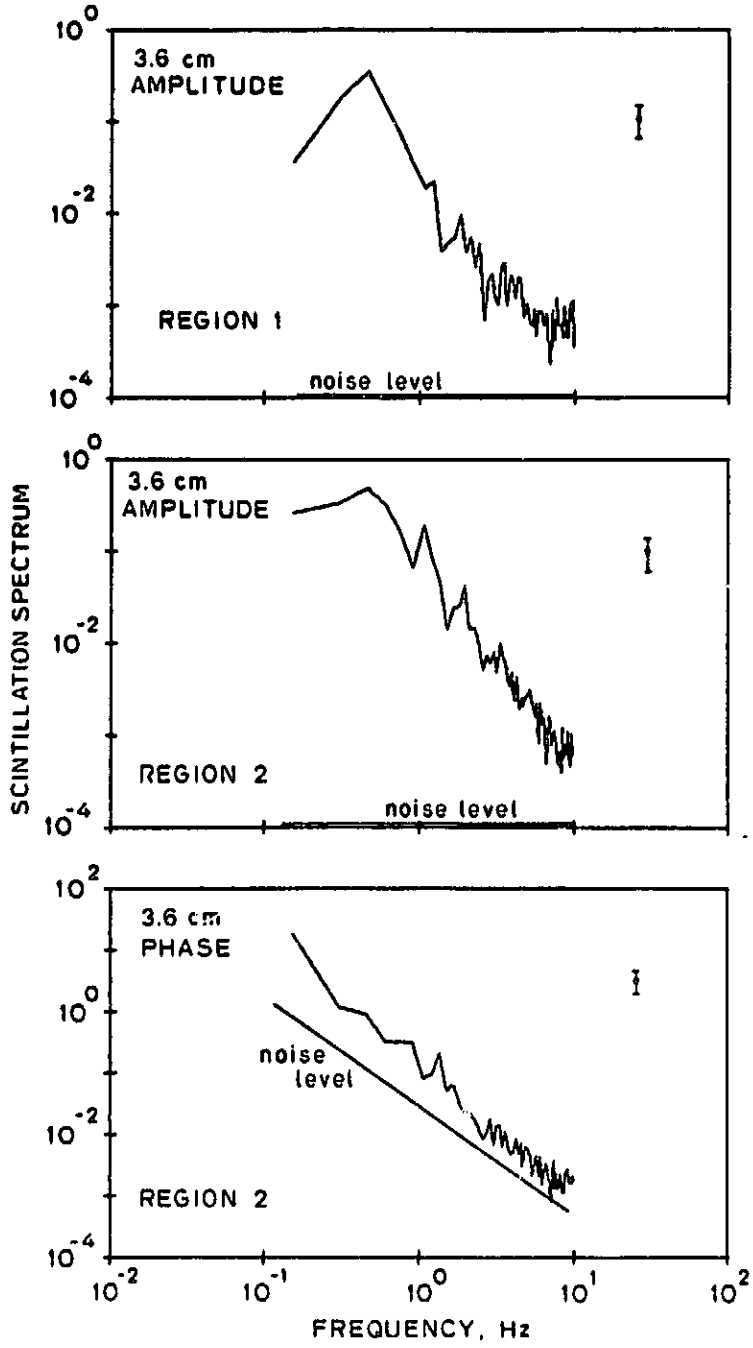

Figure 4.8 Amplitude and phase spectra at 3.6 cm from the smoothing intervals (regions 1-2) in Figure 4.7. See Figure 4.3 for additional comments. No ionospheric parameters were obtained from these data.

V2 Emersion (50°S, 150°W). Two sets of 13-cm spectra, from the regions shown in Figure 4.9, appear in Figure 4.10. Figure 4.11 shows the squared coherency and cross spectrum phase at 13 cm from these regions. The signal fluctuations due to scattering at 3.6 cm exceeded measurement noise only for the amplitude spectrum of the lower altitude smoothing interval.

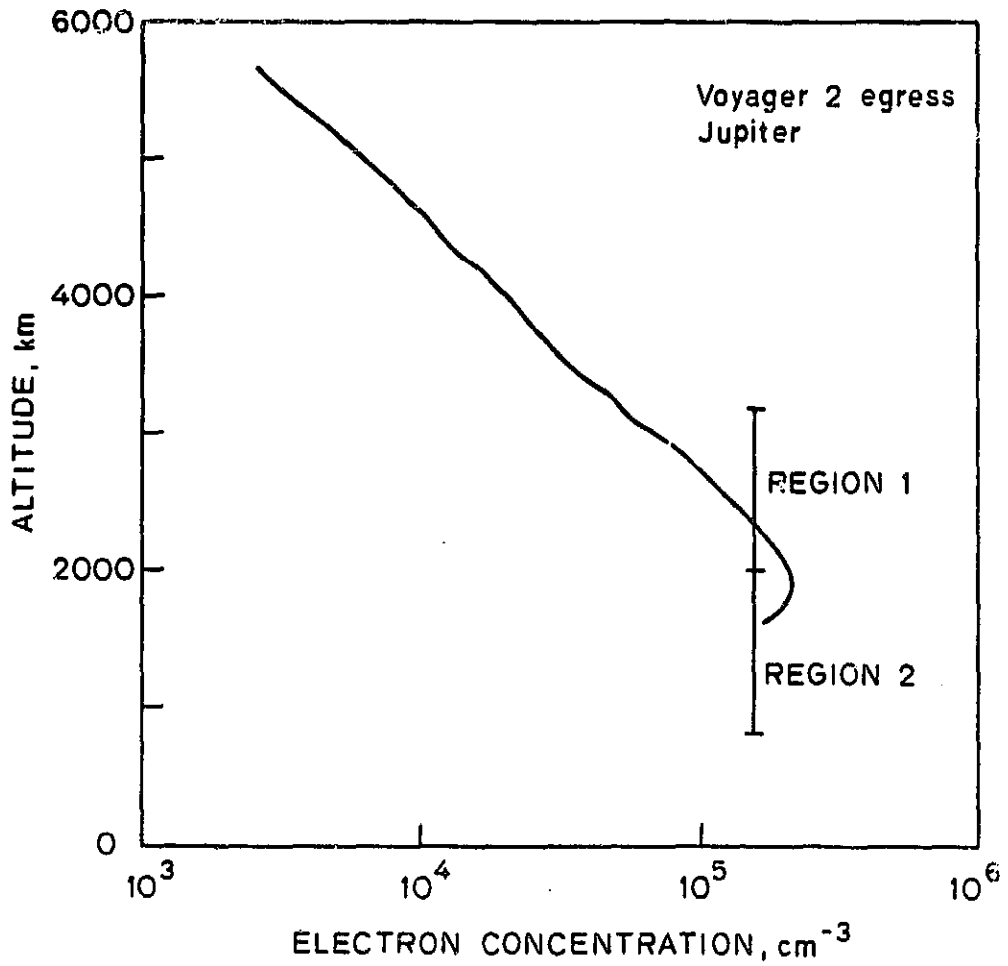

Figure 4.9 Profile of average electron concentration in the upper ionosphere at V2 emersion. Regions 1 and 2 indicate altitude intervals for computing spectra [profile from Eshleman et al., 1979c].

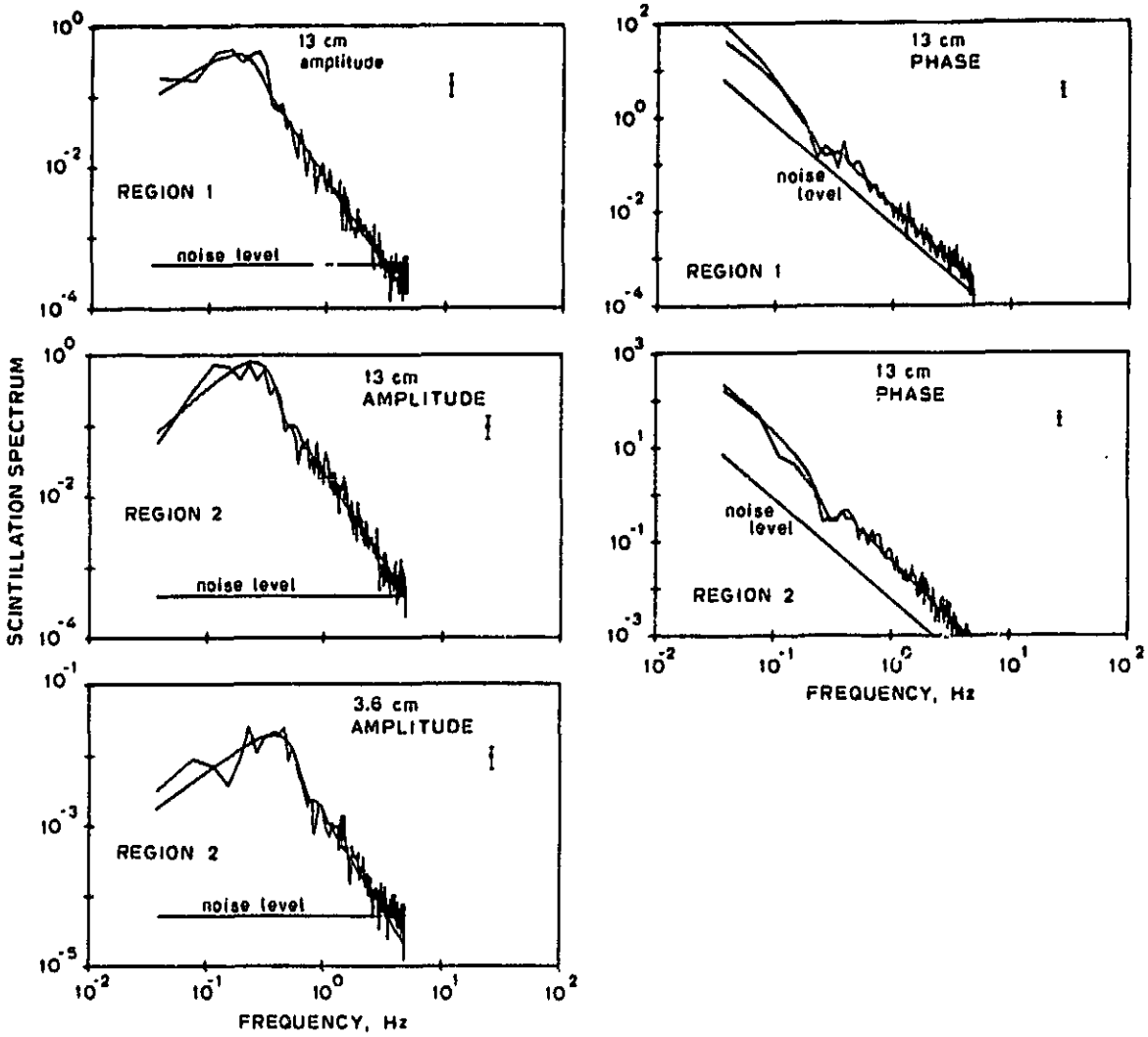

Figure 4.10 Amplitude and phase spectra at 3.6 and 13 cm from the smoothing intervals in Figure 4.9. See Figure 4.3 for additional comments.

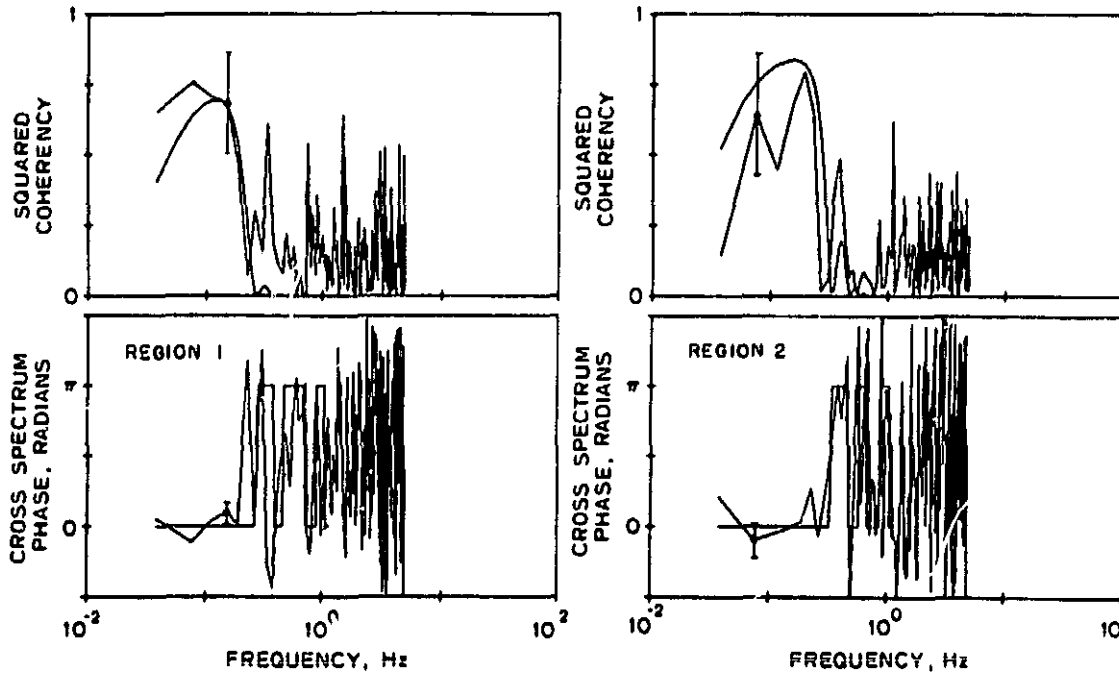

Figure 4.11 Squared coherency and cross spectrum phase at 13 cm from regions 1 and 2 of Figure 4.9. See Figure 4.4 for additional comments.

Table 4.4 Characteristics of irregularities in Jupiter's upper ionosphere at V2 emersion.

Height, km	Spectrum type	γ, degrees	Power-law index	Axial ratio	δN_e, cm^{-3}
1500	13-cm a(t)	37 ± 2.4	3.5 ± 0.05	7.0 ± 1.9	3100 ± 600
1500	13-cm ϕ(t)	34 ± 2.2	3.5 ± 0.04	8.5 ± 2.2	4300 ± 900
1500	3.6-cm a(t)	30 ± 1.9	3.7 ± 0.09	8.0 ± 2.1	3600 ± 700
2500	13-cm a(t)	26 ± 2.4	3.4 ± 0.07	6.0 ± 1.7	1900 ± 400
2500	13-cm ϕ(t)	28 ± 3.2	3.4 ± 0.04	8.0 ± 2.3	2500 ± 500

Table 4.4 lists solutions for parameters derived from amplitude and phase spectra. The five estimates of γ exhibit some spread but seem mutually consistent within the 1-σ uncertainties. The inverse power-law exponent, p, ranges from 3.4 to 3.7. Spatial irregularities of approximate size 2 to 140 kilometers contributed to scattering in the frequency range from 0.04 to 3 Hz. The spatial fluctuations in electron density correspond to fractional variations of 1 to 2% in Jupiter's high latitude ionosphere.

Solutions for ionospheric parameters indicate a large value for the axial ratio over the full altitude range of appreciable signal scattering; this differs from the altitude dependence observed at the same heights in the equatorial ionosphere at V1 immersion (Table 4.2). The GSFC 04 model of Jupiter's magnetic field [Acuna and Ness, 1976] predicts a factor of nearly two between the field magnitudes in the ionosphere at V2 emersion (9.5 Gauss) and V1 immersion (4.8 Gauss). Therefore, the magnetic field controls particle motion more effectively at high latitudes than at the equator, which may account for the strong anisotropy at both altitudes in Table 4.4.

These measurements can be compared with results derived from Pioneer 10 emersion at latitude 59°N. Woo and Yang [1978] reported that $p = 11/3$ over the altitude range in Table 4.4. This is again higher than values determined from the Voyager observations, although the comparison may be inappropriate since the measurements were made at similar latitudes but in opposite hemispheres (also see comments under V1 immersion, above). The axial ratios in Table 4.4 agree with those measured during Pioneer 10 emersion. Woo and Yang [1976] deduced that $\delta N_e/N_e$ is 72% at 1500 km by assuming an outer scale of 100 km.

However, the V2 phase spectra indicate an outer scale in excess of 140 km, which would increase the value of $\delta N_e/N_e$ inferred from the Pioneer data. In either case, the Pioneer result is considerably larger than values reported here, and seems unrealistic. Finally, Woo and Yang [1978] also suggested that the variation of Jupiter's magnetic field strength with latitude may lead to axial ratios that are larger at high latitudes than at the equator. The Voyager results contravene this conclusion -- although the field strength may affect the altitude dependence of the axial ratio, the largest axial ratio observed near the equator (10°S, Table 4.2) is similar to the largest axial ratio observed at higher latitudes (50°S, Table 4.4).

CHAPTER 5

SPATIAL IRREGULARITIES IN SATURN'S UPPER IONOSPHERE

5.1 Introduction

After their encounters with the Jovian system in 1979, Voyagers 1 and 2 successfully obtained additional measurements of the Saturnian system in 1980 and 1981 [Stone and Miner, 1981, 1982]. This reconnaissance followed the first spacecraft flyby of Saturn by Pioneer 11 in 1979 [Dyer, 1980; Opp, 1980; Northrup et al., 1980].

Through analysis of dual-wavelength (13 and 3.6 cm) radio data from the occultations of Voyagers 1 and 2 by Saturn, Tyler et al. [1981a, 1982] derived altitude profiles of the free electron density in Saturn's ionosphere, among other results. As was the case at Jupiter, rapid fluctuations were observed in the radio signals received from the occulted Voyager spacecraft; here, the scintillations are analyzed to determine the morphology of plasma irregularities in Saturn's upper ionosphere. During the occultation of Pioneer 11 by Saturn, no effects due to scattering from the ionosphere could be detected within the limitations of the radio equipment [Woo and Armstrong, 1980].

The next section describes the experimental geometry and the Voyager occultation measurements; Section 5.3 gives the spatial characteristics of Saturn's ionospheric irregularities as deduced from the Voyager scintillation data. In Chapter 6, the magnetic field orientations at two locations are inferred from the alignment of the irregularities. These results have been published elsewhere [Hinson, 1983].

5.2 Experimental Geometry and Measurements

Figure 5.1 shows the view from earth of the Voyager occultations by Saturn. Voyager 1 immersion occurred on November 13, 1980, at 70°S, 307°W, with solar zenith angle δ = 91° (evening). The spacecraft emerged from behind the atmosphere at 2°S, 157°W, δ =86° (early morning). The locations of immersion and emersion for the occultation of Voyager 2 on August 26, 1981, were 31°N, 36°W, δ = 87° (evening) and 26°S, 270°W, δ = 93° (predawn), respectively. All longitudes above are expressed in the Saturn longitude system, or SLS [Desch and Kaiser, 1981]. Radio-wave scattering from electron density structures in the upper ionosphere caused scintillations in the signals received only during V1 immersion and V2 emersion; parameters which characterize these two occultations are listed in Table 5.1. Here, as before, $\vec{v}_*$ is the ray path velocity in the plane of the sky; Δ indicates the orientation of $\vec{v}_*$ (see Figure 6.1); and D is the distance between the spacecraft and limb of Saturn. No scintillations due to scattering were observed during the occultations by the upper ionosphere at V1 emersion or V2 immersion, probably as a result of the limited signal-to-noise ratios and the relatively low average electron densities at these locations; these data will not be discussed further.

Table 5.1 Parameters that characterize the Voyager occultations by Saturn near immersion and emersion.

Space-craft	Lat.[1]	Long.[2]	$\lvert\vec{v}_*\rvert$, km/s	Δ, degrees	D, km	Fresnel-zone radius, km	
						13 cm	3.6 cm
V1	70°S	307°W	17.2	142.	$2.27 \cdot 10^5$	5.44	2.84
V2	26°S	270°W	20.6	358.	$2.07 \cdot 10^5$	5.21	2.72

[1]Planetocentric

[2]SLS [Desch and Kaiser, 1981]

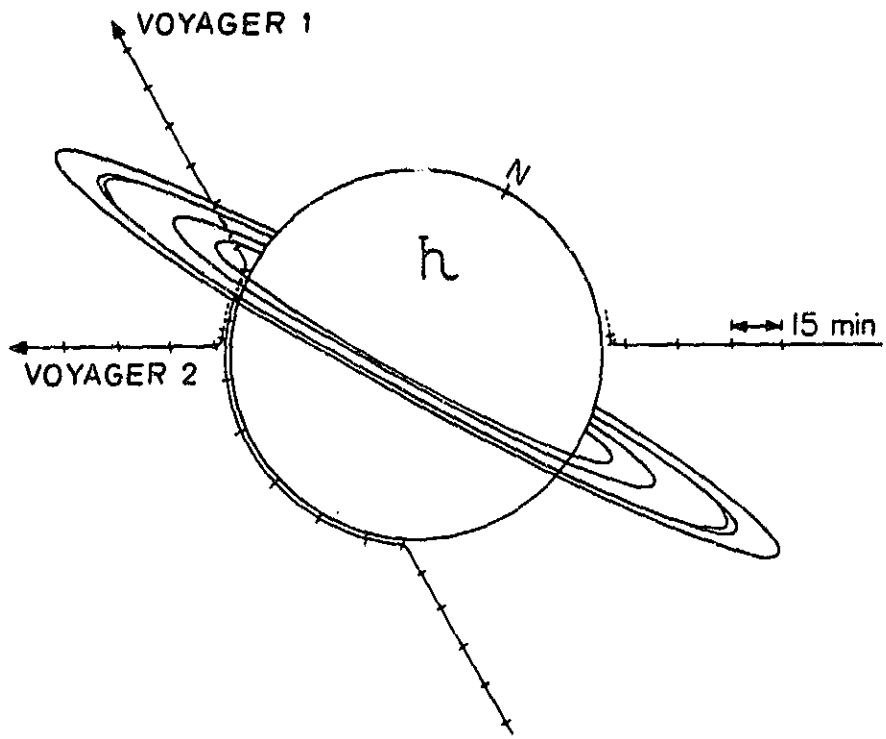

Figure 5.1 Schematic view from earth of the Voyager occultations by Saturn showing the paths followed by the spacecraft radio images.

It should be noted that scintillations were observed in connection with radio-wave propagation through the lower ionosphere at all four locations. These relatively strong perturbations of the received signal are believed to be the result of multiple-path propagation through ionized layers -- similar effects were observed in the Voyager occultation data from Jupiter. In both cases, the weak-scattering theory of Appendix A and the models for ionospheric irregularities in Chapter 2 are inappropriate for interpreting these data. The discussion in the remainder of this chapter pertains only to scattering from the topside ionosphere.

Again following the procedure for preliminary data reduction (Section 3.2), values of signal frequency, f(t), and amplitude, A(t), were measured each 0.064 s for V1 immersion at both wavelengths, 0.041 s for V2 emersion at 13 cm, and 0.027 s for V2 emersion at 3.6 cm. When displayed on an Argand diagram, the scintillations resulting from propagation through Saturn's ionosphere are similar in appearance to those plotted in Figure 3.1 for V1 immersion at Jupiter, with the exception that strong scattering was not observed at the 13-cm wavelength [cf. Hinson, 1983]. These values of f(t) and A(t) were reduced by the methods in Sections 3.3 and 3.4 that were applied previously to data from Jupiter (Chapter 4). The temporal spectra for phase, $\phi(t)$, and normalized amplitude, a(t), are discussed below, along with the solutions for the four ionospheric parameters.

5.3 Results

V1 Immersion (70°S, 307°W). Figure 5.3 displays two 13-cm amplitude spectra from the altitude intervals in Figure 5.2, with the best-fit theoretical spectra superimposed. The indicated noise levels were derived from measurements preceding ingress (see Section 3.4); weak scattering from ionospheric irregularities accounts for that portion of the scintillation spectra that exceeds the noise level. The 13-cm phase spectra from both intervals, as well as all 3.6-cm spectra, were dominated by noise and are not shown.

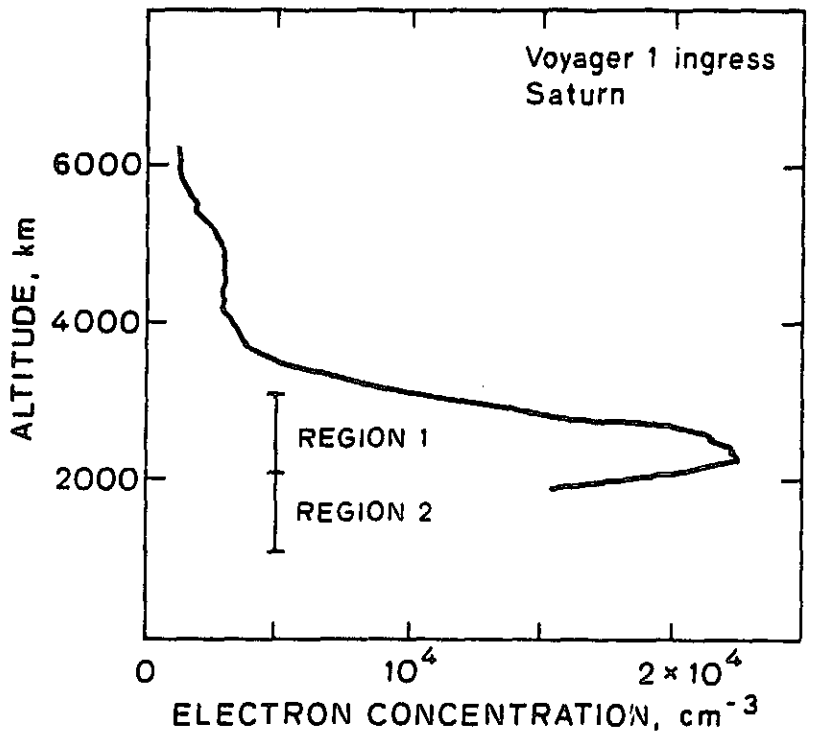

Figure 5.2 Average electron concentration as a function of altitude above the 1 bar pressure level for the upper ionosphere at V1 immersion [profile from Tyler et al., 1981a]. Regions 1 and 2 indicate altitude intervals for computing the spectra in Figure 5.3.

Least-squares solutions for ionospheric parameters were derived from the amplitude spectra; the results are listed in Table 5.2, with the 1-σ uncertainties. The altitude assigned to a measurement again corresponds to the center of the appropriate smoothing interval. Above 1 Hz, the decrease in the amplitude spectra is consistent with an inverse power-law distribution of irregularities with exponent near 3.5, similar to values observed at Jupiter [see Section 4.3; Woo and Yang, 1978] and the earth [Dyson et al., 1974; Phelps and Sagalyn, 1976]. As with Jupiter, Saturn's magnetic field orientation should not vary appreciably with radius over the extent of the upper ionosphere, so the lack of variation in the estimates of γ was expected.

Recall that under the assumption of "frozen" irregularities, there is a direct proportionality between the frequency of signal fluctuations and the size of the scattering structures (see Section 4.3). Using this interpretation, irregularities of approximate size 3 to 60 km contribute to scattering over the frequency range in Figure 5.3. These lower and upper limits result from noise limitations and the length of the measurement time interval, respectively, and do not represent either inner or outer scales. The spatial variations in electron density, δN_e, listed in Table 5.2 refer only to irregularities in this size interval, and correspond to fractional density variations of about 10%.

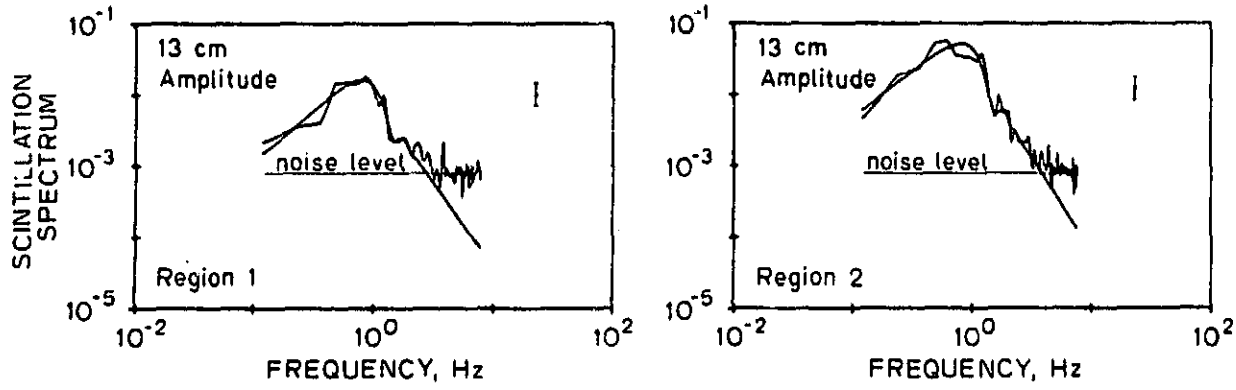

Figure 5.3 Spectra of scintillations in 13-cm amplitude from the smoothing intervals in Figure 5.2. The 1-σ uncertainties apply at all sample frequencies. Theoretical spectra (smooth curves superimposed) were fitted in a least-squares sense to the measured spectra over the frequency range where the scintillations due to scattering exceeded the noise level by at least 3 dB.

Table 5.2 Characteristics of irregularities in Saturn's upper ionosphere at V1 immersion.

Height, km	Spectrum type	γ, degrees	Power-law index	Axial ratio	δN_e, cm^{-3}
1600.	13-cm a(t)	29 ± 2	3.6 ± 0.1	11 ± 3	2600 ± 500
2600.	13-cm a(t)	27 ± 2	3.3 ± 0.2	12 ± 3	1300 ± 300

V2 Emersion (26°S, 270°W). Plasma irregularities produced weak scattering at both wavelengths during the occultation by the upper ionosphere. The amplitude and phase spectra appearing in Figure 5.5 were computed over the altitude intervals in Figure 5.4; in the intervals where phase spectra are absent, noise dominated the measurements. The best-fit theoretical spectra are superimposed in Figure 5.5.

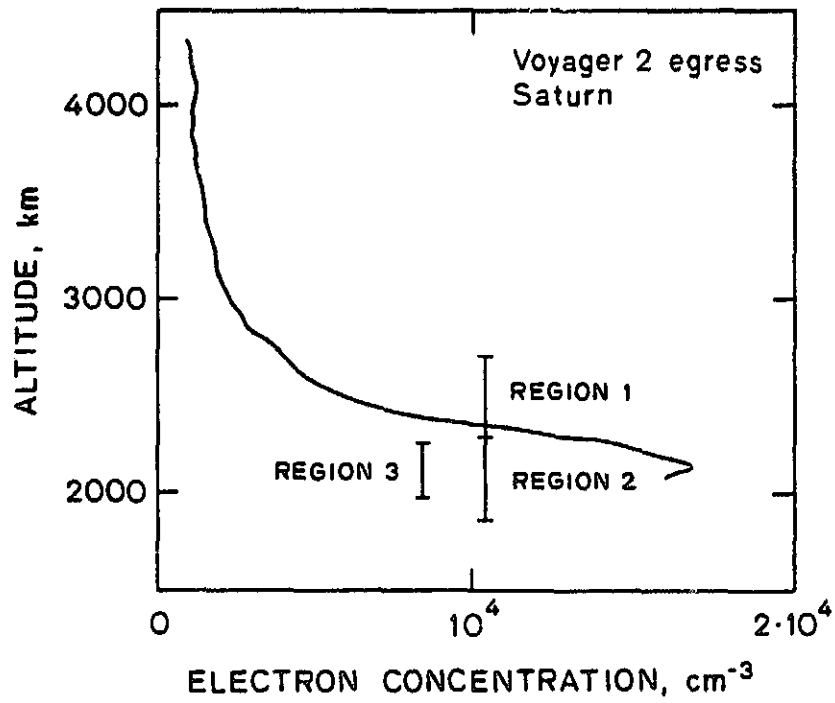

Figure 5.4 Average electron concentration as a function of altitude above the 1 bar pressure level for the upper ionosphere at V2 emersion [profile from Tyler et al., 1982]. Regions 1-3 indicate altitude intervals for computing the spectra in Figures 5.5 and 5.6.

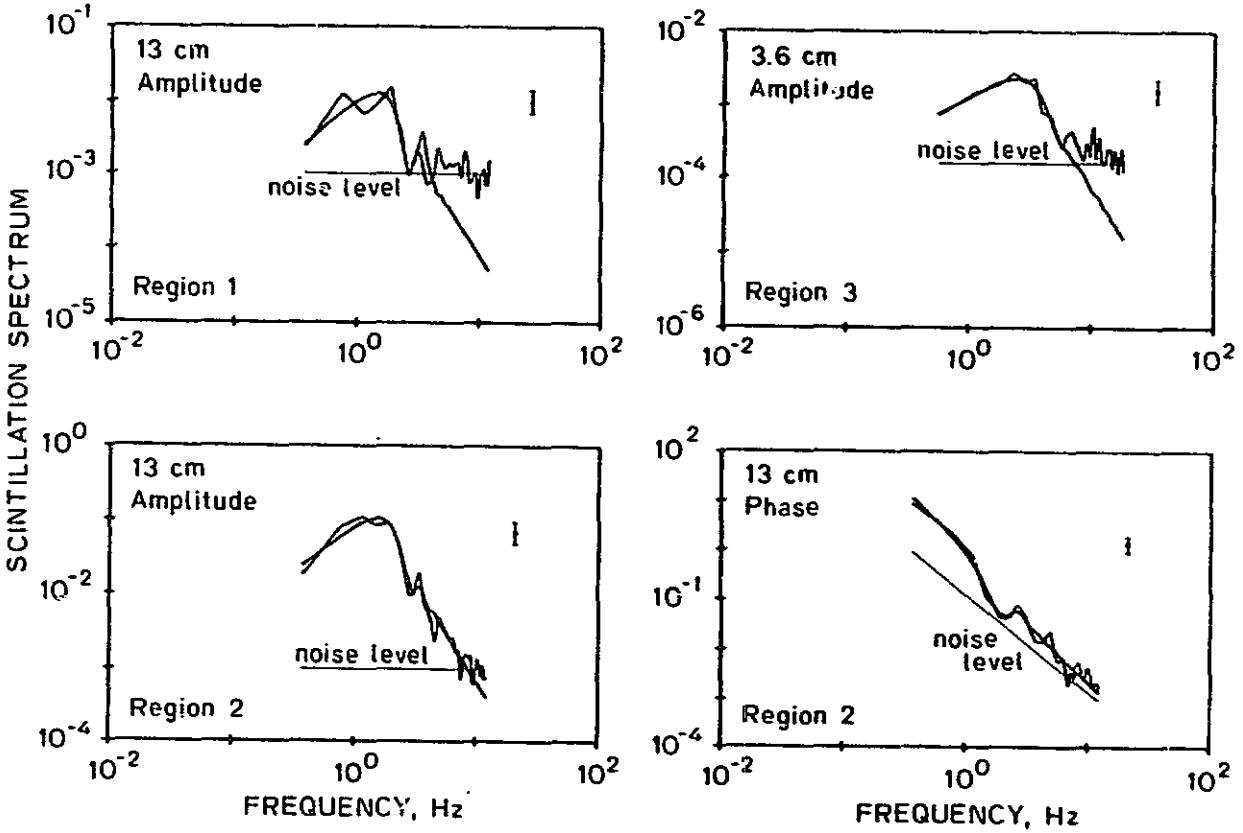

Figure 5.5 Spectra of scintillations in 13-cm amplitude and phase and 3.6-cm amplitude from the smoothing intervals in Figure 5.4. See Figure 5.3 for additional comments.

For completeness and as a test of the theory, the squared coherency and cross spectrum phase from region 2 of Figure 5.4 are shown in Figure 5.6. The high-frequency portion of the spectra corresponds to measurement noise for which the cross spectrum phase has a random distribution. Using the parameters obtained through analysis of the amplitude and phase spectra, the theoretical squared coherency and cross spectrum phase were computed and superimposed in Figure 5.6. The parameter measurements are consistent with the theory, as indicated by the general agreement between curves in each panel.

Table 5.3 lists solutions for parameters derived from amplitude and phase spectra, with 1-σ uncertainties. On the basis of the close agreement between the measurements and the theory, the spatial spectrum of irregularities is consistent with an inverse power law with exponent near 3.5. The four measurements of γ are mutually consistent. These signal fluctuations were caused by anisotropic irregularities of approximate size 2 to 40 km (over the frequency interval where the scintillations exceeded the noise). The values of δN_e apply only for this range of sizes and correspond to fractional variations in density of about 20%.

The measurements of axial ratio in Tables 5.2 and 5.3 show the same variation with altitude and latitude as was previously observed at Jupiter (see Tables 4.2 and 4.4). The axial ratio apparently increases with altitude at V2 emersion where Saturn's magnetic field is relatively weak (0.24 Gauss), while the increased field strength at V1 immersion (0.61 Gauss) is believed to be responsible for the large axial ratios at both altitudes. (Both magnetic field magnitudes were calculated from a model proposed by Connerney et al. [1982]).

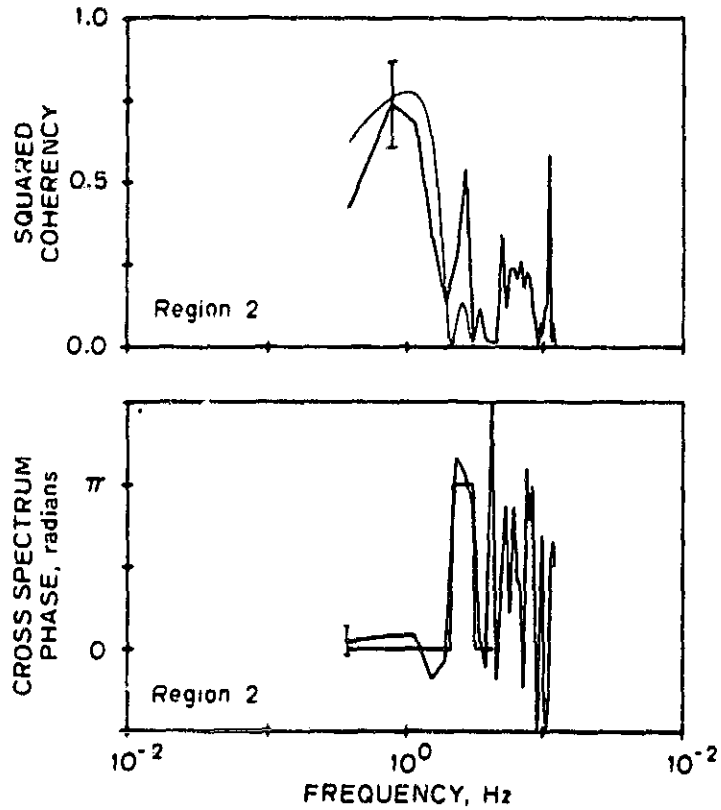

Figure 5.6 Squared coherency and cross spectrum phase at 13 cm from region 2 of Figure 5.4. The 1-σ uncertainties are indicated at one frequency. The high frequency portion of each spectrum corresponds to measurement noise for which the cross spectrum phase has a random distribution. Theoretical curves are superimposed at frequencies below 4 Hz.

Table 5.3 Characteristics of irregularities in Saturn's upper ionosphere at V2 emersion.

Height, km	Spectrum type	γ, degrees	Power-law index	Axial ratio	δN_e, cm^{-3}
2100.	13-cm a(t)	46 ± 3	3.6 ± 0.2	7 ± 3	3500 ± 700
2100.	13-cm φ(t)	43 ± 4	3.4 ± 0.2	5 ± 2	5500 ± 1100
2100.	3.6-cm a(t)	41 ± 6	3.6 ± 0.4	4 ± 2	3600 ± 700
2500.	13-cm a(t)	42 ± 3	3.5 ± 0.4	11 ± 6	1200 ± 300

CHAPTER 6

MAGNETIC FIELD ORIENTATIONS IN THE IONOSPHERES OF JUPITER AND SATURN

6.1 Introduction

In this chapter, magnetic field orientations in the ionospheres of Jupiter and Saturn are inferred from the occultation measurements in Chapters 4 and 5. Section 6.2 describes the procedure for deducing the field direction; Sections 6.3 and 6.4 report results for Jupiter and Saturn, respectively. Comparisons with the predictions of magnetic field models are included for both planets. The chapter ends with a discussion of results in Section 6.5.

In summary, at Jupiter, the occultation measurements conflict with the predictions of current field models, which apparently do not accurately represent the field near the planet. However, when used as a test of Saturnian magnetic field models, the occultation measurements generally confirm the model predictions, but also suggest that a small adjustment of model parameters might improve the field representation.

6.2 The Inference of Magnetic Field Orientation from Occultation Measurements

It has been assumed here that the ionospheric irregularities are field aligned and symmetrical with respect to rotations about the field direction (cf. Section 2.3.1). Hence, the measurements of the orientation, γ, in Tables 4.2-4.4, 5.2, and 5.3 are related to the magnetic field directions in the ionospheres of Jupiter and Saturn. To understand the constraint provided by these measurements, recall that the scintillation spectra are sensitive only to refractive variations in

the plane that is perpendicular to the direction of microwave propagation; the spectra are essentially unaffected by variations along the propagation path (cf. Appendix A). Consequently, only the field component that is perpendicular to the direction of propagation will introduce anisotropy into the plasma structures in a way that can influence these occultation measurements. The ϕ component of the planetary field (in a spherical r, θ, ϕ representation) was nearly tangent to the propagation path for each of the Voyager occultations by Jupiter and Saturn. This geometry allows a determination of the relative sizes of the r and θ field components, but no information concerning the ϕ component can be obtained through scintillation techniques. Although the ϕ component affects the angle of polarization of the microwave signals through the phenomenon of Faraday rotation, the right-hand circular polarization of the signals transmitted by Voyager was unsuitable for observations of this effect.

There are two ambiguities in the reduction of these observations to field orientation. First, a reversal of field direction would not affect the ionospheric irregularities; this results in a 180° uncertainty in γ. Second, the theoretical spectra are sensitive only to the absolute value of γ, which allows two possible mirror image solutions for the orientation [cf. equations A36 and 2.4]. Both ambiguities were resolved by choosing the field orientation that minimizes the difference between the occultation measurements and current Jovian or Saturnian magnetic field models. Other possible solutions for the orientation are well separated from the model predictions, which can be seen by considering Figure 6.1, below, and the angles in Tables 4.1-4.4, 5.1-5.3, and 6.1-6.2.

Field Orientations

To facilitate comparisons with magnetic field models in the next two sections, the field orientations inferred from occultation measurements are expressed in terms of Γ, the angle measured clockwise relative to the outward radial direction on the visible limb of the planet, as defined in Figure 6.1. This angle follows directly from the measurements of γ (Tables 4.2-4.4, 5.2, and 5.3) through the angle Δ, which defines the geometry of the occultations (Tables 4.1 and 5.1). At Saturn, a small additional correction to Γ (-1° for V1, +2° for V2) has been included to account for the motion of the ionosphere across the propagation path that results from Saturn's rotation and the slight inclination of the rotation axis at the time of the occultations. Due to the small inclination of Jupiter's rotation axis during the Voyager encounters, this correction is negligible at Jupiter.

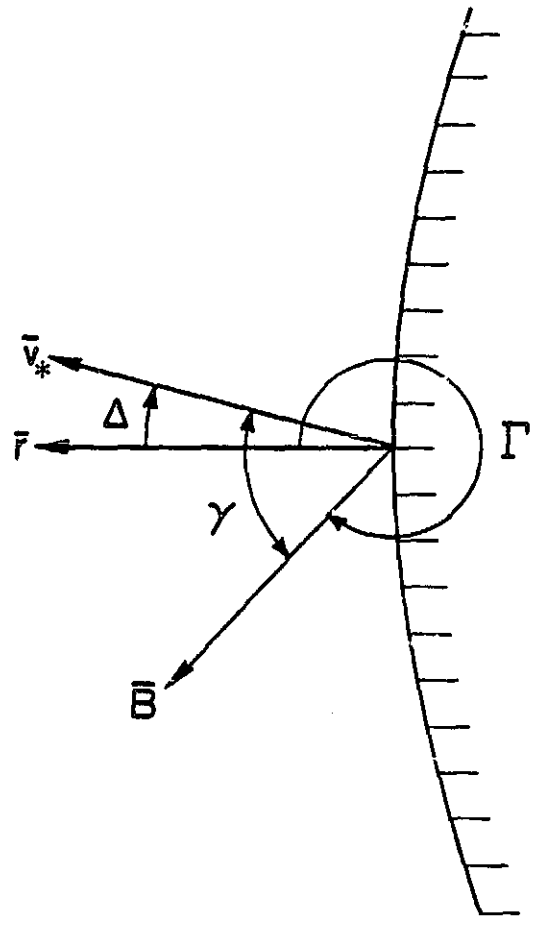

Figure 6.1 View from earth of the visible limb of the occulting planet (Jupiter or Saturn) showing the raypath velocity, $\vec{v}_*$, and the component of the planetary magnetic field, $\vec{B}$, that is perpendicular to the line of sight. The angles Δ and Γ are measured clockwise relative to the outward radial direction, $\vec{r}$, at the occultation point.

6.3 Magnetic Field Orientations in Jupiter's Ionosphere

Although numerous models for Jupiter's magnetic field have been proposed [cf. Smith et al., 1976], only four will be considered here; each is based on magnetometer measurements obtained during the Pioneer 11 (P11) flyby. Acuna and Ness [1976] fitted a third-order spherical harmonic expansion to the flux gate magnetometer (FGM) data recorded between 1.7 and 6 Jupiter radii to produce Model 1 (GSFC 04). In this representation, the observed magnetic field is attributed entirely to sources internal to Jupiter; external sources are neglected. Smith et al. [1976] derived Model 2 (P11 3I 1E) through analysis of the P11 vector helium magnetometer (VHM) data. This spherical harmonic expansion includes a dipole representation for the sources external to Jupiter in addition to a third-order expansion for internal sources. Connerney [1981] proposed Models 3 and 4 after independently analyzing the P11 FGM and VHM data, respectively, in the following manner. First, the Pioneer 10, V1, and V2 magnetometer data were used to construct a model for the magnetic field arising from currents in the Jovian magnetosphere. Next, this model was applied to remove the contribution by external sources from the P11 data. When used as input for a generalized inverse analysis, the resultant field yielded a third-order spherical harmonic model of Jupiter's internal field for each data set.

Table 6.1 summarizes the results for the magnetic field orientation in Jupiter's ionosphere, and includes comparisons with the four models just described. The third column lists occultation measurements of Γ at the locations specified in the first two columns. Columns 4 to 7 give predictions of Γ from the four Jovian magnetic field models. Relative to the 1-σ measurement uncertainties, the differences between the

occultation measurements and the predictions of all four models are significant. No discussion of the Pioneer occultation measurements of field orientation [Woo and Yang, 1978] is included here, since those results did not include measurement uncertainties, and comparisons with magnetic field models are therefore inconclusive.

As mentioned previously (Section 4.3), the field orientation should not vary appreciably with radius over the vertical extent of Jupiter's upper ionosphere. Nevertheless, in response to the longitudinal structure in the magnetic field, the orientation does vary slightly with position along the radio path within the ionosphere. This path dependence has been included in computing an effective Γ from the four models; these values and the measurements in Table 6.1 should be interpreted as local spatial averages of the field orientation in Jupiter's ionosphere. However, if the total variation along the raypath is not larger than a few degrees, this effect cannot account for the differences between the predictions of the field models and the occultation measurements.

Table 6.1 Jupiter's magnetic field orientation at ionospheric heights.

		Γ, Magnetic Field Angle, degrees				
		Occultation			Connerney [1981]	
Lat.[1]	Long.[2]	Measurement	GSFC 04	P11 3I 1E	FGM	VHM
10°S	63°W	119 ± 2.4	136	136	137	132
		119 ± 1.8				
		117 ± 1.7				
		117 ± 1.7				
		119 ± 1.0				
		117 ± 1.6				
0°	314°W	303 ± 4.6	284	288	283	290
		297 ± 6.1				
50°S	150°W	200 ± 2.4	196	196	197	197
		203 ± 2.2				
		207 ± 1.9				
		211 ± 2.4				
		209 ± 3.2				

[1]Planetocentric

[2]Sys III, 1965 [Seidelmann and Divine, 1977]

6.4 Magnetic Field Orientations in Saturn's Ionosphere

The first models of Saturn's magnetic field were derived from P11 magnetometer data, and consisted of a dipole aligned with the rotation axis but with its center offset northward by 0.04 R_S, where R_S is Saturn's radius [Smith et al., 1980a, b; Acuna and Ness, 1980; Acuna et al., 1980]. Spacecraft observations of the charged particle absorption signatures of Saturn's moons and rings also supported the "offset dipole" (OD) model [Chenette and Davis, 1982]. Through subsequent analysis of the combined V1 and V2 magnetometer data, Connerney et al. [1982] derived the "Z3" model for Saturn's field, which consists of the first three zonally symmetrical terms in a spherical harmonic expansion. Aside from a nonzero octupole coefficient, g_3^0, in the Z3 expansion, the two models are essentially the same -- both are symmetrical about Saturn's rotation axis and include no ϕ component. As the importance of the octupole term decreases rapidly with increasing distance from Saturn, the charged particle absorption signatures are also consistent with the Z3 model [Acuna et al., 1982].

Table 6.2 summarizes results for the magnetic field orientation in Saturn's ionosphere at the locations specified in the first two columns. The third column lists occultation measurements of Γ, the angle of Saturn's field component perpendicular to the line of sight as defined in Figure 6.1. For comparison, predictions of Γ from the OD and Z3 magnetic field models appear in the last two columns. The difference between the two theoretical values at each location illustrates the effect of g_3^0 on the field representation at ionospheric heights. At both locations in Table 6.2, the occultation measurements are intermediate to the predictions of the two models; within the

measurement uncertainties, each model is in reasonable agreement with the occultation results (also see Figures E3 and E4 of Appendix E).

As mentioned previously, the occultation measurements in Table 6.2 should be regarded as local spatial averages. The systematic variation of Γ along the radio path in Saturn's ionosphere was calculated on the basis of both the OD and Z3 models and the geometry of the Voyager occultations. Unlike the case at Jupiter, this effect was found to be insignificant when compared with the measurement uncertainties.

Table 6.2 Saturn's magnetic field orientation at ionospheric heights.

		Γ, Magnetic Field Angle, degrees		
Lat.[1]	Long.[2]	Occultation Measurement	Z3	OD
70°S	307°W	170 ± 2	166	171
		168 ± 2		
26°S	270°W	226 ± 3	229	221
		223 ± 4		
		221 ± 6		
		222 ± 3		

[1]Planetocentric

[2]SLS [Desch and Kaiser, 1981]

6.5 Discussion

When comparing the occultation observations to the model predictions at Jupiter (Table 6.1) and Saturn (Table 6.2), it is important to note certain limitations of the spacecraft magnetometer data [Connerney, 1981]. First, at Jupiter, the P11 FGM and VHM data are incompatible in the sense that systematic differences between the two sets of field measurements are unexpectedly large. Second, when deriving field models from magnetometer data, the representation for the internal field is sensitive to assumptions about the fields of external origin and to the alternative methods of data inversion; consequently, there are substantial differences among the four Jovian field models mentioned in Section 6.2 (see Figures 14 and 15 of Connerney [1981]). Finally, magnetometer measurements along a spacecraft flyby trajectory are insufficient to produce a unique model of a planet's internal magnetic field. Because of these limitations, complementary measurements, such as the field orientations inferred from Voyager radio occultations, could provide valuable information on the Jovian and Saturnian fields.

Jupiter's magnetic field is more complex than that of a simple dipole -- it has significant quadrupole and octupole moments [Smith and Gulkis, 1979]; the same may be true of Saturn's magnetic field [Connerney et al., 1982]. In a spherical harmonic representation, dipole terms vary as r^{-3}, quadrupole terms vary as r^{-4}, and octupole terms are proportional to r^{-5}. Consequently, the quadrupole and octupole terms in the expansion are relatively more important in the ionosphere than at the remote position of spacecraft magnetometer measurements. Therefore, in principle, the field orientations inferred

from radio occultations can provide a sensitive test for deviations from zonal symmetry in the magnetic field, and a basis for improving the higher-order coefficients in field models.

Unfortunately, occultation measurements at three locations for Jupiter and two locations for Saturn provide only a weak constraint on the twelve quadrupole and octupole terms in the respective fields. The difficulties in modifying Saturnian field models are compounded by the current uncertainty in Saturn's rotation rate, which can introduce up to ±40° of error in longitude during the interval between the V1 and V2 encounters [Desch and Kaiser, 1981]. Furthermore, in adjusting the model parameters, the residuals of both the occultation measurements and magnetometer data must be considered, which is beyond the scope of this research; no specific revisions to present field models are proposed here.

Nevertheless, two general conclusions can be drawn from the results in Tables 6.1 and 6.2. First, at Jupiter, current models are apparently inadequate for accurately representing the field near the planet. The large discrepancies between the occultation measurements and model predictions in Table 6.1 may be the result of complicated but as yet unknown fine structure in Jupiter's magnetic field. Second, at Saturn, a small adjustment of the coefficients in current field representations would remove the differences between the model predictions and occultation measurements. For example, a field model with a g_3^0 coefficient intermediate to the values in the Z3 (2743 nanotesla) and OD (0 nanotesla) representations would agree more closely with the occultation results at both locations in Table 6.2. A 20% reduction of g_3^0 in the Z3 model would change the predictions for Γ by +1° at 70°S

and -2° at 26°S. Alternatively, the g_3^0 coefficient in the Z3 model could be retained, a possibility which is preferred by Northrup and Hill [1983], and the discrepancies in Table 6.2 could be reduced by assigning small nonzero values to other octupole or higher order coefficients (e.g., g_4^0) in the field expansion.

CHAPTER 7

INTERNAL GRAVITY WAVES IN TITAN'S ATMOSPHERE

7.1 Introduction

The flyby of the Saturnian system by Voyager 1 included a radio occultation by Titan on November 12, 1980 [Stone and Miner, 1981]. Tyler et al. [1981a] and Lindal et al. [1983] analyzed the average effect of Titan's atmosphere on the two radio signals transmitted by the spacecraft and received on the earth, and thereby derived vertical profiles of gas refractivity, molecular number density, pressure, and temperature. Through subsequent analysis of the occultation signals, Lindal et al. [1983] also showed that there was neither measurable microwave absorption in the neutral atmosphere nor a detectable free electron density in the ionosphere. This chapter considers the relationship between rapid signal fluctuations during the occultation and small-scale irregularities in Titan's neutral atmosphere. These scintillation data provide the only information presently available concerning atmospheric structure and dynamics on length scales from a few hundred meters to a few kilometers in the troposphere and stratosphere.

Section 7.2 describes the experimental geometry of the Voyager occultation by Titan and the fundmental measurements. In Section 7.3, spatial characteristics of the atmospheric irregularities are determined from the reduced scintillation data; in addition, the altitude dependence of the intensity variance is calculated. Section 7.4 interprets these results, and confirms the hypothesis that freely propagating internal gravity waves are present in Titan's upper

atmosphere. In addition, wave parameters, including the vertical fluxes of energy and momentum, are estimated, and the source of the gravity waves is considered. These results have been published elsewhere [Hinson and Tyler, 1983].

7.2 Experimental Geometry and Measurements

Figure 7.1 shows a trajectory pole view of the Voyager 1 occultation by Titan; the direction to earth is upward. Occultation immersion occurred near latitude 6°N, solar zenith angle $\delta = 94°$ (evening), with emersion about 11 minutes later at 9°S, $\delta = 86°$ (early morning). (The orientation of Titan's pole is currently unknown, but is assumed to be normal to the mean orbital plane [Davies et al., 1980]. Hence, these latitudes are approximate.) Before immersion, the spacecraft antenna boresight was offset 0.11° in order to compensate for this amount of refraction. This configuration allowed complete amplitude and frequency measurements at both radio wavelengths for the tenuous upper part of Titan's atmosphere. Before emersion, the antenna boresight was repositioned to be 2.36° from earth line, which then allowed amplitude and frequency measurements at the 13-cm wavelength over the maximum possible range in pressure. However, the 3.6-cm data were of limited value in this orientation because of the relatively narrow antenna beamwidth at this wavelength. (Half-power width of the spacecraft antenna pattern is 2.5° at 13 cm and 0.6° at 3.6 cm). For this reason, the 3.6-cm data from emersion will not be discussed further; however, these data should be considered in future work, as the signal was detected briefly. These antenna positions were chosen to insure good results despite significant a priori uncertainties in the

size, orbital position, and atmospheric density of Titan [Tyler et al., 1981a; Lindal et al., 1983].

In order to be consistent with the notation used in the literature, the observations during the occultation by Titan's neutral atmosphere are reported in terms of signal intensity rather than amplitude (cf. Section 3.3). As discussed in Section A.7 of Appendix A, this change is insignificant for the case of weak scattering.

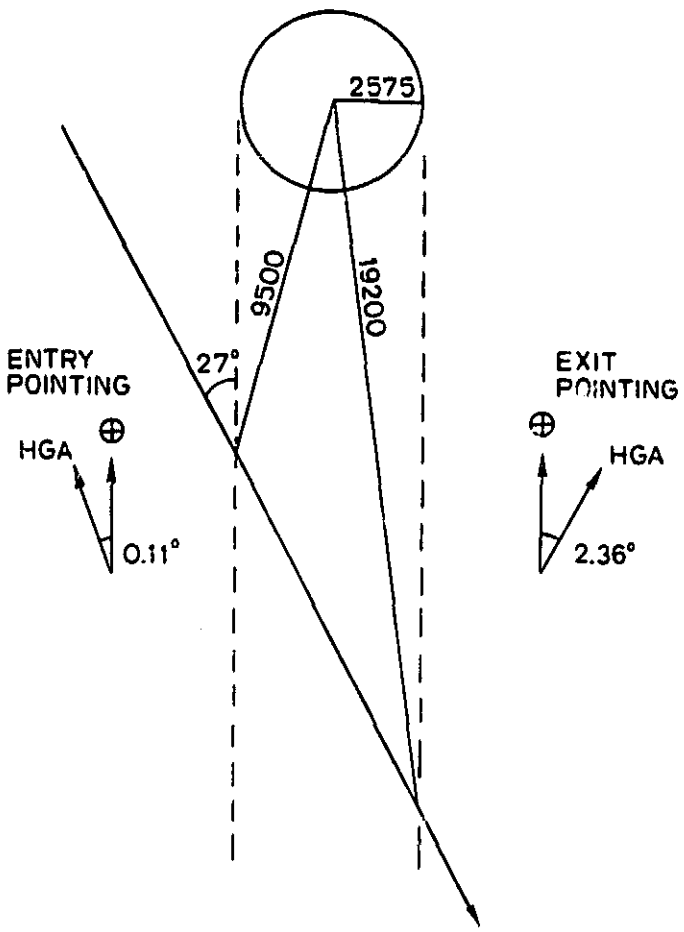

Figure 7.1 Trajectory pole view of Titan. Direction to earth is upward and the antenna orientations for immersion and emersion are indicated.

Values of signal frequency, f(t), and intensity, I(t), were measured (Section 3.2) each 0.041 s for immersion at 13 cm, 0.027 s for immersion at 3.6 cm, and 0.082 s for emersion at 13 cm. Limitations of the radio equipment and observation time resulted in standard deviations in the estimates of f(t) and I(t) of approximately 0.7 Hz and 7%, respectively, before immersion, and 1.5 Hz and 23% after emersion. These values of I(t) are used below to plot the time history of intensity (Figure 7.2) and to calculate scintillation spectra (Figure 7.3). The signal parameters also were measured at one half this sampling rate. These alternate values of I(t) have reduced noise effects, and therefore are preferable for determining the altitude profile of the intensity variance (Figure 7.5).

Intensity profiles for immersion at 3.6 and 13 cm, and emersion at 13 cm appear in Figure 7.2. To facilitate comparison, the time scale for emersion has been reversed and compressed to compensate for geometrical differences between immersion and emersion. In the first segment of each profile, where the average intensity remained constant, the radio path from spacecraft to earth was above Titan's atmosphere. During the occultation, the general shape of each curve was determined by the combined effects of atmospheric refraction and antenna pointing [cf. Lindal et al., 1983; also see Appendix D]. The 13-cm signal was received throughout both immersion and emersion except when it was blocked by Titan's surface, while the 3.6-cm signal was lost in the noise because of the antenna pattern effects before the surface was reached. The altitude of ray periapsis relative to Titan's surface is indicated in Figure 7.2 and applies to all three profiles [private communication, G. F. Lindal, 1982]. The last portion of each curve corresponds to the measurement noise level.

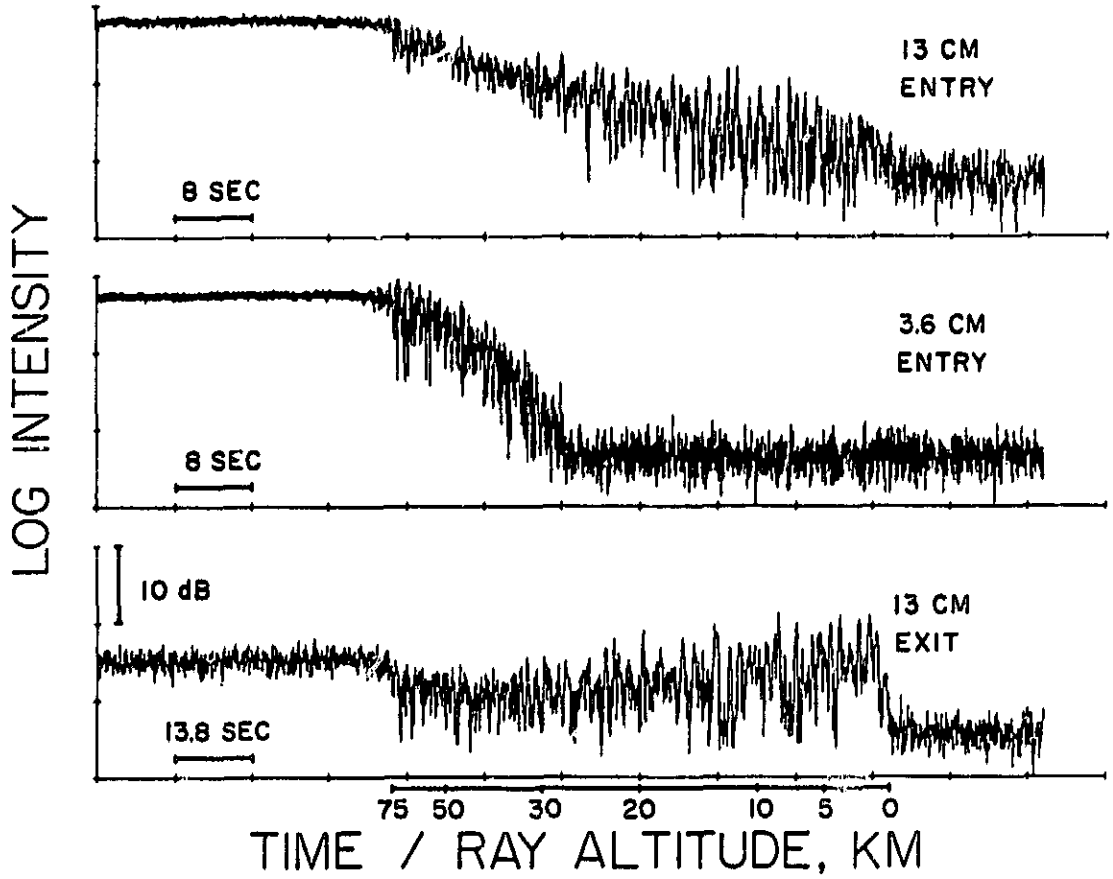

Figure 7.2 Profiles of intensity vs. time showing immersion for 3.6 and 13 cm, and emersion for 13 cm. The time scale for emersion has been reversed and compressed to account for geometrical differences between immersion and emersion. The combined effects of atmospheric refraction and antenna pointing determined the average shape of each curve. The 13-cm signal was received throughout immersion and emersion except when it was obscured by the surface; the 3.6-cm signal was lost in the noise because of the antenna orientation before the surface was reached. Titan's neutral atmosphere caused intensity fluctuations on time scales from about 0.1 to 1.0 s at both wavelengths, indicating the presence of variations in refractivity on length scales from a few hundred meters to a few kilometers at all altitudes within about 90 km of the surface.

During emersion, the antenna offset closely coincided with the angle of refraction by Titan's lower atmosphere. In this case, the signal extinction by the surface is clearly evident. The cut-off by the surface during immersion is unambiguous at a lower sampling rate which increases the signal-to-noise ratio [Lindal et al., 1983].

Small fluctuations in intensity appear in the first segment of each of the curves in Figure 7.2. These rapid variations result from thermal noise, and are representative of the measurement uncertainties in the upper atmosphere. Titan's neutral atmosphere caused intensity fluctuations which exceed the noise on time scales from about 0.1 to 1.0 s at both wavelengths. As discussed in detail below, this indicates the presence of variations in refractivity on length scales from a few hundred meters to a few kilometers at all altitudes within about 90 km of the surface. The strongest scintillations were observed with the lowest point on the radio path between about 5 and 25 km above the surface. Weaker intensity scintillations occurred with ray periapsis between the surface and 5 km, and between 25 and 90 km. Note that the scintillations show similar variation with altitude for immersion and emersion -- evidence that the atmospheric structures that cause these effects are not a localized phenomenon, as the observations were on opposite sides of Titan.

The intensity data were reduced through a two step procedure (Section 3.3). First, the technique of spectral analysis was applied to the weak intensity fluctuations caused by scattering from the upper atmosphere. Second, the fractional variance of intensity, σ_1^2 (see equation 3.4), was calculated for data obtained throughout the occultation. These results appear in the next section. Analysis of

C-2

phase fluctuations was restricted by the signal-to-noise ratio of the data and the limitations of the weak-scattering theory.

In order to interpret the intensity spectra, theoretical spectra, w_i, were calculated from equation A41 in Appendix A (as discussed in Section A.7, $w_i = 4w_\chi$ for weak scattering). It is important to note that the parameters ϕ_y and ϕ_z (see Appendix D) in this equation affect the shape of w_i [Haugstad, 1979], and vary with time during the occultation. Their values were determined using the formulas in Appendix D and parameters supplied by G. F. Lindal [private communication, 1982]. For all data considered here, $\phi_y \approx 1$ so that limb curvature had a negligible effect. However, ϕ_z varied from 1.0 before immersion to less than 0.1 with ray periapsis near the surface, and the steady variation of ϕ_z during the time interval of one spectrum had the effect of smoothing the measurements over a fractional range in frequency of about ±10%. To account for this frequency smearing, four theoretical spectra were calculated from equation A41 using four slightly different values of ϕ_z. Then, these spectra were averaged to produce a smoothed theory, $\bar{w}_i$, for comparison with the measurements. Typical values of parameters used in these computations were $v_y = 0.1$ km s^{-1}, $v_z = 7.98$ km s^{-1}, $\phi_y = 1.01$, $\phi_z = 0.29$, and $D = 9150$ km (see Appendix D for definitions); these values apply for scattering from Titan's atmosphere near 44 km during immersion.

Comparisons of measured spectra with the smoothed theory, $\bar{w}_i$, produced solutions for four parameters that characterize the scattering irregularities in the neutral atmosphere (see Section 3.4). In this case, the parameters are (Section 2.3.2): (1) the axial ratio, e/f; (2) the orientation, ψ; (3) the inverse power-law exponent, p, of the

spatial spectrum; and (4) the magnitude of the spatial variations in refractive index, n_t. The covariance matrix of the solution for the four parameters was computed by propagation of errors (Section 3.4) using the theoretical expression for $\overline{w}_i$ as a model for the process. The parameter measurements and the uncertainties are dicussed in the next section.

7.3 Results

Intensity spectra at 3.6 and 13 cm appear in Figure 7.3. Figure 7.4 shows the altitude interval of these measurements, which correspond to weak scattering ($\sigma_i^2 = 0.25$ at 3.6 cm and $\sigma_i^2 = 0.076$ at 13 cm; cf. Appendix B). The noise levels were determined from observations before immersion (see Section 3.4) with a correction for the decrease in average signal intensity. As this noise level was subtracted before fitting, large variations appear in the high frequency part of each measured spectrum. The best fit theoretical spectra are given as the smooth curves in Figure 7.3. When compared to the noise level, the fluctuations in 13-cm intensity from above 25 km during emersion were too small for useful spectral analysis.

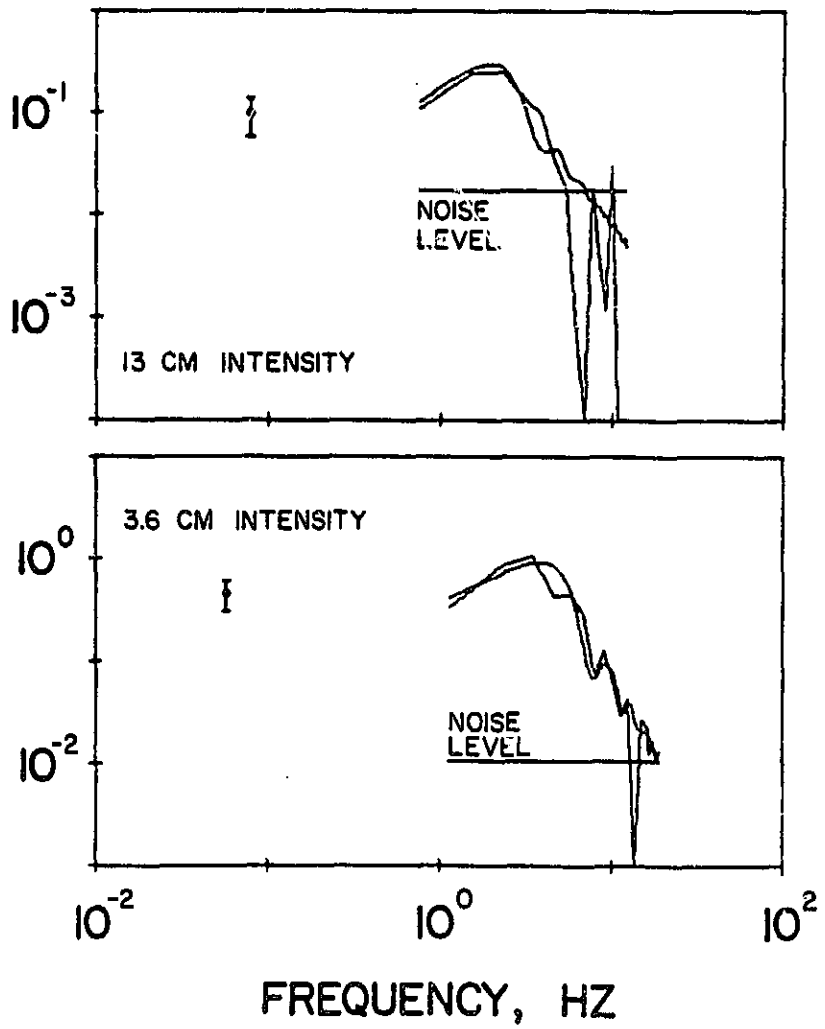

Figure 7.3 Weak-scattering intensity spectra at 13 cm (upper panel) and 3.6 cm (lower panel) during immersion from the smoothing interval centered at 44 km in Figure 7.4. Theoretical spectra (smooth curves superimposed) were fitted in a least-squares sense to measured spectra over the frequency range where the intensity fluctuations exceed the noise level by at least 3 dB. Note that the noise level was subtracted before fitting, resulting in large variations in the high frequency portion of both spectra.

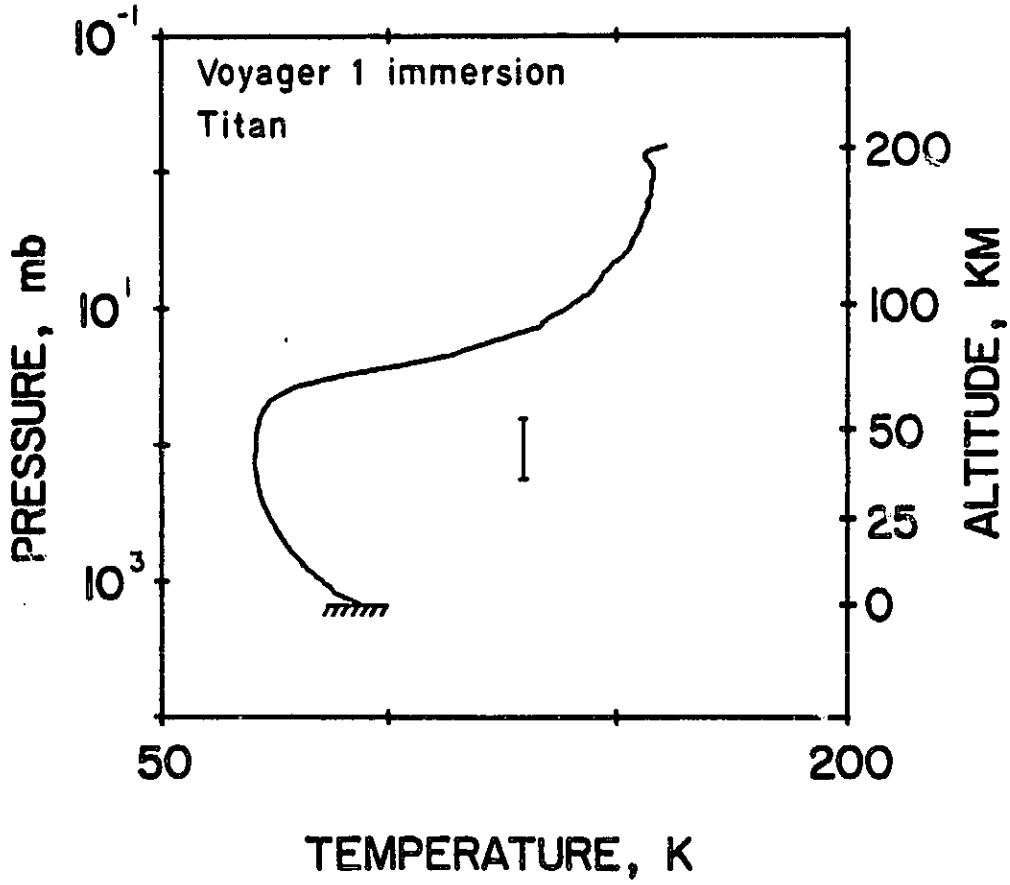

Figure 7.4 Temperature-pressure profile with altitude scale for Titan's atmosphere at immersion [Lindal et al., 1983]. Vertical bar indicates the smoothing interval for computing the intensity spectra in Figure 7.3.

Table 7.1 Characteristics of irreglarities in Titan's upper atmosphere at immersion.

Height, km	λ, cm	ψ, degrees	p	Axial ratio	n_t/n_o
44	3.6	0. ± 10.	3.7 ± 0.3	4 ± 2	$(8 \pm 3) \cdot 10^{-4}$
44	13.	10. ± 20.	3.1 ± 0.4	6 ± 4	$(9 \pm 4) \cdot 10^{-4}$

The solutions for atmospheric parameters derived from the intensity spectra are listed in Table 7.1. Each measurement should be interpreted as a spatial average over the smoothing interval in Figure 7.4. The uncertainties, which correspond to 1-σ, result from noise limitations and the steady variation of ϕ_z over the time period of the measurements, which tends to suppress the distinguishing features in the spectra. Recall that e/f and ψ characterize the shape and orientation, respectively, of the atmospheric irregularities (see Section 2.3.2 and Figure 2.3). Applying this interpretation to the present case ($e/f \sim 4$, $\psi \sim 0$), both horizontal and vertical variations in refractivity probably were present in Titan's upper atmosphere. The structures were not isotropic, but instead had a tendency toward horizontal stratification. In addition, the normalized variations in refractive index, n_t/n_o, were of order 10^{-3}.

The transverse raypath velocity at 44 km altitude is given by $|\vec{v}_*| \approx 2.3$ km s^{-1} (see Appendix D and the parameter values given above). This value greatly exceeds both the phase velocity of atmospheric waves and the bulk velocity of fluid motion which are likely to be encountered in Titan's atmosphere (see below). Hence, the intensity fluctuations in Figure 7.3 result primarily from motion of the radio path across a fixed field of refractive irregularities. Using this interpretation, the scale sizes in the atmosphere which contributed to the spectral range 1 to 10 Hz lie between about 0.2 and 2 km.

The variance of normalized intensity, σ_i^2, was measured over time intervals of 1.3 s for immersion at 13 cm, 0.87 s for immersion at 3.6 cm, and 2.6 s for emersion at 13 cm; the three curves appear in Figure 7.5. In general, larger values of σ_i^2 were observed at lower

altitudes. Hence, each value of σ_i^2 was assigned the minimum periapsis altitude in the corresponding measurement interval. As mentioned previously, ϕ_z and $\vec{v}_*$ varied smoothly as a function of periapsis altitude during the occultation. Each parameter was reduced to about 10% of its free-space value when the raypath reached Titan's surface. Consequently, the resolution of the measurements improved from about 8 km at 100 km altitude to about 0.8 km at the surface during immersion, with roughly half the resolution at the same altitudes during emersion. The standard deviation of σ_i^2 was calculated by established methods [Jenkins and Watts, 1968], and appears at two altitudes in each curve. The smooth curves show the noise levels, which vary as $\langle I(t) \rangle^{-1}$. At altitudes below about 90 km, σ_i^2 clearly exceeded the noise -- the observed scintillations resulted primarily from scattering in Titan's atmosphere (cf. Figure 7.2).

The measurements in Figure 7.5 quantitatively illustrate the general features mentioned previously in describing Figure 7.2. During immersion, spatial irregularities in Titan's atmosphere caused weak intensity scintillations when ray periapsis was between the surface and about 5 km, or between 25 and 75 km, where σ_i^2 was nearly constant. Strong scintillations occurred with ray periapsis between 5 and 25 km. (The basis for distinguishing between weak and strong scintillation is given in Appendix B.) At both wavelengths, σ_i^2 increased by more than an order of magnitude when ray periapsis descended from 90 to 70 km. During emersion, σ_i^2 showed the same general characteristics as for immersion, although the increased noise level restricts interpretation. The theoretical curves, shown superimposed, are explained in the next section.

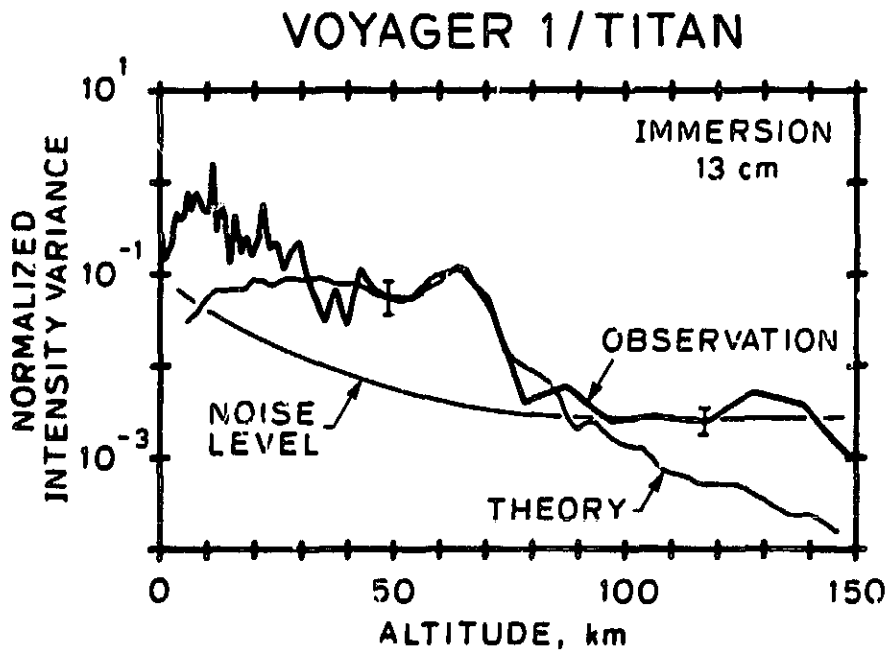

Figure 7.5a Normalized intensity variance at 13 cm (heavy line) as a function of periapsis altitude during Voyager 1 immersion at Titan. The noise level varies as $\langle I(t)\rangle^{-1}$ and is indicated by the smooth curve. Altitude resolution improved from about 8 km at 100 km altitude to about 0.8 km at the surface. Uncertainties are shown at two altitudes. The theory (superimposed light line) is based on a model for the propagation of internal gravity waves through the vertical stratification in Titan's atmosphere.

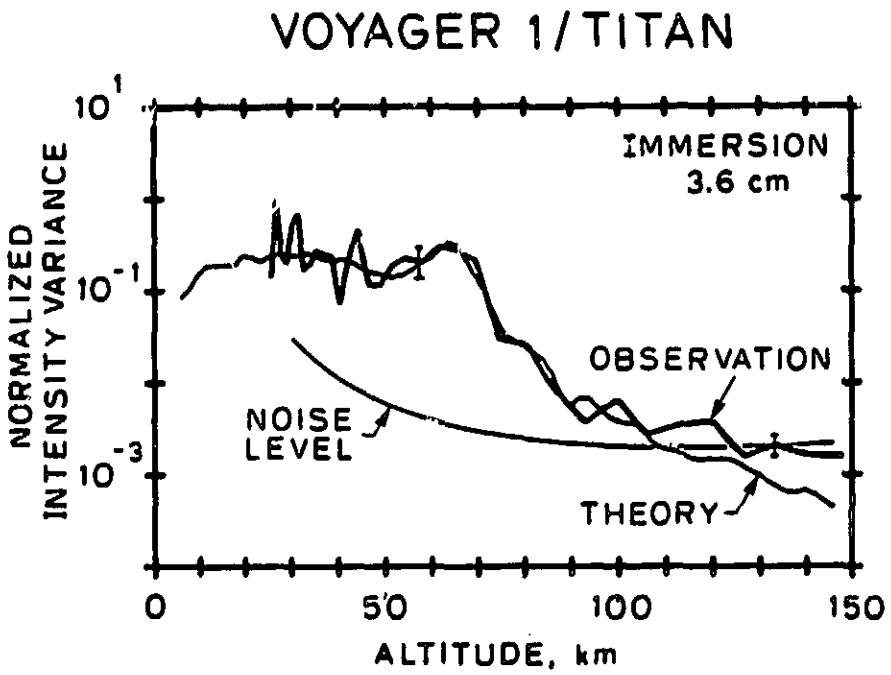

Figure 7.5b Normalized intensity variance at 3.6 cm during Voyager 1 immersion at Titan. See Figure 7.5a for additional comments.

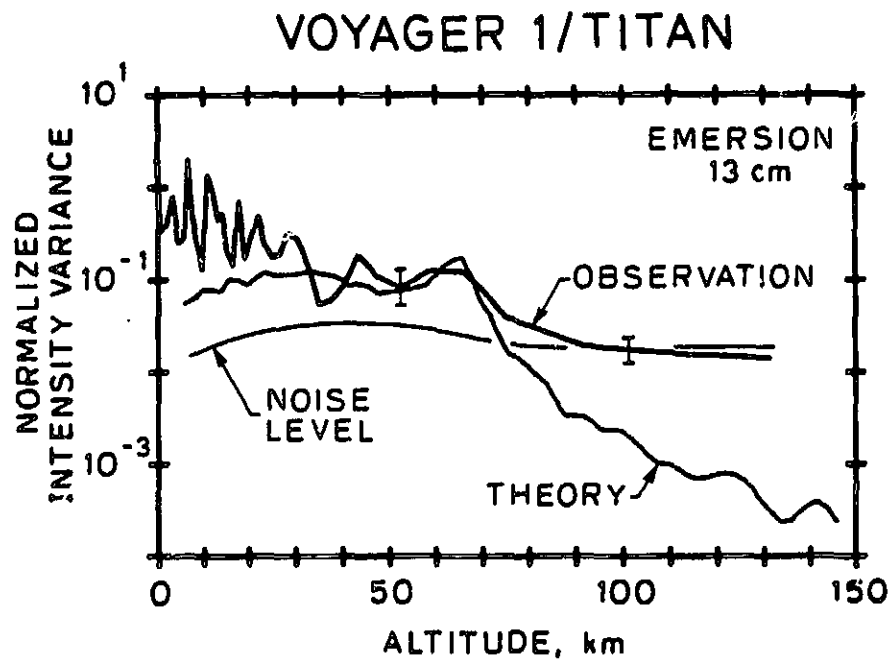

Figure 7.5c Normalized intensity variance at 13 cm during Voyager 1 emersion at Titan. See Figure 7.5a for additional comments.

7.4 Discussion

Upper Atmosphere (above 25 km). The parameters in Table 7.1 provide evidence for horizontal variations in refractivity, and hence dynamics, near 44 km in Titan's atmosphere. Above 25 km, the altitude profile of σ_1^2 (Figure 7.5) closely agrees with the predictions of a simple theory based on the chracteristics of freely propagating atmospheric gravity waves [Hines, 1960; Gossard and Hooke, 1975], as will be shown below. On the basis of these observations, the scintillations that occurred during occultation by the upper atmosphere are primarily the result of scattering from the density disturbances associated with gravity waves. (Note that the high vertical stability of the atmosphere above 25 km excludes convective turbulence as an explanation for intensity scintillations.)

To understand the altitude variation of σ_1^2, consider a parcel of gas displaced adiabatically in the vertical direction. During a gradual displacement, the fractional difference in density between the displaced parcel and its new surroundings is given by [cf. Gossard and Hooke, 1975, p. 71-75]:

$$\frac{\delta\rho}{\rho} = \frac{1}{\theta}\frac{\partial\theta}{\partial z}\delta z \qquad (7.1)$$

where $\delta\rho$ is the density difference, ρ is the density of the undisturbed atmosphere, θ is the potential temperature, and the vertical displacement, δz, is assumed to be small compared to the atmosphere's scale height.

The derivative of θ can be expressed as [cf. Turner, 1973, p.5]:

$$\frac{1}{\theta}\frac{\partial\theta}{\partial z} = \frac{1}{T}\left[\frac{\partial T}{\partial z} + \frac{g}{c_p}\right] \equiv \Pi \qquad (7.2)$$

where T is the temperature of the undisturbed atmosphere, g is the gravitational acceleration, and c_p is the specific heat per unit mass at constant pressure. The density variations, δρ, result from the combined effects of adiabatic expansion and the vertical stratification of the undisturbed atmosphere.

To approximate the behavior of atmospheric gravity waves, it is assumed here that δz increases exponentially with altitude in proportion to $\rho^{-1/2}$ so as to maintain a constant vertical energy flux [Turner, 1973, p. 10-11, 22-23]. As discussed in Appendix A (see Section A.7 and the paragraph following equation A40), σ_i^2 is proportional to both the variance of refractive index, $\langle n_t^2 \rangle$, and the variance of fluctuations in atmospheric density. By combining equations 7.1 and 7.2 the theoretical intensity variance in this model varies with altitude as

$$\sigma_i^2 \propto \rho\left\{\frac{1}{T}\left[\frac{\partial T}{\partial z} + \frac{g}{c_p}\right]\right\}^2 \qquad (7.3)$$

The constant of proportionality depends on experimental geometry, radio wavelength, and the vertical energy flux and spatial characteristics of the wave.

The theoretical σ_i^2 was calculated from equation 7.3 using values of ρ, T, and ∂T/∂z measured during the radio occultation [Lindal et al., 1983], values of g(z) determined from Titan's mass [Tyler et al., 1981a], and a value of c_p appropriate for N_2. The theoretical curves

are superimposed in Figure 7.5. The constant of proportionality in equation 7.3, which amounts to an additive offset on the logarithmic plot, was adjusted to obtain a good fit. The ratio of these constants at 3.6 and 13 cm during immersion, about 3, is consistent with scattering from a power-law distribution of irregularities with exponent $p \approx 4.3$ (see Section A.7 and the paragraph following equation A40). This value is within 3σ of the estimates in Table 7.1.

Above 25 km during immersion, the altitude variation of the observed scintillations is entirely consistent with a hypothesis of freely propagating gravity waves; interpretation for emersion is somewhat restricted by noise, but also appears to be consistent with this hypothesis. Note the detailed agreement between the theory and 3.6-cm measurements (Figure 7.5b): both exhibit a nearly constant level of scintillation between 25 and 60 km, a local maximum at 65 km, and a rapid decrease above 70 km that includes several changes in slope. A region of high vertical stability, where $\partial T/\partial z$ is large (Figure 7.4), leads to the enhancement of σ_i^2 near 65 km, while the abrupt decrease above 70 km results from the atmosphere's average vertical structure, not from wave attenuation or reflection.

The model described by equations 7.1 to 7.3, though not rigorous, has the advantage of requiring relatively few assumptions while still incorporating the principal features of gravity-wave propagation. In this regard, the level of analysis attempted here is consistent with the limitations of the available data. To avoid unnecessary complications in the discussion below, it is assumed that a single coherent gravity wave caused the scintillations. In reality, the signal fluctuations are probably the result of scattering from a superposition of gravity waves,

since the spectra in Figure 7.3 reveal a continuous distribution of energy over a range of length scales. Nevertheless, this assumption should be acceptable for order-of-magnitude calculations.

The physical characteristics of the gravity waves can be inferred from the parameters listed in Table 7.1. Near 44 km, $\Pi = 2 \cdot 10^{-5}$ m^{-1}, $\rho = 0.5$ Kg m^{-3} [Lindal et al., 1983], and the fractional variations in density associated with the wave must satisfy $\delta\rho/\rho = n_t/n_o = 10^{-3}$ (for the relationship between refractivity and density, see Section 2.2). The horizontal and vertical wavelengths are roughly 4 and 1 km, respectively, which correspond to the observed size and axial ratio of the irregularities. Then, using standard formulas for the linearized relationships among field variables for gravity waves [Gossard and Hooke, 1975, p. 75], the horizontal and vertical fluid velocities associated with the wave are $u_h \approx 0.2$ m s^{-1} and $u_v \approx 0.05$ m s^{-1}, respectively. Similarly, the phase velocity is 0.2 m s^{-1}. The vertical displacement caused by the wave, which follows from equations 7.1 and 7.2, is about 50 m at 44 km. In the Boussinesq approximation used implicity here, the fractional variations in temperature obey $\delta T/T \approx -\delta\rho/\rho$ [Spiegel and Veronis, 1960]; substitution yields wave-associated temperature fluctuations of about 0.07 K at 44 km.

Below 25 km, the scintillations at 13 cm during both immersion and emersion exceed the predictions of the gravity-wave theory. This observation and other considerations (see below) suggest that tropospheric processes below 25 km excite gravity waves which transport energy and momentum upward through the atmosphere. The vertical flux of energy due to gravity waves is given by $\overline{\delta p \cdot u_v}$, where δp is the pressure field associated with the wave and the overbar denotes a wave-cycle

average [Lindzen and Holton, 1968]. Using the approximations above, the upward flux of energy at 44 km is roughly $2 \cdot 10^{-3}$ W m^{-2} (2 erg cm^{-2} s^{-1}). The vertical flux of horizontal momentum from gravity waves is given by $\overline{\rho u_h u_v}$ [Gossard and Hooke, 1975, p.108]. The net flux depends on a summation over the momentum components of each wave in the superposition, which is not possible based on the present observations. However, an upper limit of $3 \cdot 10^{-3}$ N m^{-2} ($3 \cdot 10^{-2}$ dyne cm^{-2}) can be placed on the net upward flux of horizontal momentum by assuming that the contributions from the waves add constructively, which amounts to the assumption of an anisotropic gravity-wave source.

Viscosity and thermal conductivity cause the dissipation of small scale waves, and impose a lower limit on the permitted gravity-wave scale size. This minimum scale size increases at higher altitudes because of the increase in kinematic viscosity that accompanies a decrease in atmospheric density [Hines, 1960]. The effect of dissipation in Titan's atmosphere was evaluated using approximate formulas derived by Gossard and Hooke [1975, p. 218], the temperature-pressure profile in Figure 7.4, and measurements of the viscosity of N_2 appropriate to Titan's atmosphere [Vargaftik, 1975, p. 458]. According to these calculations, gravity waves of length scale a few hundred meters to a few kilometers, which correspond to the size of the observed irregularities, can propagate essentially unattenuated to at least 150 km in Titan's atmosphere; this result provides a basis for discussing the importance of the gravity-wave transport of energy and momentum.

This gravity-wave energy flux is believed to be insignificant relative to the rate at which solar energy is absorbed in the

stratosphere or at the surface [private communication, R. E. Samuelson, 1982]. Hence, gravity waves will not affect the atmosphere's thermal structure below 150 km; only at considerably higher altitudes would this energy flux become significant. In contrast, the absorption of momentum above 150 km at a rate of 10^{-3} N m^{-2} would accelerate the atmosphere by about 7 m s^{-1} per Titan day, which may be significant in sustaining the cyclostrophic zonal winds described by Hanel et al. [1981] and Flasar et al. [1981].

The net transport of momentum does not require anisotropic gravity-wave sources, and can occur under quite general source conditions when gravity waves propagate through a region of vertical wind shear. Briefly, waves propagating upward through a region of sufficient wind shear are either absorbed or reflected depending on whether their components of horizontal momentum are generally parallel or anti-parallel, respectively, to the mean flow. The theory of reflection and "critical layer" absorption has been discussed at length [Gossard and Hooke, 1975, p. 170; Bretherton, 1969a, b; Turner, 1973, p. 24-29 and 37-39]; this same type of interaction, where gravity waves transport horizontal momentum from the troposphere, where they are generated, to the stratosphere, where the momentum is absorbed by the mean flow at a critical layer, has been proposed by Lindzen and Holton [1968] to explain features of the zonal flow in the Earth's tropical atmosphere [also see Holton and Lindzen, 1972; Wallace, 1973; Cadet and Tietelbaum, 1979]. Until more detailed observations are available, one can only speculate that gravity waves may supply momentum to Titan's zonal circulation through this type of interaction. It should be noted that some momentum transport process is required to maintain the excess angular momentum in Titan's atmosphere [Flasar et al., 1981].

The preceding discussion presented evidence in support of a gravity-wave interpretation for the refractive irreglarities in Titan's atmosphere above 25 km. Although other interpretations are possible, each suffers from inconsistencies with the observations. For completeness, and to provide indirect support for the gravity-wave hypothesis, several alternative explanations and their limitations are summarized below.

Minor constituents in Titan's stratosphere include C_2H_6, C_2H_2, C_3H_8, C_3H_4, and HCN [Maguire et al., 1981; Kunde et al., 1981]. Figure 2 of Maguire et al. [1981] indicates that the condensation level of each of these gases lies between about 55 and 85 km. As the upper boundary of condensation is expected to be abrupt, the condensation products could introduce layers in refractivity that contribute to the scattering observed in Titan's stratosphere. Alternatively, thin stable layers are observed commonly in the earth's troposphere and stratosphere under cloud-free conditions [Harper and Gordon, 1980; Gage and Balsley, 1980; Röttger, 1980], and could also contribute to scattering in Titan's stratosphere. However, in either case, stable stratification cannot account for the inferred horizontal variations in refractivity. Furthermore, the agreement between the gravity-wave theory and the observations in Figure 7.5 suggests that these scattering mechanisms are not important in Titan's upper atmosphere.

Thin turbulent layers in clear air have been observed in the earth's lower stratosphere [R. K. Crane, 1980]. These turbulent regions develop when an atmospheric layer becomes unstable with respect to vertical displacement because of excessive wind shear. A related measure of atmospheric stability is given by the gradient Richardson

number, $Ri \equiv g\Pi/(\partial U/\partial z)^2$ [Wallace, 1973]. Here, the numerator is the square of the Vaisala-Brunt frequency, the denominator is the square of the wind shear, and $Ri > 0.25$ is generally regarded as the condition for stability [Turner, 1973, p. 100]. In the interval between 25 and 75 km, $(g\Pi)^{1/2} \gtrsim 4 \cdot 10^{-3}$ s^{-1}, requiring $\partial U/\partial z \gtrsim 8$ m s^{-1} km^{-1} for instability. A wind shear of this size has not been confirmed by any observations -- turbulent layers are not expected to be present in Titan's atmosphere above 25 km.

A hypothesis that the scattered signal originates from acoustic waves also fails to explain the observations. An acoustic-wave energy flux of about 1 W m^{-2} would be required to account for the parameters in Table 7.1 [for the appropriate theory, see Gossard and Hooke, 1975]. However, there is no plausible energy source for waves of this magnitude. For example, a source in the boundary layer near the surface would necessitate remarkably efficient conversion of the incident solar flux of about 3 W m^{-2} [Samuelson, 1983], and would deplete the insolation needed to maintain radiative equilibrium at the temperatures in the lower atmosphere [cf. Samuelson, 1983; Lindal et al., 1983; Eshleman et al., 1983]. Furthermore, Figure 7.6 shows two theoretical profiles of $\langle n_t^2 \rangle$, a quantity that is proportional to σ_i^2 as discussed above. One curve is appropriate to internal gravity waves, or buoyancy waves (see Section 1.3), and also appeared in Figure 7.5; the other curve corresponds to freely-propagating acoustic waves. The latter was calculated using formulas analagous to those in equations 7.1-7.3 [Gossard and Hooke, 1975], and the measured stratification of Titan's atmosphere at Voyager 1 immersion (Figure 7.4). The buoyancy-wave profile agrees with the measurements above 25 km in Figure 7.5, but the acoustic-wave profile diverges significantly.

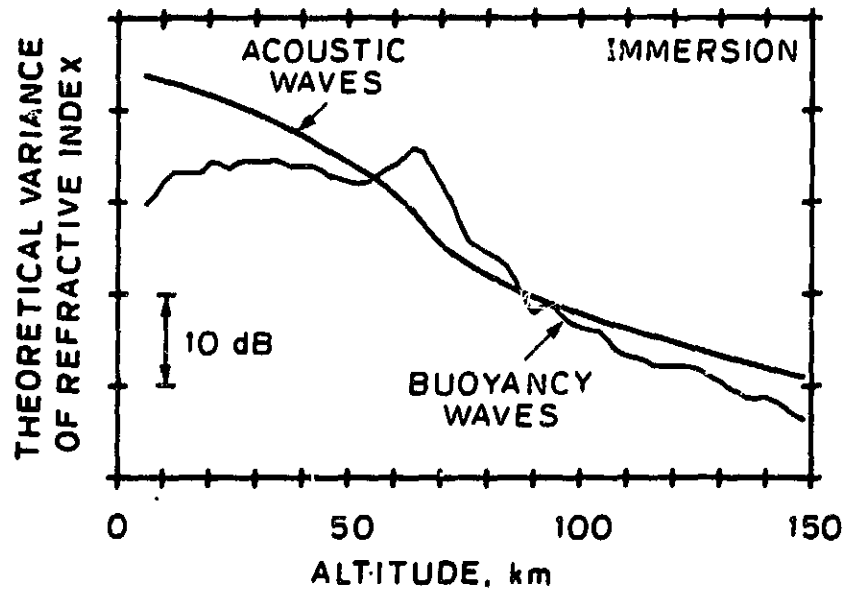

Figure 7.6 Two theoretical profiles for the variance of refractive index. Each would result from a different type of atmospheric wave propagating through the vertical stratification in Titan's atmosphere at Voyager 1 immersion. One curve is appropriate to internal gravity waves, or buoyancy waves, and also appeared in Figures 7.5a and 7.5b. The second curve corresponds to acoustic waves. The two curves have been scaled by constants to facilitate comparison.

Lower Atmosphere (0-25 km). The temperature follows the dry adiabatic lapse rate for N_2 in the lowest few kilometers of the atmosphere [Lindal et al., 1983]. Consequently, the weak scintillations from this region during immersion (see Figures 7.2 and 7.5a) might be the result of propagation through a cloud-free convective boundary layer. Detailed analysis of the signals scattered from this layer is restricted by the short time duration and limited signal-to-noise ratio

of the data. In addition, the strong refractivity variations between 5 and 25 km altitude tend to obscure the irregularities between the surface and 5 km when observed through occultation techniques. More work is needed on this problem. It is interesting to note that boundary layer turbulence and penetrative convection can excite gravity waves [Stull, 1976; Einaudi et al., 1978; Nagpal, 1979; Harper and Gordon, 1980] that would propagate into the stratosphere.

Between 5 and 25 km, the temperature lapse rate is subadiabatic and apparently stable [Lindal et al., 1983; Eshleman et al., 1983], and the 13-cm scintillations exceeded the predictions of the gravity-wave model (Figure 7.5). A comparison with the earth's atmosphere [Stull, 1976] suggests that penetrative convection is unlikely to extend more than a few kilometers into the stable region above the turbulent boundary layer. Consequently, the strong scattering in the middle troposphere perhaps was associated with propagation through stratified layers rather than dynamics. Lindal et al. [1983] and Eshleman et al. [1983] found no direct evidence for CH_4 condensation in the radio occultation observations, and favor models in which the CH_4 concentration is at most a few percent. In this case, layers in Titan's troposphere similar to those observed in the earth's troposphere and stratosphere under clear air conditions [Green and Gage, 1980] could cause the strong radio scintillations in the absense of any clouds. However, Samuelson et al. [1981] proposed that CH_4 clouds may provide the dominant opacity in Titan's upper troposphere, although Hunt et al. [1983] currently dispute this claim. On the basis of terrestrial cloud models [Mason, 1971], the refractivity variations resulting from layered clouds could explain some of the strong scintillations in this region provided that

sufficient material has condensed. At present, we cannot distinguish between these two interpretations.

Analysis of the strong intensity scintillations (see Figures 7.2 and 7.5) may provide additional information on the refractivity structures in Titan's troposphere. In particular, it may be possible to infer the morphology of the irregularities, as was the case in Titan's stratosphere, and thereby distinguish stable stratification from dynamic processes. Any information concerning the variations in refractivity between 5 and 25 km altitude would lead to a better understanding of the source for stratospheric gravity waves, and the lowest few kilometers of the atmosphere as well.

CHAPTER 8

SUMMARY OF RESULTS AND SUGGESTIONS FOR FUTURE WORK

8.1 Summary of Results

A new procedure has been developed for systematically analyzing the amplitude and phase scintillations observed during radio occultations by planetary atmospheres (Chapter 3). First, conventional methods of spectral analysis are applied in order to reduce the data and to model the statistics of the measurements. Then, the resultant amplitude and phase spectra are interpreted through objective comparisons with the predictions of the well-developed weak-scattering theory. This technique yields least-squares solutions for parameters that characterize the underlying atmospheric scattering structures. The covariance matrix of the solutions is calculated by propagation of errors, thereby providing the measurement uncertainties. This procedure was applied to data obtained during the dual-wavelength (3.6 and 13 cm) radio occultations of Voyager by Jupiter, Saturn, and Titan.

For Jupiter and Saturn, only data pertaining to the upper ionospheres were considered. For the theoretical calculations, the occulting ionosphere was modeled as a thin screen containing a power-law spectrum of anisotropic scattering structures. Comparisons between measured spectra and the theory produced solutions for four parameters in the model for the ionospheric irregularities: (1) the axial ratio, (2) the angular orientation, (3) the power-law exponent of the spatial spectrum, and (4) the magnitude of the spatial variations in electron density. Scattering was observed from irregularities of approximate size 2 to 140 km at Jupiter and 2 to 60 km at Saturn; in both cases,

the lower and upper limits result from noise limitations and the method of analysis, respectively, and do not represent either inner or outer scales. Within this size interval, the three-dimensional spatial spectrum obeys an inverse power law with exponent varying from 3.0 to 3.7; moreover, and the fractional variations in electron density range from 1 to 20%. All irregularities appear to be anisotropic; the axial ratios, which vary with altitude and latitude, are as small as 2:1 at low altitudes in the equatorial ionosphere, and as large as 12:1 at high latitudes. Magnetic field orientations in the ionospheres of Jupiter and Saturn were inferred from the direction of alignment of the anisotropic irregularities. The occultation measurements conflict with the predictions of current Jovian magnetic field models, but generally corroborate models of Saturn's field, and may prove useful in deriving improved field representations. These results were discussed at length in Chapters 4, 5, and 6.

During the occultation of Voyager 1 by Titan, intensity and frequency fluctuations occurred on time scales from about 0.1 to 1.0 s at both wavelengths whenever the radio path passed within 90 km of the surface. This observation indicates the presence of variations in atmospheric refractivity on length scales from a few hundred meters to a few kilometers. As the intensity fluctuations showed similar variations with altitude during immersion and emersion, the small-scale atmospheric structure does not appear to be a localized phenomenon. The theoretical intensity spectra show best agreement with the measurements when horizontal variations in refractivity are included in the models for the scattering irregularities -- evidence for a dynamic atmosphere. Above 25 km, the altitude profile of intensity scintillation closely agrees

with the predictions of a theoretical model in which internal gravity waves propagate with no attenuation through the vertical stratification in Titan's atmosphere. These results substantiate the hypothesis that gravity waves underlie the variations of refractivity in Titan's upper atmosphere. A cloud-free convective region in the boundary layer near the surface could act as a source for the waves. The net upward flux of energy and an upper bound on the net upward flux of horizontal momentum due to gravity waves are approximately $2 \cdot 10^{-3}$ W m^{-2} (2 erg cm^{-2} s^{-1}) and $3 \cdot 10^{-3}$ N m^{-2} ($3 \cdot 10^{-2}$ dyne cm^{-2}), respectively. Although this energy flux is not significant in determining the thermal structure of the atmosphere below 150 km, the vertical transport of momentum by gravity waves could be important in maintaining the zonal stratospheric circulation. These results were described in detail in Chapter 7.

8.2 Suggestions for Future Work

8.2.1 Development of a New Technique for Analyzing Strong Scintillations.

The theory derived in Appendix A is valid only for the case of weak scattering. However, periods of strong intensity scintillation were observed during the Voyager radio occultations by Jupiter, Saturn, and Titan (for example, see Chapter 7); a more general theory is required in order to interpret these data. In this regard, the development of new methods of analysis could improve the occultation technique by extending it into the strong-scattering signal regime.

In a recent advance, a new theory was derived to predict the temporal spectrum of strong intensity fluctuations during an occultation by an atmosphere with a finite scale height [Haugstad, 1982]. All previous derivations for the case of strong scattering neglected the

effect of differential refraction (or Fresnel zone distortion) associated with occultation measurements [cf. Rumsey, 1975], and therefore were inappropriate for interpreting the strong intensity scintillations mentioned above. A difficult numerical integration is required to implement the new formula; after this has been accomplished, it will be possible for the first time to analyze strong intensity scintillations during planetary occultations. The theoretical spectra can be compared to the measurements by following the least-squares procedure described in Section 3.4. At present, one area of uncertainty in the potential of this new technique involves the sensitivity of the strong-scattering spectra to the underlying dynamic structure in the occulting atmosphere.

8.2.2 Further Analysis of Voyager Radio Occultation Data. Our knowledge of the neutral atmospheres of Jupiter and Saturn might benefit from analysis of the signal fluctuations observed during the Voyager radio occultations. Weak scintillations can be analyzed by following the procedures which were applied in Chapter 7 to interpret data from the Voyager 1 occultation by Titan. Strong intensity scintillations can be attacked by using the new technique described above. In this way, the structure and dynamics of these atmospheres can be investigated on length scales near Fresnel-zone size (see Tables 4.1 and 5.1) and at pressures from about 1 mbar to more than 1 bar.

Strong intensity scintillations were observed in connection with propagation through Titan's lower atmosphere (5-25 km altitude; see Figures 7.2 and 7.5). Present uncertainties regarding the nature of the refractive irregularities in this region might be resolved through application of the technique described above. By comparing calculated

theoretical spectra with the measurements, spatial characteristics of the atmospheric structures, such as the axial ratio and size distribution, might be inferred. (See Chapters 4, 5, and 7 for results derived from observations of weak scattering.) This characterization could lead to a better understanding of the structure and dynamics of Titan's troposphere, and might allow an identification of the source of the stratospheric gravity waves.

While internal gravity waves in the earth's atmosphere have been studied extensively, the role of gravity waves in other planetary atmospheres remains uncertain. In fact, the Voyager occultation measurements at Titan constitute the only detailed observations of progressive gravity waves in the atmosphere of another planet. In previous stellar and radio occultations, the unambiguous identification of gravity waves as scattering sources has not been possible. For example, Woo et al. [1980a] initially speculated that scintillations observed during the radio occultations of Pioneer by Venus were the result of trapped gravity waves in a vertically stable region of the atmosphere. However, Woo et al. [1982] subsequently revised this interpretation and attributed the scattering to turbulent layers generated by wind-shear instability. It also has been suggested that gravity waves cause the intensity fluctuations observed during stellar occultations by the upper atmospheres of Jupiter [French and Gierasch, 1974] and Uranus [French et al., 1983]. Although the discovery of internal gravity waves at Titan lends credibility to this interpretation, the hypothesis remains speculative, since the underlying cause of intensity fluctuations in stellar occultations is at present the subject of controversy (for example, see the review by Elliot [1979]).

A study of atmospheric dynamics at Jupiter, Saturn, and Titan, as outlined above, could promote a more general awareness of the role of gravity-wave phenomena in planetary atmospheres. Progress in understanding the dynamics of these atmospheres could provide a basis for comparisons with the earth and with other planets as studied by occultation methods, thereby contributing to atmospheric studies at several planets.

8.2.3 Magnetic Field Studies at Jupiter and Saturn. In a spherical harmonic magnetic field representation, the quadrupole and octupole terms in the expansion are relatively more important in the ionosphere than at the remote position of spacecraft magnetometer measurements (see Section 6.5). Consequently, the field orientations inferred from radio occultations could provide useful constraints on the higher-order coefficients in field models. For this reason, our knowledge of the internal magnetic fields of Jupiter and Saturn could be improved through the development of methods for deriving field models from the combined magnetometer and radio occultation measurements.

Two fundamental areas of research might benefit from future measurements pertaining to the magnetic fields of Jupiter and Saturn. First, improved spherical harmonic field representations or evidence for secular variation could provide constraints for models of the Jovian and Saturnian interiors and dynamos [Hide and Malin, 1979; Stevenson, 1980]. Second, efforts toward obtaining a more detailed field model near these planets might lead to a better understanding of the source of low-frequency radio emissions from both Jupiter [Warwick et al., 1979a, b; Boischot et al., 1981] and Saturn [Kaiser et al., 1980, 1981; Warwick et al., 1981, 1982], and an explanation for the modulation of the radiation at the planets' rotation rates.

Observations of Faraday rotation in future radio occultations could provide the strength of the field component along the ray path [Eshleman, 1973]. A spacecraft orbiting Jupiter or Saturn and equipped for radio occultation measurements of both scintillations and Faraday rotation would be well suited for further study of the planetary magnetic field. When combined with the conventional magnetometer data, a sequence of radio occultation measurements at a range of latitudes and longitudes could produce a more accurate field model near the planet. These types of measurements are planned as part of a future investigation of the Jovian system using the Galileo ortiber [private communication, H. T. Howard, 1983].

APPENDIX A

DERIVATION OF THEORETICAL FORMULAS FOR WEAK SCATTERING

A.1 Introduction

The theory for propagation of electromagnetic waves through a weakly irregular refracting medium originated in the studies of radio star and satellite scintillations caused by the earth's ionosphere [for example, see Booker et al., 1950; Hewish, 1951; Fejer, 1953; Bramley, 1954; and Ratcliffe, 1956]. The application of the weak-scattering theory to an occultation geometry has been discussed by Haugstad [1978b], Hubbard et al. [1978], and Woo et al. [1980b], among others. Although the results are not original, expressions for the theoretical covariance functions and scintillation spectra are derived here for completeness, and to provide a basis for the discussions in Appendix B (a limit for validity of the weak-scattering theory) and Appendix C (a physical interpretation of the weak-scattering theory).

In Sections A.2 and A.3, the theory is derived for scattering from a phase screen with a spatially homogeneous average refractive index. Section A.4 gives some convenient definitions for the transverse coordinates in the phase screen. In Sections A.5 and A.6, the theoretical formulas are modified to account for the effect of Fresnel zone distortion (see Appendix D). Finally, Section A.7 discusses the relationships among amplitude, log amplitude, and intensity fluctuations.

A.2 Covariance Functions: Homogeneous Background

A.2.1 Approximate Forumlas for the Scattered Field. At the magnetic field magnitudes in Jupiter's ionosphere inferred from spacecraft magnetometer measurements [Connerney, 1981], the electron gyrofrequency, f_e, is 10 to 20 MHz, while at the field strengths in Saturn's ionosphere [Connerney et al., 1982], $f_e \approx 1$ to 2 MHz. The observed ionospheric irregularities appear to be anisotropic and field aligned (Chapters 4 and 5), which suggests that the electron collision frequency $\nu_e \lesssim f_e$. In addition, the plasma frequencies, f_p, are less than 4 MHz and 1 MHz at the maximum electron densities measured in Jupiter's upper ionosphere [Eshleman et al., 1979b, c] and Saturn's upper ionosphere [Tyler et al., 1981a, 1982], respectively.

The radio frequencies used for the Voyager occultation experiments (2295 and 8415 MHz) greatly exceeded f_e and f_p at both Jupiter and Saturn. For this reason, the effect of the planetary magnetic field on the refractive index in the ionospheres was extremely small [cf. Jordan and Balmain, 1968, pp. 687-698]. Nevertheless, a linearly polarized microwave signal propagating through Jupiter's ionosphere would be expected to experience appreciable Faraday rotation. However, the observation of this phenomenon was not possible with the Voyager spacecraft, which transmitted signals in right-hand circular polarization.

In the remainder of this appendix, the phenomenon of Faraday rotation is neglected; the magnetic field then has no significant effect on direct propagation through the planetary ionospheres. (Note, however, that the magnetic field affects the morphology of the plasma irregularities, and thereby indirectly influences the scattered

signals.) The positions of the transmitter and receiver enter symmetrically into the expression for the scattered field (equation A1, below). Using this property, the roles of the spacecraft transmitter and earth-based receiver are interchanged in what follows, which simplifies the derivation and discussion without affecting the results. In particular, the electromagnetic wave impinging on the occulting planetary atmosphere can be treated as planar, since the distance from earth to the planet is greater by a factor of at least 700 than the distance from planet to spacecraft for the occultations considered here.

Figure A1 shows the idealized experimental geometry. A monochromatic plane wave of unit amplitude propagating in the x-direction illuminates the occulting atmosphere, modeled as a screen of thickness L with transverse coordinates y, z. The spacecraft radio receiver is located a distance D beyond the midpoint of the screen, where D >> L. The refractive index in the scattering region is expressed as $n(\vec{r}) = 1 + n_0 + n_t(\vec{r})$, where n_0 corresponds to the average electron density, and n_t represents the irregularities ($\langle n_t \rangle = 0$, where $\langle\rangle$ denotes a statistical average). For the ionospheric occultations considered here, the gradient in n_0 had no appreciable effect on the scattering; hence, in the model for the ionosphere, n_0 is considered to be homogeneous ($\nabla n_0 = 0$). Furthermore, $1 + n_0 \approx 1$ for the electron densities in the ionospheres of Jupiter and Saturn (see equation 2.1 and Figures 4.2, 4.5, 4.7, 4.9, 5.2, and 5.4). It is also assumed that the refractive variations obey the Taylor hypothesis so that they can be considered "frozen" on time scales of interest. During the occultations of Voyager, the spacecraft velocity was sufficiently large to ensure

that the only significant time variation resulted from motion of the raypath across an essentially fixed field of spatial variations in refractive index (see Tables 4.1 and 5.1).

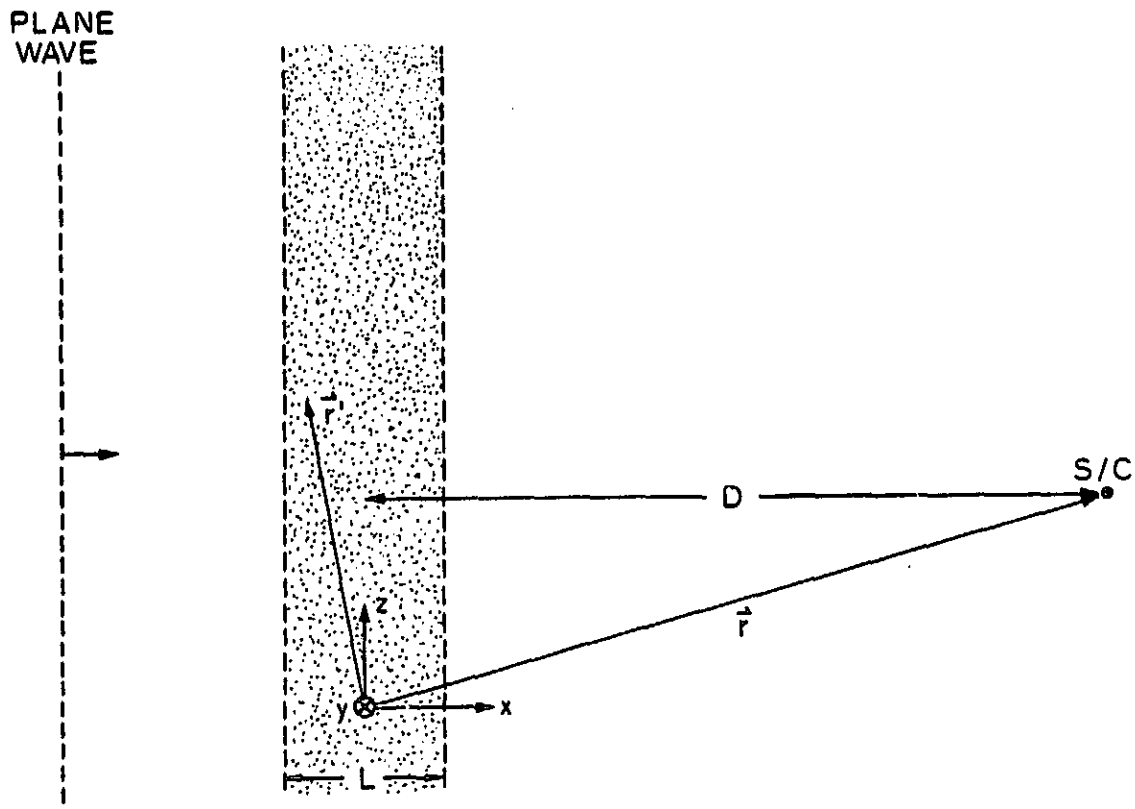

Figure A1 Idealized experimental geometry and coordinate system. A monochromatic plane wave propagating in the x-direction illuminates the scattering volume modeled as a screen of thickness L with transverse coordinates y, z. The origin of coordinates is at the center of the occulting planet. A radio receiver is situated a distance D beyond the screen, where D >> L.

In the Born approximation, the electric field at the receiver is the sum of the undisturbed incident wave, $\vec{E}_0(\vec{r})$, and a small perturbation due to scattering, $\vec{E}_s(\vec{r})$, which can be expressed as [cf. Tatarskii, 1971, p. 108]

$$\vec{E}_s(\vec{r}) = \frac{k^2}{2\pi} \iiint_V \frac{e^{jk|\vec{r}-\vec{r}'|}}{|\vec{r}-\vec{r}'|} n_t(\vec{r}') \vec{E}_0(\vec{r}') \, d^3r' \quad , \tag{A1}$$

where

$$\vec{E}_0 = \hat{z} \, e^{jkx} \quad .$$

Here, k is the radio wavenumber, $\hat{z}$ is the coordinate unit vector, the integration extends throughout the volume of the screen, V, and time dependence $\exp[-j2\pi f_r t]$ has been suppressed, where f_r is the radio frequency. Approximations used in deriving equation A1 impose the following restrictions on its validity [cf. Tatarskii, 1971, p. 103-106]

$$k|\vec{r}-\vec{r}'| \gg 1 \quad \text{and} \quad \lambda \ll \ell \quad , \tag{A2}$$

where λ is the free-space radio wavelength and ℓ is the smallest irregularity which contributes significantly to the scattered field (as opposed to the smallest irregularity present). The above inequalities are easily satisfied for the Voyager occultations by Jupiter, Saturn, and Titan, where $k|\vec{r}-\vec{r}'| > 10^8$ and $\lambda/\ell < 10^{-3}$. [Values of ℓ are 2 km for Jupiter (Chapter 4), 2 km for Saturn (Chapter 5), and 0.2 km for Titan (Chapter 7), while $\lambda \approx 10^{-4}$ km].

In the present case, the scattering angles are of order λ/ℓ or smaller [Tatarskii, 1971, p. 115]. Consequently, the principal contributions to $\vec{E}_s$ arise in the region of the screen contained within a radius $\lambda D/\ell$ from the straight-line path connecting spacecraft and earth. For mathematical convenience, the limits of integration over y and z can be extended indefinitely ($-\infty < y,z < +\infty$), since the remote regions of the screen produce a negligible contribution to $\vec{E}_s$. Furthermore, the small-angle approximation allows the expansion

$$|\vec{r}-\vec{r}'| \approx (x-x') + \frac{(y-y')^2+(z-z')^2}{2(x-x')} - \frac{[(y-y')^2+(z-z')^2]^2}{8(x-x')^3} \quad . \tag{A3}$$

Using A3, and neglecting second order corrections

$$\vec{E}_s(\vec{r}) \approx \vec{E}_o(\vec{r}) \frac{k^2}{2\pi} \iiint_V \frac{\exp\{\frac{jk}{2(x-x')}[(y-y')^2+(z-z')^2]\}}{(x-x')} \cdot n_t(\vec{r}') \, d^3r' \quad . \tag{A4}$$

Terms through second order in the expansion A3 have been retained in the exponential factor, which requires

$$\frac{k}{8(x-x')^3}[(y-y')^2+(z-z')^2]^2 \ll 2\pi \quad . \tag{A5}$$

For the region of the screen where the scattered signal originates, this inequality can be expressed as

$$(\lambda D)^{1/2} \ll \sqrt{8}\, \ell^2/\lambda \quad , \tag{A6}$$

where the left-hand side is the radius of the Fresnel zone. For the occultations considered here, the condition is easily satisfied (see Chapters 4, 5, and 7 for parameter values; typically, $(\lambda D)^{1/2} \approx 5$ km, $\ell \approx 1$ km, and $\lambda \approx 10^{-4}$ km).

As the scattered field remains polarized in the same sense as the incident field, both will be treated subsequently as scalar quantities. By convention, the weak-scattering theory solves for the first-order contributions to the log amplitude, χ, and phase, ϕ:

$$E(\vec{r}) \equiv E_0(\vec{r}) \exp(\chi + j\phi) \approx E_0(\vec{r}) \left[1 + \chi + j\phi\right] \quad . \tag{A7}$$

From expression A4,

$$\begin{aligned} E'(\vec{r}) &\equiv \chi(\vec{r}) + j\phi(\vec{r}) \\ &= \frac{k^2}{2\pi} \iiint_V \frac{\exp\left\{\frac{jk}{2(x-x')}\left[(y-y')^2 + (z-z')^2\right]\right\}}{(x-x')} n_t(\vec{r}') \, d^3r' \quad . \end{aligned} \tag{A8}$$

A.2.2 Statistics of the Scattered Field. In a statistical description of the scattered field, the quantities of interest are the autocovariance functions of amplitude and phase

$$\begin{aligned} B_\chi(\vec{r}_1, \vec{r}_2) &\equiv \langle \chi(\vec{r}_1) \, \chi(\vec{r}_2) \rangle \\ &= \frac{1}{2} \operatorname{Re}\left[\langle E'(\vec{r}_1) \, \overline{E'(\vec{r}_2)} \rangle + \langle E'(\vec{r}_1) \, E'(\vec{r}_2) \rangle\right] \quad , \end{aligned} \tag{A9}$$

$$B_{\phi}(\vec{r}_1,\vec{r}_2) \equiv \langle \phi(\vec{r}_1)\ \phi(\vec{r}_2)\rangle$$

$$= \frac{1}{2}\,\mathrm{Re}\,\left[\langle E'(\vec{r}_1)\ \overline{E'(\vec{r}_2)}\rangle - \langle E'(\vec{r}_1)\ E'(\vec{r}_2)\rangle\right] \quad , \tag{A10}$$

and the cross covariance of amplitude and phase at the same radio wavelength

$$B_{\chi\phi}(\vec{r}_1,\vec{r}_2) \equiv \langle \chi(\vec{r}_1)\ \phi(\vec{r}_2)\rangle$$

$$= \frac{1}{2}\,\mathrm{Im}\,\left[\langle E'(\vec{r}_1)\ E'(\vec{r}_2)\rangle - \langle E'(\vec{r}_1)\ \overline{E'(\vec{r}_2)}\rangle\right] \quad . \tag{A11}$$

In Equations A9-A11, Re and Im signify the real and imaginary parts, and overbars indicate complex conjugates.

It is assumed that the spatial variations of refractive index in the phase screen can be described as a locally homogeneous random field. In this case, the spatial covariance of refractive index, B_n, depends only on the separation of the observation points and obeys the following Fourier transform relationship [Tatarskii, 1971; Yaglom, 1962]:

$$B_n(\xi,\eta,\zeta) \equiv \langle n_t(x+\xi,y+\eta,z+\zeta)\ n_t(x,y,z)\rangle$$

$$= \int_{-\infty}^{+\infty}\!\!\int\!\!\int \exp[j(\kappa_x\xi + \kappa_y\eta + \kappa_z\zeta)]\ \Phi(\vec{\kappa})\ d\kappa_x d\kappa_y d\kappa_z \quad , \tag{A12}$$

$$\Phi_n(\vec{\kappa}) = \frac{1}{(2\pi)^3}\int_{-\infty}^{+\infty}\!\!\int\!\!\int \exp[-j(\kappa_x\xi + \kappa_y\eta + \kappa_z\zeta)]\ B_n(\xi,\eta,\zeta)\ d\xi\ d\eta\ d\zeta \quad .$$

Here, Φ_n is the three-dimensional spatial spectrum of variations in

refractive index, and κ_x, κ_y, and κ_z are the Cartesian components of the wave vector, $\vec{\kappa}$.

The general expressions for the covariance functions in equations A9-A11 will be evaluated for the present case by using equation A8; two moments of the scattered electric field must be calculated. First,

$$\langle E'(\vec{r}_1)\,\overline{E'(\vec{r}_2)}\rangle = \frac{k^4}{4\pi^2}\iiint_V \iiint_V \langle n_t(\vec{r}')\, n_t(\vec{r}'')\rangle \cdot \frac{\exp\{\frac{jk}{2(x_1-x')}\,[(y_1-y')^2+(z_1-z')^2]\}}{(x_1-x')} \cdot \frac{\exp\{\frac{-jk}{2(x_2-x'')}\,[(y_2-y'')^2+(z_2-z'')^2]\}}{(x_2-x'')}\, d^3r'\, d^3r'' \quad . \tag{A13}$$

After substitution from A12, the integrals over y', z', y'', and z'' separate into factors such as (for y')

$$I \equiv \int_{-\infty}^{+\infty} \exp\left[j\kappa_y y' + \frac{jk}{2(x_1-x')}\,(y_1-y')^2\right] dy' \quad , \tag{A14}$$

which can be integrated analytically to obtain

$$I = (1+j)\left(\frac{\pi(x_1-x')}{k}\right)^{1/2} \exp\left\{j\left[\kappa_y y_1 - \frac{\kappa_y^2 (x_1-x')}{2k}\right]\right\} \quad . \tag{A15}$$

After integration over x', x'', y', y'', z', and z'', expression A13 reduces to

$$\langle E'(\vec{r}_1)\,\overline{E'(\vec{r}_2)}\rangle = k^2 \iiint_{-\infty}^{+\infty} \Phi_n(\vec{\kappa}) \left\{\frac{\sin[(\beta + \kappa_x)\, L/2]}{(\beta + \kappa_x)/2}\right\}^2 \cdot \exp\{j[-\beta(x_1 - x_2) + \kappa_y(y_1 - y_2) + \kappa_z(z_1 - z_2)]\}\, d\kappa_x d\kappa_y d\kappa_z \quad , \tag{A16}$$

where $\beta \equiv \left(\frac{\kappa_y^2 + \kappa_z^2}{2k}\right)$.

Consider the two factors in the integrand of A16 which depend on κ_x. In the present study, it is assumed that Φ_n obeys a power law of the general form (see section 2.3.1)

$$\Phi_n \propto \frac{1}{[1 + \kappa_o^{-2}(\kappa_x^2 + \kappa_y^2 + \kappa_z^2)]^{p/2}} \quad , \tag{A17a}$$

where $2\pi/\kappa_o$ corresponds to the outer scale. On the basis of the results in Chapters 4, 5, and 7, it was concluded that $\kappa_x^2 + \kappa_y^2 + \kappa_z^2 \gg \kappa_o^2$ for the Voyager observations at Jupiter, Saturn, and Titan. Then, to a good approximation

$$\Phi_n \propto (\kappa_x^2 + \kappa_y^2 + \kappa_z^2)^{-p/2} \quad . \tag{A17b}$$

As a function of κ_x, Φ_n has width of order $(\kappa_y^2 + \kappa_z^2)^{1/2}$, and is symmetrical about $\kappa_x = 0$. The second factor

$$J \equiv \left\{\frac{\sin[(\beta + \kappa_x)\, L/2]}{(\beta + \kappa_x)/2}\right\}^2 \quad , \tag{A18}$$

has area $2\pi L$ and width $2\pi/L$. As $2\pi/L$ is extremely narrow compared to the width of Φ_n (the observed irregularities are much smaller than the thickness of the phase screen), J behaves much like a delta function, so that the integration of A16 over κ_x yields

$$\langle E'(\vec{r}_1)\,\overline{E'(\vec{r}_2)}\rangle \approx 2\pi k^2 L \iint_{-\infty}^{+\infty} \Phi_n(0,\kappa_y,\kappa_z) \cdot \exp\{j[-\beta(x_1 - x_2) + \kappa_y(y_1 - y_2) + \kappa_z(z_1 - z_2)]\}\, d\kappa_y d\kappa_z \quad , \tag{A19}$$

where $\Phi_n(-\beta,\kappa_y,\kappa_z) \approx \Phi_n(0,\kappa_y,\kappa_z)$. This last approximation is easily satisfied, which can be seen by considering A17b and the definition of β:

$$\begin{aligned} \beta^2 + \kappa_y^2 + \kappa_z^2 &= (\kappa_y^2 + \kappa_z^2)\left(1 + \frac{\kappa_y^2 + \kappa_z^2}{4k^2}\right) \\ &\leq (\kappa_y^2 + \kappa_z^2)\left(1 + \left(\frac{\lambda}{2\ell}\right)^2\right) \\ &\approx (\kappa_y^2 + \kappa_z^2) \quad , \end{aligned} \tag{A20}$$

by condition A2. As indicated by the condition $\kappa_x = 0$ in the argument of Φ_n, the field scattered at small angles is insensitive to refractive variations along the line of sight.

An expression for $\langle E'(\vec{r}_1)\, E'(\vec{r}_2)\rangle$ can be derived in a similar fashion by using equations A8 and A12, and evaluating the integrals over x', x'', y', y'', z', and z'' (as in A14 and A15):

$$\langle E'(\vec{r}_1)\, E'(\vec{r}_2)\rangle = -k^2 \iiint_{-\infty}^{+\infty} \Phi_n(\vec{\kappa}) \cdot \exp\{j[-\beta(x_1+x_2) + \kappa_y(y_1-y_2) + \kappa_z(z_1-z_2)]\} \cdot \frac{\sin[(\kappa_x+\beta)\,L/2]\,\sin[(\kappa_x-\beta)\,L/2]}{(\kappa_x+\beta)\,(\kappa_x-\beta)/4}\, d\kappa_x d\kappa_y d\kappa_z \quad . \tag{A21}$$

Consider the κ_x-dependence of the integrand in A21, which contains a factor similar to J in A18

$$K \equiv \frac{\sin[(\kappa_x+\beta)\,L/2]\,\sin[(\kappa_x-\beta)\,L/2]}{(\kappa_x+\beta)\,(\kappa_x-\beta)/4} \quad . \tag{A22}$$

Using the same arguments as applied previously to the function J, K can be approximated as a delta function when integrating over κ_x:

$$\langle E'(\vec{r}_1)\, E'(\vec{r}_2)\rangle \approx -2\pi k^2 L \iint_{-\infty}^{+\infty} \Phi_n(0,\kappa_y,\kappa_z)\, \frac{\sin(\beta L)}{\beta L} \cdot \exp\{j[-\beta(x_1+x_2) + \kappa_y(y_1-y_2) + \kappa_z(z_1-z_2)]\}\, d\kappa_y d\kappa_z \quad . \tag{A23}$$

When substituted into equations A9-A11, A19 and A23 yield expressions for the autocovariance and cross covariance functions of amplitude and phase:

$$\begin{matrix} B_\chi(\vec{r}_1,\vec{r}_2) \\ B_\phi(\vec{r}_1,\vec{r}_2) \end{matrix} = \pi k^2 L \int\int_{-\infty}^{+\infty} \Phi_n(0,\kappa_y,\kappa_z) \exp\{j[\kappa_y(y_1 - y_2) + \kappa_z(z_1 - z_2)]\}$$

$$\cdot\{\cos[\beta(x_1 - x_2)] \mp \frac{\sin(\beta L)}{\beta L} \cos[\beta(x_1 + x_2)]\}\, d\kappa_y d\kappa_z \quad , \tag{A24}$$

$$B_{\chi\phi}(\vec{r}_1,\vec{r}_2) = \pi k^2 L \int\int_{-\infty}^{+\infty} \Phi_n(0,\kappa_y,\kappa_z) \exp\{j[\kappa_y(y_1 - y_2) + \kappa_z(z_1 - z_2)]\}$$

$$\cdot\{\sin[\beta(x_1 - x_2)] + \frac{\sin(\beta L)}{\beta L} \sin[\beta(x_1 + x_2)]\}\, d\kappa_y d\kappa_z \quad , \tag{A25}$$

Note that $\Phi_n(0,\kappa_y,\kappa_z) = \Phi_n(0,-\kappa_y,-\kappa_z)$, (see A17), so that the above expressions are real valued. Equations A24 and A25 are identical to the results obtained for scattering from a slab of finite thickness in the Rytov approximation [Yeh and Liu, 1982; also see related comments concerning the Rytov and Born approximations in Appendix B].

Consider the parameter βL in equations A24 and A25. By definition

$$\beta L \equiv \left(\frac{\kappa_y^2 + \kappa_z^2}{2k}\right) L \leq \pi\left(\frac{\lambda L}{\ell^2}\right) \quad . \tag{A26}$$

If the irregularities are larger than the radius of the Fresnel zone, $(\lambda L)^{1/2}$, as seen by an observer positioned near $x = L/2$, then $\beta L \ll \pi$ and $(\sin \beta L)/\beta L \approx 1$. Under this condition, the field emerging from the scattering volume can be calculated accurately using

geometrical optics, and the occulting atmosphere behaves like a thin phase-changing screen [Salpeter, 1967; Bramley, 1977].

Noting that $x_1 - x_2 \leq L$ for the observations reported here, and applying the thin-screen approximation

$$\begin{matrix} B_\chi(\eta,\zeta) \\ B_\phi(\eta,\zeta) \end{matrix} = 2\pi k^2 L \int_{-\infty}^{+\infty}\int \Phi_n(0,\kappa_y,\kappa_z)\, \exp[j(\kappa_y\eta + \kappa_z\zeta)] \cdot \begin{matrix} \sin^2 \\ \cos^2 \end{matrix} \left[\frac{\kappa^2 D}{2k}\right] d\kappa_y d\kappa_z \quad , \tag{A27}$$

$$B_{\chi\phi}(\eta,\zeta) = 2\pi k^2 L \int_{-\infty}^{+\infty}\int \Phi_n(0,\kappa_y,\kappa_z)\, \exp[j(\kappa_y\eta + \kappa_z\zeta)] \cdot \sin\left[\frac{\kappa^2 D}{2k}\right] \cos\left[\frac{\kappa^2 D}{2k}\right] d\kappa_y d\kappa_z \quad , \tag{A28}$$

where $\kappa^2 = \kappa_y^2 + \kappa_z^2$, and $x_1 + x_2 \approx 2D$. For a homogeneous spectrum, Φ_n, the covariance functions depend strongly on the transverse separation of the observation points $\eta = y_1 - y_2$ and $\zeta = z_1 - z_2$, while the weak dependence on the separation along the line of sight, $x_1 - x_2$, can be neglected.

Let us assume that the amplitude of the irregularities is a constant fraction of the background refractive index. The quantity $(2rH)^{1/2}$ is then a good approximation to the phase screen thickness L, where r is the planet's radius and H is the atmosphere's scale height. For Jupiter, $r \approx 7 \cdot 10^4$ km, and $H \approx 10^3$ km in the upper ionosphere [Eshleman et al., 1979b, c], so that $L \approx 10^4$ km; for Saturn, $r \approx 6 \cdot 10^4$ km, and $H \approx 10^3$ km in the upper ionosphere [Tyler et al., 1981a, 1982], so that $L \approx 10^4$ km; in Titan's atmosphere near the

tropopause, $r \approx 2600$ km and $H \approx 16$ km [Tyler et al., 1981a], which give $L \approx 300$ km. At the wavelengths of the Voyager data and the values of ℓ in Sections 4.3, 5.3, and 7.3, $\beta L < \pi/4$ so that $(\sin \beta L)/\beta L \approx 1$. Therefore, the thin-screen approximation can be applied safely when considering the signal scintillations measured during the Voyager occultations.

A.3 Temporal Spectra: Homogeneous Background

The temporal covariance of amplitude fluctuations, $R_\chi(\tau)$, is related to the spatial covariance function in A27 through

$$R_\chi(\tau) = B_\chi(v_y\tau,\ v_z\tau) \quad , \tag{A29}$$

where v_y and v_z are the transverse components of spacecraft velocity (i.e., parallel to the phase screen), and τ is the time delay of the measurement. By definition, the temporal Fourier transform of A29 yields the spectrum of amplitude fluctuations

$$W_\chi(\omega) = \frac{1}{2\pi} \int_{-\infty}^{+\infty} B_\chi(v_y\tau, v_z\tau)\, \exp(-j\omega\tau)\, d\tau \quad , \tag{A30}$$

where ω is the fluctuation frequency. After substitution from A27 and integration over τ (which produces a delta function)

$$W_\chi(\omega) = 2\pi k^2 L \int\int_{-\infty}^{+\infty} \Phi_n(0,\kappa_y,\kappa_z)\, \delta\lfloor \kappa_y v_y + \kappa_z v_z - \omega \rfloor \cdot \sin^2\lfloor \frac{\kappa^2 D}{2k} \rfloor\, d\kappa_y d\kappa_z \quad . \tag{A31}$$

For the case of a homogeneous average refractive index, the transverse raypath velocity in the phase screen, $\vec{v}_*$, is given by (see Appendix D)

$$\vec{v}_* = v_y\hat{y} + v_z\hat{z} \quad . \tag{A32}$$

From this consideration, the physical significance of the delta function in A31 becomes clear: under the Taylor hypothesis, the contributions to amplitude fluctuations at frequency ω arise from irregularities with wave vectors that satisfy

$$\omega = \vec{\kappa}_\perp \cdot \vec{v}_* \quad , \tag{A33}$$

where

$$\vec{\kappa}_\perp = \kappa_y\hat{y} + \kappa_z\hat{z} \quad .$$

Changing variables of integration, A31 becomes

$$w_\chi(\omega) = 2\pi k^2 L \int_0^\infty \int_0^{2\pi} \Phi_n(0,\kappa\cos\varepsilon,\kappa\sin\varepsilon)\ \delta\lfloor\kappa v_* \cos(\varepsilon-\gamma) - \omega\rfloor \cdot \sin^2\lfloor\frac{\kappa^2 D}{2k}\rfloor\ \kappa\, d\kappa\, d\varepsilon \quad . \tag{A34}$$

where $\kappa_y = \kappa\cos\varepsilon$, $\kappa_z = \kappa\sin\varepsilon$, and γ is the angle between $\vec{v}_*$ and the y-axis. Figure A2 shows the coordinate system used in equation A34 along with the angles ε and γ.

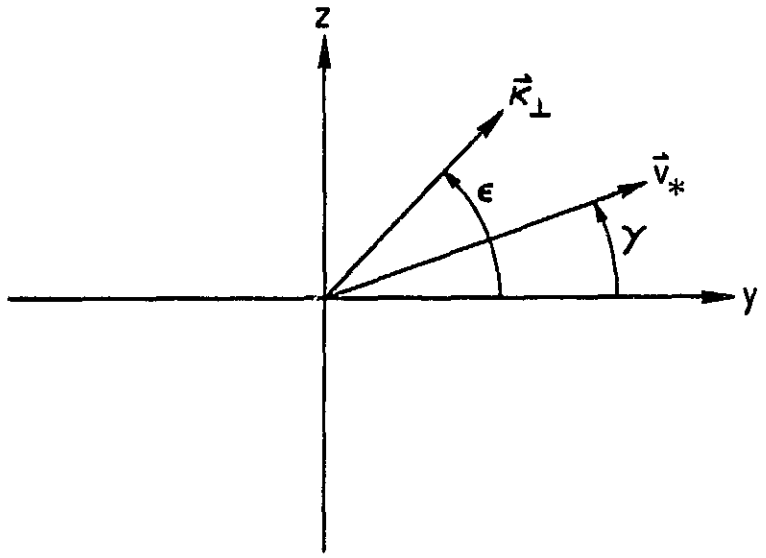

Figure A2 Phase-screen coordinate system. The angles γ and ϵ indicate the orientations of the transverse raypath velocity, $\vec{v}_*$, and the transverse wave vector, $\vec{\kappa}_\perp$, respectively.

Equation A34 can be integrated by using the following property of delta functions

$$\int_{-\infty}^{+\infty} \delta[f(x)]\, dx = \frac{1}{|f'(x_0)|} \quad , \tag{A35}$$

where $f(x_0) = 0$ and $f'(x_0) \neq 0$. Noting that the argument of the delta function in A34 has value zero only if $\kappa \geq \omega/v_*$, and applying A35 to the integration over ε

$$w_\chi(\omega) = 2\pi k^2 L \int_{\omega/v_*}^{+\infty} \frac{1}{(\kappa^2 v_*^2 - \omega^2)^{1/2}} \sum_{i=1}^{2} \Phi_n(0, \kappa\cos\varepsilon_i, \kappa\sin\varepsilon_i) \cdot \sin^2\left[\frac{\kappa^2 D}{2k}\right] \kappa\, d\kappa \quad , \tag{A36}$$

$$\varepsilon_1 \equiv \gamma + \cos^{-1}(\omega/\kappa v_*) \quad , \quad \varepsilon_2 \equiv \gamma - \cos^{-1}(\omega/\kappa v_*) \quad .$$

The lower limit for κ-integration is a consequence of condition A33.

Similar expressions can be derived for the phase and cross amplitude-phase spectra

$$w_\phi(\omega) = 2\pi k^2 L \int_{\omega/v_*}^{+\infty} \frac{1}{(\kappa^2 v_*^2 - \omega^2)^{1/2}} \sum_{i=1}^{2} \Phi_n(0, \kappa\cos\varepsilon_i, \kappa\sin\varepsilon_i) \cdot \cos^2\left[\frac{\kappa^2 D}{2k}\right] \kappa\, d\kappa \quad , \tag{A37}$$

$$w_{\chi\phi}(\omega) = 2\pi k^2 L \int_{\omega/v_*}^{+\infty} \frac{1}{(\kappa^2 v_*^2 - \omega^2)^{1/2}} \sum_{i=1}^{2} \Phi_n(0, \kappa\cos\varepsilon_i, \kappa\sin\varepsilon_i) \cdot \frac{1}{2} \sin\left[\frac{\kappa^2 D}{k}\right] \kappa\, d\kappa \quad . \tag{A38}$$

A.4 Transverse Coordinates in the Phase Screen

In order to complete the theoretical discussion of weak scattering from a phase screen with a homogeneous background, a specific definition of the transverse coordinates (y, z) is required. A simple choice for the orientation of the y- and z-axes follows directly from the fundamental characteristics of the refractive irregularities. In the ionospheric occultations considered here, the magnetic field influenced the shape of the plasma irregularities, and hence the characteristics of the scattered signals. In contrast, the overall effect of the ionosphere's finite scale height was negligible. Consequently, in a convenient alignment of the transverse coordinates, the y-direction coincides with the projection of the magnetic field onto the y-z plane (see Section 2.3.1 and Figure 2.1). This coordinate system was adopted in Chapters 4, 5, and 6 when applying equations A36-A38 to interpret scintillations observed during the occultations of Voyager by Jupiter and Saturn.

In Sections A.5 and A.6, equations A27, A28, and A36-A38 are modified to account for the effect of Fresnel zone distortion. The resulting formulas were applied in Chapter 7 to interpret weak scattering from Titan's neutral atmosphere during the radio occultation of Voyager 1. As a consequence of atmospheric stratification, the equations now are expressed most conveniently by using a coordinate system in which the y-axis coincides with the visible limb of the planet, and the z-axis is directed vertically, opposite to the gravitational acceleration at ray periapsis (see Section 2.3.2 and Figure 2.2). In general, this y-z orientation differs from the field-aligned system defined above.

A.5 Covariance Functions: Inhomogeneous Background.

In the preceding derivation, the average refractive index in the phase screen was assumed to be essentially homogeneous. In order to remove this restriction from the previous results, the refractive index now is expressed as $n(\vec{r}) = 1 + n_0(r) + n_t(\vec{r})$, where $n_0(r)$ represents the spherically symmetrical quiescent atmosphere. The covariance functions, A27 and A28, can be generalized accordingly by noting that the inhomogeneous background affects the scattering in two ways (see Appendix D). First, for an observer at the spacecraft, the Fresnel zone is distorted to horizontal and vertical dimensions $(\phi_y \lambda D)^{1/2}$ and $(\phi_z \lambda D)^{1/2}$, respectively. Second, horizontal and vertical separations δy and δz in the phase screen are transformed by differential refraction to equivalent separations $\delta y/\phi_y$ and $\delta z/\phi_z$ in the plane of the spacecraft (x = D in Figure D1). Expressions which account for the inhomogeneous background are obtained by introducing these corrections into A27 and A28:

$$\begin{matrix} B_\chi(\eta,\zeta) \\ B_\phi(\eta,\zeta) \end{matrix} = 2\pi k^2 L \int_{-\infty}^{+\infty}\int \Phi_n(0,\kappa_y,\kappa_z)\, \exp\left[j(\phi_y\kappa_y\eta + \phi_z\kappa_z\zeta)\right] \cdot \begin{matrix} \sin^2 \\ \cos^2 \end{matrix}\left[\frac{D}{2k}(\phi_y\kappa_y^2 + \phi_z\kappa_z^2)\right] d\kappa_y d\kappa_z \quad , \tag{A39}$$

$$B_{\chi\phi}(\eta,\zeta) = 2\pi k^2 L \int_{-\infty}^{+\infty}\int \Phi_n(0,\kappa_y,\kappa_z)\, \exp\left[j(\phi_y\kappa_y\eta + \phi_z\kappa_z\zeta)\right] \cdot \sin\left[\frac{D}{2k}(\phi_y\kappa_y^2 + \phi_z\kappa_z^2)\right] \cos\left[\frac{D}{2k}(\phi_y\kappa_y^2 + \phi_z\kappa_z^2)\right] d\kappa_y d\kappa_z \quad . \tag{A40}$$

Two important properties can be inferred from equation A39 for the case of scattering from a neutral planetary atmosphere. First, when Φ_n obeys an inverse power law with exponent p (cf. equation A17), it can be shown through a change of variables that $B_\chi(0,0) \equiv \langle\chi^2\rangle$ has radio wavelength dependence $\lambda^{p/2-3}$ [Tatarskii, 1971; Young, 1976]. Second, from equation A12, $\Phi_n \propto \langle n_t^2\rangle$, and it is clear that $\langle\chi^2\rangle \propto \langle n_t^2\rangle$. Furthermore, as refractivity is proportional to density for nonpolar gases [Essen and Froome, 1951; Tyler and Howard, 1969; Eshleman, 1973; also see Section 2.2], both $\langle n_t^2\rangle$ and $\langle\chi^2\rangle$ are proportional to the variance of fluctuations in gas density in the occulting atmosphere.

A.6 Temporal Spectra: Inhomogeneous Background

Temporal spectra also can be derived from equations A39 and A40 by following the procedure in Section A.3, which yields

$$W_\chi(\omega) = 2\pi k^2 L \int_{\omega/v_*}^{+\infty} \frac{1}{(\kappa^2 v_*^2 - \omega^2)^{1/2}} \sum_{i=1}^{2} \Phi_n(0, \kappa\cos\varepsilon_i, \kappa\sin\varepsilon_i) \cdot \sin^2\left[\frac{\kappa^2 D}{2k}(\phi_y\cos^2\varepsilon_i + \phi_z\sin^2\varepsilon_i)\right] \kappa\, d\kappa \quad , \tag{A41}$$

$$\varepsilon_1 \equiv \gamma + \cos^{-1}(\omega/\kappa v_*) \quad , \quad \varepsilon_2 \equiv \gamma - \cos^{-1}(\omega/\kappa v_*) \quad .$$

$$W_\phi(\omega) = 2\pi k^2 L \int_{\omega/v_*}^{+\infty} \frac{1}{(\kappa^2 v_*^2 - \omega^2)^{1/2}} \sum_{i=1}^{2} \Phi_n(0, \kappa\cos\varepsilon_i, \kappa\sin\varepsilon_i) \cdot \cos^2\left[\frac{\kappa^2 D}{2k}(\phi_y\cos^2\varepsilon_i + \phi_z\sin^2\varepsilon_i)\right] \kappa\, d\kappa \quad . \tag{A42}$$

$$W_{\chi\phi}(\omega) = 2\pi k^2 L \int_{\omega/v_*}^{+\infty} \frac{1}{(\kappa^2 v_*^2 - \omega^2)^{1/2}} \sum_{i=1}^{2} \Phi_n(0, \kappa\cos\varepsilon_i, \kappa\sin\varepsilon_i) \cdot \frac{1}{2} \sin\left[\frac{\kappa^2 D}{k}(\phi_y \cos^2\varepsilon_i + \phi_z \sin^2\varepsilon_i)\right] \kappa \, d\kappa \quad . \tag{A43}$$

In this case, differential refraction modifies $\vec{v}_*$, the raypath velocity in the phase screen, according to (see Appendix D)

$$\vec{v}_* = \phi_y v_y \hat{y} + \phi_z v_z \hat{z} \quad . \tag{A44}$$

Equations A41-A43 reduce to equations A36-A38 when $\phi_y = \phi_z = 1$, which corresponds to a homogeneous average refractive index, $n_0(r)$ = constant.

A.7 The Relationship Between Amplitude and Intensity Fluctuations

This section discusses the simple relationships among amplitude, log amplitude, and intensity fluctuations for the case of weak scattering, and summarizes the notation for these quantities.

In equation A7, the electric field at the receiver was expressed as

$$E(\vec{r}) = E_0(\vec{r}) \cdot \exp(\chi + j\phi) \approx E_0(\vec{r}) \cdot [1 + \chi + j\phi] \quad , \tag{A7}$$

where $E_0(\vec{r})$ represents the undisturbed field. The approximation is valid under conditions of weak scattering, since the fluctuations in log amplitude, χ, and phase, ϕ, then satisfy $\chi, \phi << 1$ (see Tatarskii [1971, pp. 253-258] and Appendix B).

The first-order intensity follows from equation A7:

$$I(\vec{r}) \approx I_0(\vec{r}) \cdot [1 + 2\chi] \quad . \tag{A45}$$

Then, from equations 3.1 and 3.4, the normalized amplitude, a(t), and the normalized intensity, i(t), are related to $\chi(t)$ through

$$\begin{aligned} a(t) &= \chi(t) \quad , \\ i(t) &= 2\chi(t) \quad . \end{aligned} \tag{A46}$$

By applying this result, the covariance function for intensity can be expressed as

$$B_i(\vec{r}_1,\vec{r}_2) \equiv \langle i(\vec{r}_1)\, i(\vec{r}_2)\rangle = 4 \cdot B_\chi(\vec{r}_1,\vec{r}_2) \quad . \tag{A47}$$

In particular,

$$\langle i^2\rangle = 4 \cdot \langle \chi^2\rangle \quad . \tag{A48}$$

Similarly, the temporal spectrum of intensity fluctuations is given by

$$w_i(\omega) = 4 \cdot w_\chi(\omega) \quad . \tag{A49}$$

This completes the theoretical derivations.

APPENDIX B

A LIMIT FOR VALIDITY OF THE WEAK-SCATTERING THEORY

In the Born approximation, only first-order terms are retained in the perturbation expansion for the scattered field. Consequently, the results in Appendix A remain valid only for small signal fluctuations. In discussing the condition for validity of the weak-scattering theory, it is useful to define the intensity variance

$$\sigma_i^2 \equiv \left\langle \left[\frac{I - \langle I \rangle}{\langle I \rangle} \right]^2 \right\rangle \quad , \tag{B1}$$

where $I = E_0^2 \cdot \exp(2\chi)$ is the signal intensity (see equation A7), and $\langle\ \rangle$ represents an average over time. For weak scattering, this quantity is related to the variance of log amplitude through $\sigma_i^2 \approx 4\langle\chi^2\rangle$ (cf. Section A.7).

An upper limit on σ_i^2 consistent with the Born approximation can be established from the predictions of theories that properly account for strong scattering. In the weak-scattering theory, an increase in the variance of refractive index (the parameter Q in Section 2.3.1) scales the intensity spectrum but does not change its shape on a logarithmic display. Marians [1975] has computed intensity spectra based on the theory for strong scattering from a thin screen [Rumsey, 1975]; as shown in Figure 6 of Marians [1975], the shape of the intensity spectrum begins to depart from the predictions of the weak-scattering theory when σ_i^2 increases beyond about 0.3. Similar computations by Rino [1980] are consistent with this limit (see his Figure 5). Apparently, the weak-scattering theory is valid only when $\sigma_i^2 \lesssim 0.3$, for which

$\langle\chi^2\rangle \lesssim 0.08$. For all data analyzed in Chapters 4, 5, and 7, $\sigma_1^2 < 0.25$, so the weak-scattering theory can be applied safely.

An empirical test of the weak-scattering assumption was obtained as follows. Spectra of the intensity fluctuations can be computed by normalizing the data in two ways

$$i_1 = \frac{I - \langle I\rangle}{\langle I\rangle} \quad , \qquad (B2)$$

$$i_2 = \ln(I) - \langle \ln(I)\rangle \quad .$$

For weak scattering, χ is small so that $\exp(2\chi) \approx 1 + 2\chi$, and the intensity spectra obtained from i_1 and i_2 are essentially identical. When the limits of weak scattering are exceeded, higher-order terms must be included in the expansion of $\exp(2\chi)$, and the spectra computed from i_1 and i_2 are different. A comparison of intensity spectra based on these two normalizations confirms that the Voyager data considered here correspond to weak scattering.

It should be noted that some authors have adopted a less stringent condition for the validity of the weak-scattering theory. Tatarskii [1971, p. 258] stated that the Rytov approximation is justified when $\langle\chi^2\rangle \lesssim 0.64$. However, at that time, the Rytov approximation was believed to constitute an improvement over the conventional perturbation techniques based on the Born approximation, which is strictly limited to single scattering. More recently, it has been recognized that the Rytov approximation does not properly account for multiple scattering and actually is equivalent to the single scattering formulations, and limited to about the same range of validity $\sigma_1^2 \lesssim 0.3$ [Fante, 1975;

Brown, 1966]. Woo and Yang [1976, 1978] adopted Tatarskii's criterion and applied the weak-scattering theory to interpret amplitude spectra when $\langle\chi^2\rangle$ was as large as 0.37, which is well above the limit for weak scattering imposed here.

The preceding discussion strictly applies only to the case of scattering from a thin phase screen with a homogeneous average refractive index. However, it can be shown [cf. Haugstad, 1982] that approximately the same upper limit on $\langle\chi^2\rangle$ is appropriate when the phase screen includes an inhomogeneous background.

APPENDIX C

A PHYSICAL INTERPRETATION OF THE WEAK-SCATTERING THEORY

C.1 Introduction

The general behavior of weakly-scattered, short-wavelength radio waves has been discussed previously [Ratcliffe, 1956; Lee and Harp, 1969; Briggs, 1975; Uscinski, 1977]. Here, those results are extended in order to gain some insight into the mathematical formulas of Appendix A. In particular, this appendix explains the basic relationship between the morphology of the scattering irregularities and the appearance of the temporal spectra of the received signal. It is emphasized that the spectra are sensitive to variations in both the axial ratio and the orientation of anisotropic irregularities.

Section C.2 provides a basis for subsequent discussions by analyzing a simple scattering problem. Section C.3 then applies the results to account for the principal features of the amplitude and phase spectra. Certain characteristics of the cross amplitude-phase spectrum are discussed briefly in Section C.4. These results have been published elsewhere [Hinson and Tyler, 1982].

C.2 The Field Scattered from a Homogeneous Phase Screen

It is useful to begin by analyzing a simple scattering problem; Figure A1 shows the geometry. A monochromatic plane wave propagating in the x-direction illuminates the scattering volume, modeled as a thin phase screen with transverse coordinates y, z. At position x = D, a spacecraft receiver samples the perturbed wave. Consider the case in which the refractive index in the thin screen is given by

$$n(x',y',z') = 1 + n_1\cos(\kappa_y y' + \kappa_z z') \quad , \tag{C1}$$

where the constant $n_1 << 1$, and the average refractive index is independent of position. Note that $2\pi/\kappa_y$ and $2\pi/\kappa_z$ represent the characteristic length scales of refractive variations in the y- and z-directions, respectively. For short radio wavelengths, the radio wavenumber $k >> \kappa_y, \kappa_z$. Far beyond the screen, at location (x = D, y, z), the scattered field, E_s, will consist of two plane waves inclined at small angles relative to the original direction of propagation [Ratcliffe, 1956]:

$$E_s(x,y,z) = jM\{\exp[j(\kappa_y y + \kappa_z z)] + \exp[-j(\kappa_y y + \kappa_z z)]\} \cdot \exp\{j[x(k^2-\kappa^2)^{1/2} - 2\pi f_r t]\} \quad . \tag{C2}$$

Here, the real constant M is proportional to n_1 and represents the strength of the scattered field, f_r is the radio frequency, and $\kappa^2 \equiv \kappa_y^2 + \kappa_z^2$.

By expanding

$$(k^2-\kappa^2)^{1/2} \approx k - \frac{\kappa^2}{2k} \quad , \tag{C3}$$

and supressing the propagation factor, $\exp[j(kx-2\pi f_r t)]$, the amplitude and phase perturbations (χ and ϕ, respectively, in the notation of equation A7) can be expressed as

$$\chi = 2M \cdot \cos(\kappa_y y + \kappa_z z) \cdot \sin(\frac{\kappa^2 x}{2k}) \quad ,$$

$$\phi = 2M \cdot \cos(\kappa_y y + \kappa_z z) \cdot \cos(\frac{\kappa^2 x}{2k}) \quad . \tag{C4}$$

The pair of scattered plane waves interfere with one another in such a way that at locations where the amplitude perturbation is maximum (for example, $x = \frac{2k}{\kappa^2}\frac{\pi}{2}$) , the phase perturbation is zero, and at locations where χ is zero (for example, x=0), the magnitude of ϕ is maximum. The size of the irregularity, $2\pi/\kappa$, relative to the radius of the Fresnel zone, $(\lambda x)^{1/2}$, determines the strength of the interference effect through the factors $\sin(\frac{\kappa^2 x}{2k})$ and $\cos(\frac{\kappa^2 x}{2k})$. These factors, which appeared in equations A27 and A28 for the covariance functions, will be referred to as the Fresnel filters in amplitude and phase, respectively [cf. Briggs, 1975]. Note that amplitude fluctuations develop only at a distance greater than about $x \approx \pi k/2\kappa^2$ beyond the screen. Conversely, at a given distance beyond the screen, only irregularities on the order of Fresnel-zone size or smaller, such that $\kappa \geq \pi/(\lambda x)^{1/2}$, will cause significant amplitude fluctuations (cf. equation C4). As the variation with x is gradual ($k >> \kappa$), the time variations in χ and ϕ result

essentially from spacecraft motion parallel to the phase screen. In the case above, the fluctuation frequency is $\omega = \vec{\kappa} \cdot \vec{v}_*$, where $\vec{v}_*$ is the transverse raypath velocity and $\vec{\kappa}$ is the wavevector with components κ_y and κ_z (cf. Section A.3).

In order to model a planetary atmosphere, the phase screen must include a distribution of irregularities, such as the one in equation C1, with various wave vectors as specified by the spectrum, $\Phi_n(\vec{\kappa})$ (see equation A12 and Section 2.3.1). However, for a statistically homogeneous $\Phi_n(\vec{\kappa})$, irregularities with different wave vectors are independent [Tatarskii, 1971, p. 22-25; Yaglom, 1962]. In this case, the weakly-scattered electric field (see equations A27 and A28) consists of a linear superposition of independent components, each in the form of a pair of plane waves, such as the one just analyzed. This representation of the field as a spectrum of plane waves is useful for interpreting the temporal spectra of signal fluctuations [cf. Uscinski, 1977].

C.3 The Temporal Spectra of Amplitude and Phase

The principal features of the temporal spectrum of amplitude fluctuations, $W_\chi(\omega)$, can be explained in terms of the simple concepts discussed above. First, consider scattering from a power-law spectrum of isotropic irregularities (e = f = 1 in equation 2.4), so that

$$\Phi_n(\vec{\kappa}) \propto \kappa^{-p} \quad . \tag{C5}$$

For the observations by Voyager, $3 < p < 4$ (see Chapters 4, 5, and 7). The amplitude fluctuations at frequency ω originate from those

refractive irregularities where the wave vectors satisfy $\vec{\kappa}\cdot\vec{v}_{\perp} = \omega$. The Fresnel filter, plus $\Phi_n(\vec{\kappa})$, which gives the strength of the irregularities, determine the size of each contribution to the scattered signal. As $\Phi_n(\vec{\kappa})$ rapidly decreases with increasing κ, the principal contribution to $w_\chi(\omega)$ arises from the "first pass band" of the amplitude Fresnel filter, which corresponds to irregularities of size near the Fresnel zone radius (see Figure C1). This is a well known result of the wave-optics theory [Tatarskii, 1971]. Fresnel-zone-size variations in the screen contribute to $w_\chi(\omega)$ at frequencies roughly less than or equal to

$$\omega_c \equiv \frac{\sqrt{2\pi}|\vec{v}_{\perp}|}{(\lambda D)^{1/2}} \quad , \tag{C6}$$

depending on their orientation with respect to $\vec{v}_{\perp}$; when p = 3.5, $w_\chi(\omega)$ is nearly constant for $\omega \leq \omega_c$. At frequencies $\omega >> \omega_c$ (smaller scattering structures), $w_\chi(\omega)$ generally decreases as ω^{1-p} when $\Phi_n(\vec{\kappa})$ obeys a power law (see equation 8 of Hinson and Tyler [1982]). The break frequency, ω_c, is often referred to as the Fresnel knee. Figure C2 shows $w_\chi(\omega)$ for scattering from isotropic irregularities; on a log-log plot, the high frequency asymptote is linear, with slope 1-p.

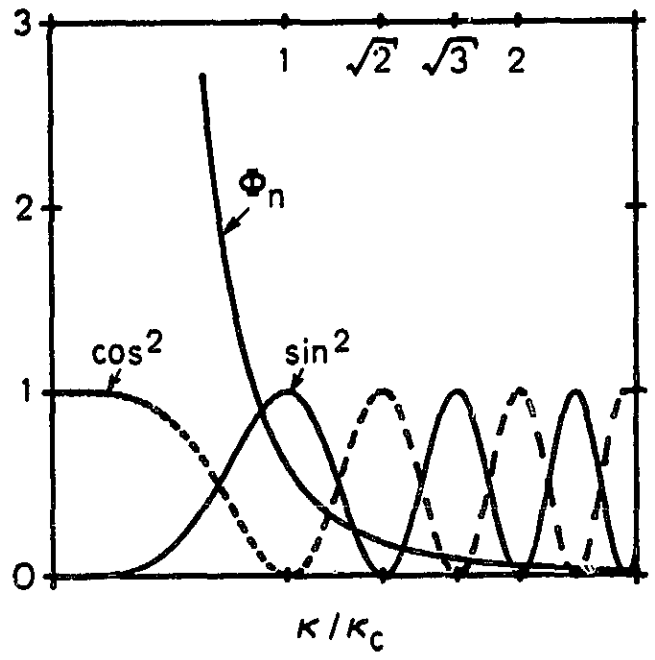

Figure C1 Functions that determine the efficiency of refractive irregularities for producing amplitude and phase fluctuations. The spectrum $\Phi_n(\vec{\kappa})$ specifies the strength of the irregularities with wave vector κ; here, $\Phi_n \propto \kappa^{-p}$, $p = 3.5$, and the irregularities are isotropic. The functions $\sin^2(\kappa^2 D/2k)$ and $\cos^2(\kappa^2 D/2k)$ represent the Fresnel filters for amplitude and phase, respectively. For a refractive structure with length scale $2\pi/\kappa$, the contribution to amplitude or phase fluctuations is proportional to the product of $\Phi_n(\vec{\kappa})$ and the appropriate Fresnel filter (see equation A27). The amplitude fluctuations arise primarily from irregularities within the "first pass band" of the Fresnel filter for amplitude, near $\kappa = \kappa_c \equiv \sqrt{2\pi/(\lambda D)}$. However, the Fresnel filter for phase has value unity for small κ. Hence, the principal fluctuations in signal phase are the result of scattering from the largest refractive structures present in the atmosphere.

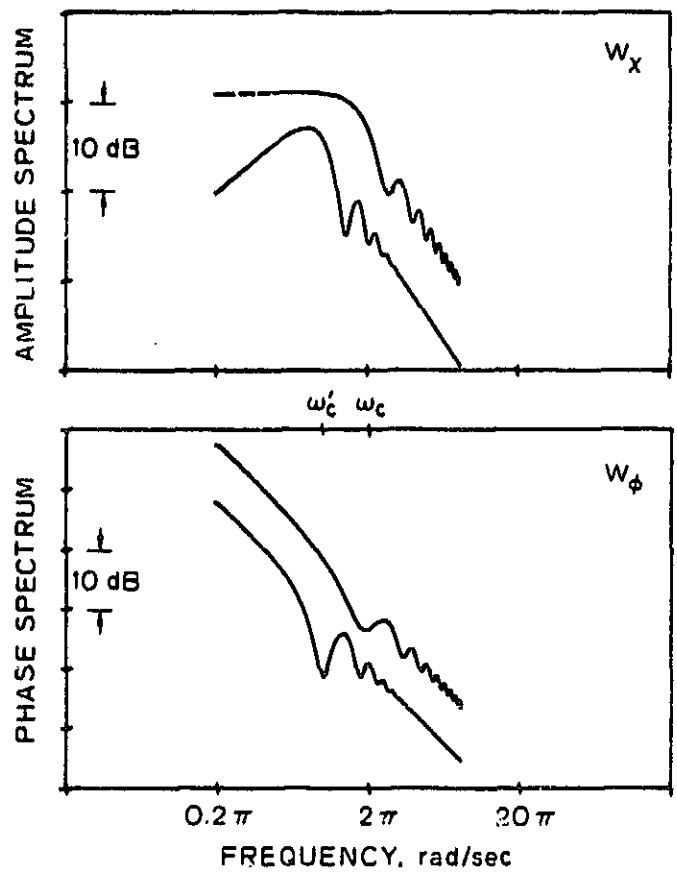

Figure C2 Theoretical amplitude (upper panel) and phase (lower panel) spectra for weak scattering by a power-law phase screen; all scales are logarithmic. These spectra were computed numerically using equations A36, A37, and 2.4. In each panel the upper curve applies when $\Phi_n(\vec{\kappa})$ is isotropic, while the lower curve corresponds to scattering by anisotropic irregularities with an axial ratio of 20:1. The two curves in each panel have been shifted vertically by 8 dB to accommodate comparison. In the isotropic case, the Fresnel knee in $w_\chi(\omega)$ occurs at frequency ω_c, below which the spectrum is nearly constant. For the case of highly anisotropic irregularities, the Fresnel knee is reduced in frequency to ω_c', and at lower frequencies the scintillations are suppressed relative to the isotropic case. Note that an increase in the axial ratio results in a shift in the frequency of the Fresnel fringes in both panels. For these calculations, $|\vec{v}_*| = 7.07$ km s^{-1}, $\gamma = 30°$, $A = 0°$, $p = 3.5$, and $(\lambda D)^{1/2} = 5$ km. From equations C6 and C7, $\omega_c = 2\pi$ and $\omega_c' = \pi$.

Next consider scattering from highly anisotroic irregularities (e >> f in equation 2.4). In this case, the phase screen has refractive variations in only one direction -- all wavevectors, $\vec{\kappa}$, in $\Phi_n(\vec{\kappa})$ are essentially parallel. Consequently, temporal amplitude fluctuations at the receiver result only from the component of raypath motion parallel to $\vec{\kappa}$. On the basis of the discussion above, a maximum in $w_\chi(\omega)$ due to Fresnel-zone-size structures occurs near frequency

$$\omega_c' \equiv \frac{\sqrt{2}\pi v_\star'}{(\lambda D)^{1/2}} \leq \omega_c \quad , \tag{C7}$$

where $v_\star'$ is the component of $\vec{v}_\star$ which is parallel to $\vec{\kappa}$. For magnetic-field-aligned irregularities at angle γ to the motion of the raypath, $v_\star' = |\vec{v}_\star| \cdot \sin\gamma$ (cf. Section 2.3.1 and Figure 2.1). Refractive irregularities that contribute to amplitude scintillations at frequencies less than ω_c' have dimension greater that $(\lambda D)^{1/2}$. Due to the Fresnel filter, structures of this size are not effective in producing amplitude fluctuations, so $w_\chi(\omega)$ is suppressed relative to the isotropic case for $\omega < \omega_c'$. At frequencies greater than ω_c', $w_\chi(\omega)$ again generally decreases in proportion to ω^{1-p}. The anisotropic spectrum also appears in Figure C2.

It is important to appreciate the difference between the amplitude spectra in Figure C2. In the isotropic case, the Fresnel knee occurs at a frequency ω_c, below which the spectrum is nearly constant (for p = 3.5). For the case of highly anisotropic irregularities, the Fresnel knee is shifted in frequency to ω_c', and at lower frequencies the scintillations are suppressed. The amplitude spectra therefore depend on the two-dimensional spatial structure of refractive variations in the

phase screen; this sensitivity can be explained physically. As demonstrated above, the Fresnel filter, which results from diffraction effects and experimental geometry, introduces a preferred length scale, $(\lambda D)^{1/2}$, for scattering structures. With a knowledge of the geometry, in particular $\vec{v}_*$ and D, and a measurement of the frequency of the Fresnel knee, ω_c', one can infer γ, the principal orientation of the irregularities in the anisotropic case (see equation C7). Occultation observations along a flyby trajectory thereby yield two-dimensional information concerning atmospheric spatial structure. Furthermore, as demonstrated by the curves in Figures C2 and C3, $w_\chi(\omega)$ is sensitive to the degree of anisotropy. Therefore, accurate measurements of the axial ratio do not require simultaneous observations using a spaced array of radio receivers, contrary to what some authors have claimed [see e.g., Woo and Yang, 1978].

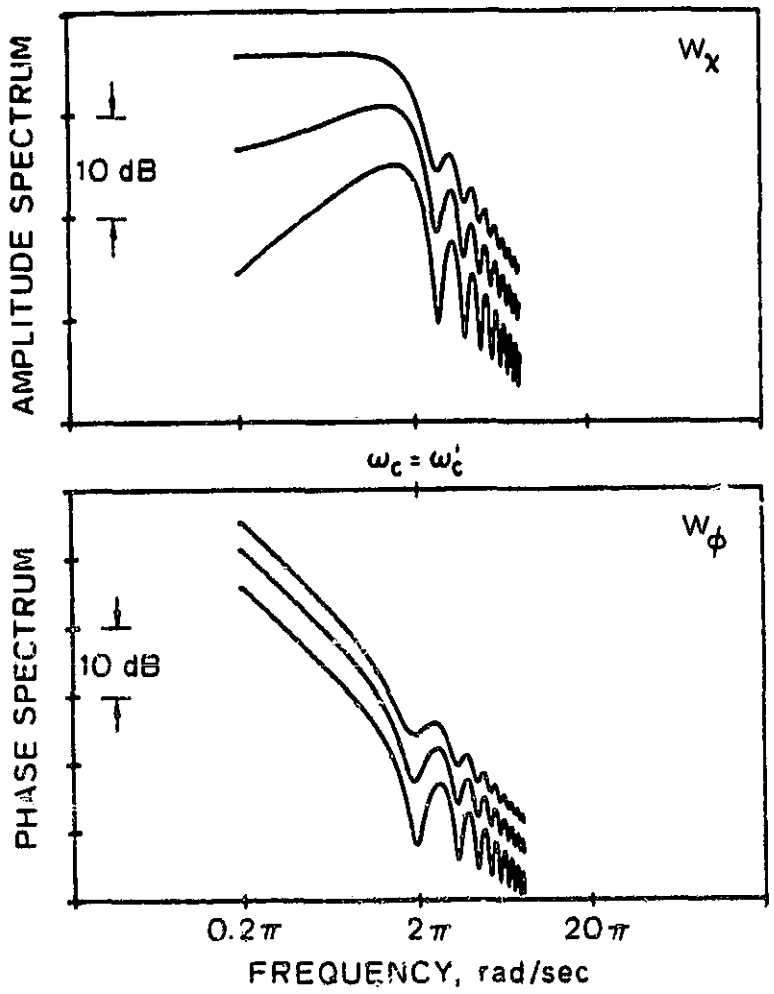

Figure C3 Theoretical amplitude (upper panel) and phase (lower panel) spectra for weak scattering by a power-law phase screen; all scales are logarithmic. These spectra were computed numerically using equations A36, A37, and 2.4. In each panel, the top curve applies when $\Phi_n(\vec{\kappa})$ is isotropic, the middle curve represents scattering by slightly anisotropic irregularities with an axial ratio of 1.7:1, and the bottom curve corresponds to an axial ratio of 3:1. Again, the curves have been shifted vertically by a few dB to accommodate comparison. Notice that an increase in the axial ratio enhances the Fresnel fringes at $\omega > \omega_c'$ and suppresses the amplitude scintillations for $\omega < \omega_c'$. For these calculations, $|\vec{v}_\perp| = 7.07$ km s^{-1}, $\gamma = 90°$, $\Lambda = 0°$, $p = 3.5$, and $(\lambda D)^{1/2} = 5$ km. In this case, $\omega_c = \omega_c' = 2\pi$ since $\gamma = 90°$ (see equations C6 and C7).

Oscillations, or "Fresnel fringes", occur at frequencies $\omega > \omega_c'$ in each of the spectra in Figures C2 and C3. A comparison of curves in Figure C3 shows that the Fresnel fringes are enhanced by anisotropic irregularities. Once again, this phenomenon can be explained on the basis of the arguments given above [cf. Briggs, 1975]. In the case of strong anisotropy, all wavevectors in $\Phi_n(\vec{\kappa})$ are nearly parallel. Therefore, all irregularities that satisfy $\omega = \vec{\kappa} \cdot \vec{v}_*$, and contribute to $w_\chi(\omega)$ at this frequency, have nearly the same magnitude and experience the same amount of Fresnel filtering. The amplitude Fresnel filter (see Figure C1) strongly modulates $w_\chi(\omega)$, producing local maxima at frequencies

$$\omega = (m)^{1/2}\omega_c' \quad , \tag{C8}$$

for m = 1, 3, 5, ..., with alternating deep nulls (m = 2, 4, 6, ...). For the case of isotropic irregularities, the situation is modified; there is a range of wavevectors with different magnitudes and orientations contributing to $w_\chi(\omega)$ at each ω. These various wavevectors experience different amounts of Fresnel filtering depending on their magnitudes. Consequently, in the summation of contributions at each ω, the effect of the Fresnel filter tends to be smoothed out; the resulting fringes are less pronounced than in the anisotropic case.

Similar considerations apply to interpretation of the theoretical phase spectrum, $w_\phi(\omega)$. As the Fresnel filter for phase has value unity for small κ (Figure C1), no Fresnel knee is present in $w_\phi(\omega)$. The spectrum generally decreases as ω^{1-p}, with Fresnel fringes similar to those in $w_\chi(\omega)$, but at offset frequencies. Theoretical results for $w_\phi(\omega)$ also appear in Figures C2 and C3.

To summarize the discussion above, the theoretical model for refractive irregularities in the ionosphere contains five free parameters (Section 2.3.1): (1) the inverse power-law exponent, p; (2) the axial ratio, e/f; (3) the orientation, γ; (4) the strength, Q; and (5) the wave vector corresponding to the outer scale, κ_0. As κ_0 did not influence any of the observations in Chapters 4, 5, and 7 (see Section 3.4), this parameter was not considered here. (The theoretical curves in Figures C2, C3, and C4 were calculated in the limit where $\kappa_0 \to 0$; this parameter then had a negligible effect on the shape of the spectra over the frequency range of interest). The remaining parameters affect the spectra as follows: the exponent, p, determines the slope (on a logarithmic plot) of the high-frequency portion both $W_\chi(\omega)$ and $W_\phi(\omega)$. For anisotropic irregularities, the orientation, γ, strongly determines the frequency of the Fresnel knee in $W_\chi(\omega)$, while the axial ratio, e/f, influences the shape of $W_\chi(\omega)$ at low frequencies. In addition, both e/f and γ affect the detailed structure of the Fresnel fringes. Finally, the factor Q scales both $W_\chi(\omega)$ and $W_\phi(\omega)$ for weak scattering, but does not change their shape on a logarithmic display.

As a direct consequence of these distinctive effects, the four principal parameters can be obtained from analysis of each measured amplitude or phase spectrum by following the procedure in Section 3.4. The strength of the determination depends on the values of the parameters themselves and the experimental conditions. Analysis of the solutions for p, γ, and Q shows that for the Voyager observations, these parameters were well determined in a physically meaningful sense. The parameter e/f is best determined from measurements at low frequencies

($\omega < \omega_c'$) which require long time segments of data. The relatively large uncertainties in e/f reported in Chapters 4, 5, and 7 are the result of the limited duration of the data from any one altitude region in the occulting planet's atmosphere.

The preceding discussion can be generalized to the case where the refractive background is inhomogeneous; the effects of the free parameters in $\Phi_n(\vec{\kappa})$ on the scintillation spectra are essentially unchanged.

C.4 The Cross Amplitude-Phase Spectrum

The cross spectrum, $W_{\chi\phi}(\omega)$, compares the magnitude and phase of correlated Fourier components in the amplitude and phase spectra of the received signal (see Sections A.2 and A.3). By the reasoning in Section C.2, at each frequency ω, $W_{\chi\phi}(\omega)$ consists of independent contributions from irregularities with wave vectors that satisfy $\vec{\kappa}\cdot\vec{v}_\perp = \omega$. The behavior of each contribution can be understood by considering the result in equation C4 for scattering from the cosinusoidal phase screen. In that case, fluctuations in amplitude and phase caused by spacecraft motion parallel to the screen are either in phase or shifted by π radians, as determined by the signs of the Fresnel filters, $\sin(\kappa^2 D/2k)$ and $\cos(\kappa^2 D/2k)$. The relative size of the fluctuations also depends on these two factors. Clearly, since the phase of each contribution to $W_{\chi\phi}(\omega)$ is 0 or π radians, $W_{\chi\phi}(\omega)$ is real for scattering from a statistically homogeneous medium.

Figure C4 shows the magnitude and phase of $W_{\chi\phi}(\omega)$, as calculated from equations A38 and 2.4. Fluctuations at low frequencies result from irregularities with large dimension (small $|\vec{\kappa}|$) so that $\sin(\kappa^2 D/2k)$ and

$\cos(\kappa^2 D/2k)$ are both positive and the cross spectrum phase is 0. At a higher frequency, there is an increased contribution from length scales where $\sin(\kappa^2 D/2k) > 0$, $\cos(\kappa^2 D/2k) < 0$, and the phase of $w_{\chi\phi}(\omega)$ changes abruptly to π. In this way, the phase is predicted to alternate between values of 0 and π, with shifts occurring at frequencies $\omega = (m)^{1/2}\omega_c'$ for integer values of m. Each shift in phase is accompanied by a null in the magnitude of $w_{\chi\phi}(\omega)$.

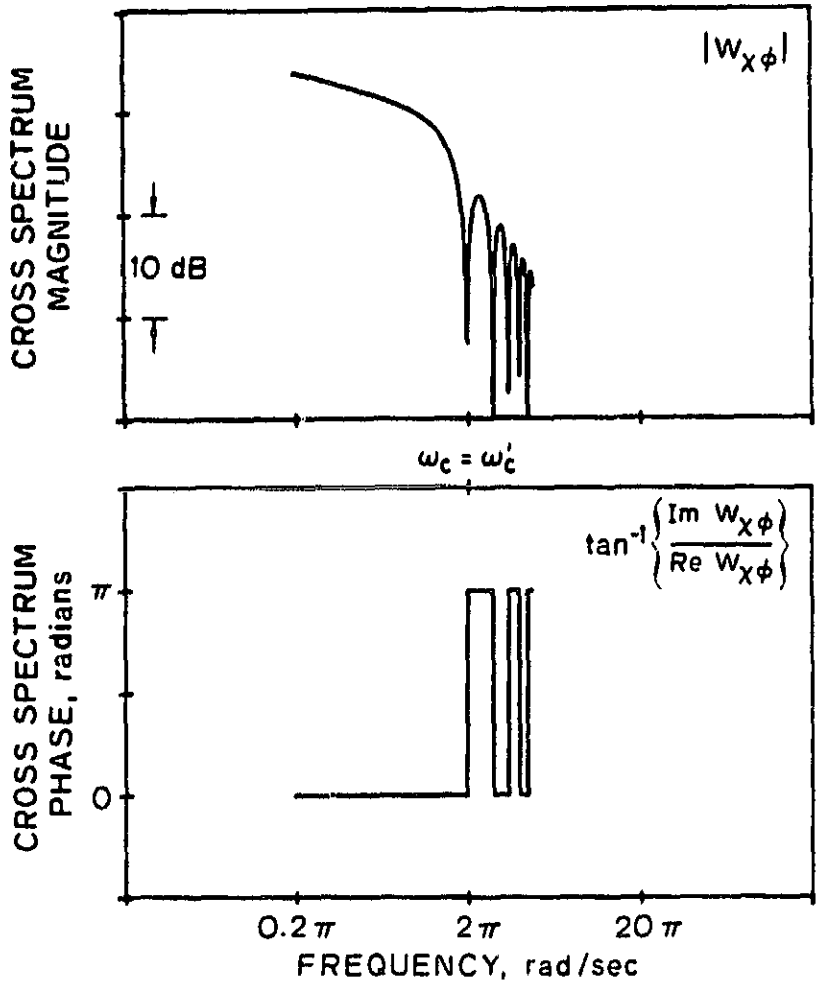

Figure C4 Theoretical magnitude (upper panel) and phase (lower panel) of the cross spectrum, $w_{\chi\phi}(\omega)$, for weak scattering by a power-law phase screen. These spectra were computed numerically from equations A38 and 2.4. The phase alternates between values of 0 and π, with abrupt shifts occurring at frequencies $\omega = (m)^{1/2}\omega_c'$ for integer values of m. Each shift in phase is accompanied by a null in the magnitude of $w_{\chi\phi}(\omega)$; the depth of the nulls varies as a result of discrete sampling. For these calculations, e/f = 10, $|\vec{v}_\star|$ = 7.07 km s^{-1}, $\gamma = 90°$, $\Lambda = 0°$, p = 3.5, $(\lambda D)^{1/2}$ = 5 km, and $\omega_c = \omega_c' = 2\pi$.

APPENDIX D

THE EFFECT OF THE QUIESCENT ATMOSPHERE DURING PLANETARY RADIO OCCULTATIONS

The effect of the quiescent atmosphere during planetary radio occultations has been discussed at length in the literature (for example, see Haugstad [1982]); this appendix summarizes the results and defines parameters. Additional references on this subject include Fjeldbo and Eshleman [1969], Young [1976], Haugstad [1978a, 1978c, 1982], Hubbard et al. [1978], Eshleman et al. [1979a], and Woo et al. [1980b].

Figure D1 represents the idealized occultation geometry and shows the coordinate system. A monochromatic plane wave propagating in the x-direction impinges on a planetary atmosphere which is free of small-scale irregularities such as turbulence, waves, or layers. The refractive index in the atmosphere is given by $1 + n_0(r)$. After refraction by angle α, where $\alpha \ll 1$, the geometrical optics ray which intercepts the spacecraft has fractional intensity $\phi_y\phi_z$, where the two factors account for focusing due to limb curvature and defocusing due to the vertical gradient in $n_0(r)$, respectively. For a spherically symmetrical, isothermal atmosphere with scale height H,

$$\phi_y = \left(1 - \frac{\alpha D}{r}\right)^{-1} \quad \text{and} \quad \phi_z = \left(1 + \frac{\alpha D}{H}\right)^{-1} \quad . \tag{D1}$$

Here, D is the distance from spacecraft to planet, and r is the altitude of the raypath at periapsis.

As a second consequence of differential refraction, the transverse raypath velocity in the phase screen is given by

$$\vec{v}_* = \phi_y v_y \hat{y} + \phi_z v_z \hat{z} \quad , \tag{D2}$$

where v_y and v_z are components of spacecraft velocity that are perpendicular to the direction of propagation, and $\hat{y}$ and $\hat{z}$ are the horizontal and vertical coordinate unit vectors at ray periapsis.

Finally, the quiescent atmosphere distorts the Fresnel zone at wavelength λ to horizontal and vertical dimensions $(\phi_y \lambda D)^{1/2}$ and $(\phi_z \lambda D)^{1/2}$, respectively.

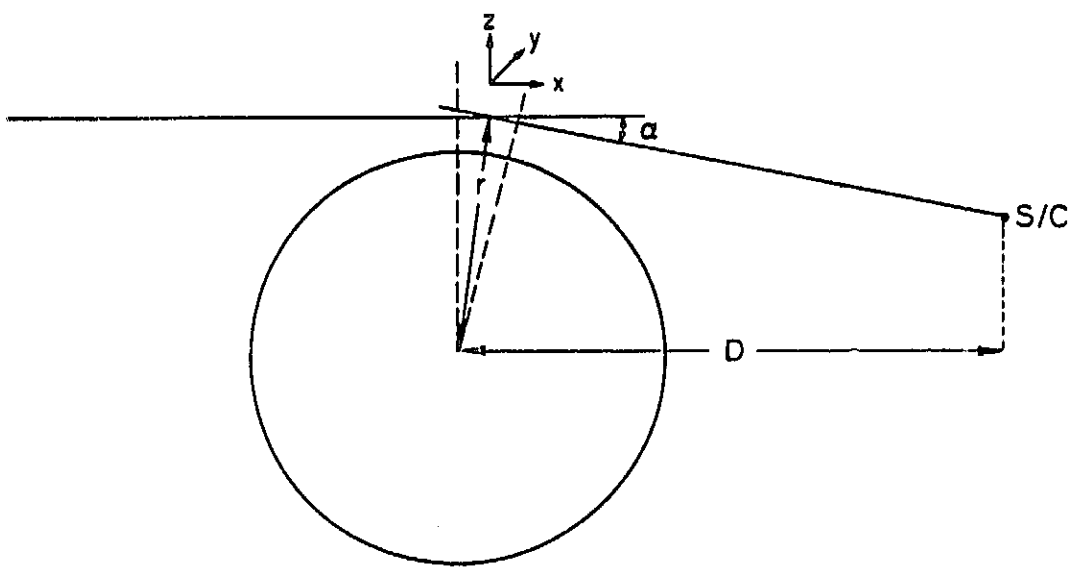

Figure D1 Idealized occultation geometry and coordinate system. A radio signal transmitted from earth (located at $x \approx -\infty$) undergoes refraction by angle α in the occulting planet's atmosphere and is received subsequently by the spacecraft. A distance D separates the spacecraft and planet; the parameter r gives the altitude of the raypath at periapsis. As viewed from earth, the y- and z-directions are tangent and perpendicular, respectively, to the visible limb of the planet.

APPENDIX E

THE VALIDITY OF THE MEASUREMENT UNCERTAINTIES

The results reported in Chapters 4 and 5 consist of solutions for four parameters that characterize the refractive irregularities in the ionospheres of Jupiter and Saturn. From Chapter 6 it is clear that realistic uncertainties are essential for interpreting these parameter measurements. In this appendix, the uncertainty in γ, the inferred magnetic field orientation (see Chapter 6), is shown to be realistic with respect to statistical errors and not simply formal. As the uncertainties in all four parameters were calculated by the same procedure (Section 3.4), this suggests, by implication, that the uncertainties in the remaining parameters are also reliable.

The conclusions in this appendix do not apply to systematic errors, which are more difficult to assess. One such error in γ arises from uncertainty in the spacecraft trajectory. This effect was considered, but was found to be insignificant for the occultations of Voyager by Jupiter and Saturn. As mentioned previously, a bias in γ due to the spatially varying field geometry in Jupiter's ionosphere could be comparable to the statistical errors; however, this source of error was taken into account in evaluating the Jovian magnetic field models (Section 6.3). The analagous effect at Saturn is believed to be negligible relative to the statistical uncertainties (Section 6.4).

Validity of the Measurement Uncertainties

The 13-cm amplitude spectrum measured in region 2 during V2 emersion at Saturn (see Figures 5.4 and 5.5) is used as an example in the first part of this discussion. In order to demonstrate the sensitivity of the amplitude spectrum to changes in γ, three theoretical spectra are shown in Figure E1. One curve ($\gamma = 46°$) corresponds to the least-squares solution for parameters derived from this measured spectrum (see Table 5.3); this same theoretical spectrum also appeared in the panel at the lower left of Figure 5.5. The other two curves illustrate the effect of changing γ by $\pm 3\sigma$, or 9° (see Table 5.3), from the best fit. Note that a shift of 3σ in either direction significantly alters the alignment of the theoretical spectrum, a phenomenon which was explained in Appendix C.

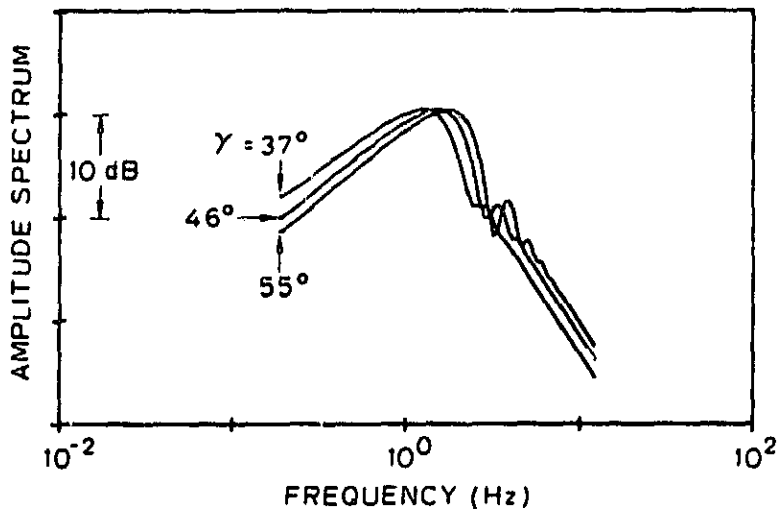

Figure E1 Theoretical 13-cm amplitude spectra for weak scattering by a power-law phase screen. The spectra were computed numerically as described in Section 3.4. One curve ($\gamma = 46°$) corresponds to the least-squares solution for parameters derived from the 13-cm amplitude spectrum in region 2 during V2 emersion at Saturn (see Figures 5.4 and 5.5); this same theoretical spectrum also appeared in the panel at the lower left of Figure 5.5. The other two curves illustrate the effect of changing γ by $\pm 3\sigma$, or 9° (see Table 5.3), from the best fit. Note that a shift of 3σ in either direction significantly alters the alignment of the theoretical spectrum, as explained in Appendix C. For these calculations, $e/f = 7$, $|\vec{v}_\star| = 20.6$ km s^{-1}, $p = 3.6$, and $(\lambda D)^{1/2} = 5.21$ km, where λ is the radio wavelength.

Validity of the Measurement Uncertainties

In Figure E2, three theoretical curves are compared to the measured amplitude spectrum. For these fits, the angle γ was assigned a fixed value (37°, 46°, or 55°, as in Figure E1) and the three parameters p, e/f, and Q (see Section 2.3.1 for definitions) were adjusted in order to minimize the residual, as defined in equation 3.5. The residual attains its overall minimum value when $\gamma = 46°$, as reported in Chapter 5 (see Figure 5.5 and Table 5.3). A change in γ by $\pm 3\sigma$ away from the least-squares solution visibly reduces the quality of the fit in the frequency interval from 1 to 4 Hz. (The solutions for p, e/f, and Q for each choice of γ remained within 1σ of the values listed in Table 5.3.)

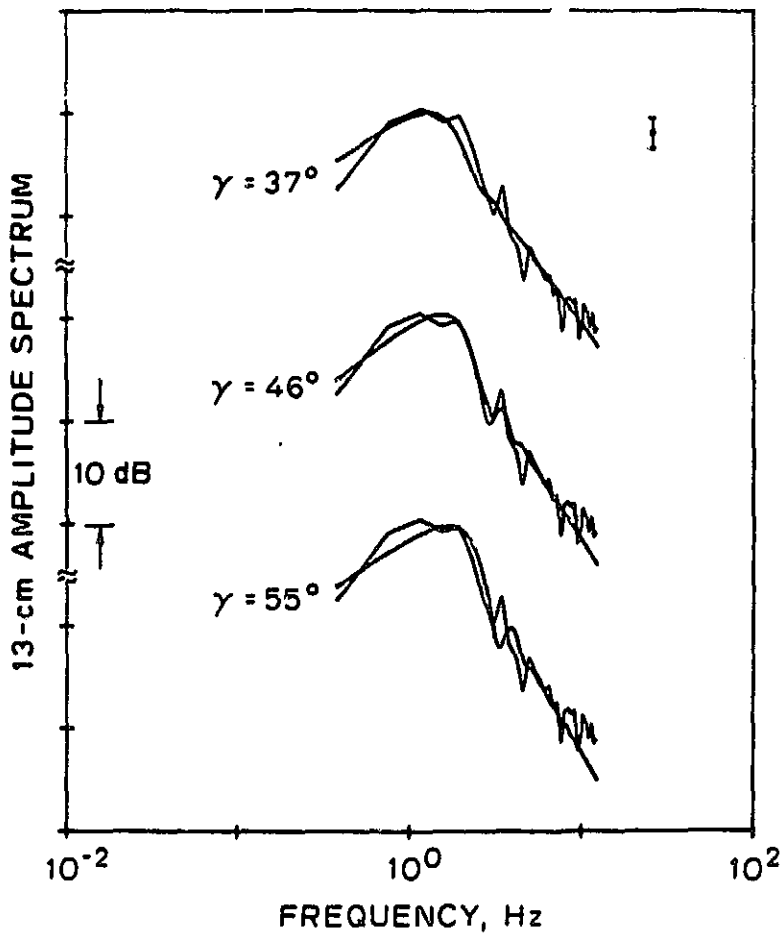

Figure E2 Comparison of three theoretical curves to the 13-cm amplitude spectrum measured in region 2 during V2 emersion at Saturn. For these fits, the angle γ was assigned a fixed value (37°, 46°, or 55°) and the other three parameters in the theory (p, e/f, and Q) were adjusted in order to minimize the residual. The overall minimum value of the residual occurs when γ = 46°, as reported in Chapter 5. A change in γ by $\pm 3\sigma$ away from the least-squares solution visibly reduces the quality of the fit in the frequency interval from 1 to 4 Hz.

The residual of the theoretical fit to the measured amplitude spectrum was calculated as a function of γ (by varying p, e/f, and Q) for values intermediate to those shown in Figure E2. The results appear as curve 1 in Figure E3; the angle γ has been converted to Γ (see Figure 6.1) for comparison with the predictions of magnetic field models. The residuals of curve 1 at Γ = 217°, 226°, and 235° correspond to the three fits in Figure E2; the well-defined minimum at Γ = 226° indicates the least-squares solution for this parameter. When Γ is shifted by $\pm 3\sigma$ away from the minimum, the residual increases by more than 70%. The results in Figures E2 and E3 demonstrate that the occultation measurements are sensitive to changes of 3σ in the magnetic field direction, and confirm the uncertainty in γ.

Figure E3 also shows plots of the residual as a function of Γ for the 13-cm phase spectrum from region 2 (curve 2) and the 3.6-cm amplitude spectrum from region 3 (curve 3) of V2 emersion at Saturn (see Figures 5.4 and 5.5). The corresponding curves derived from the two spectra measured during V1 immersion at Saturn (see Figures 5.2 and 5.3) appear in Figure E4. The similarities among all five curves suggest that the amplitude spectrum discussed above is typical of the Voyager occultation measurements.

For comparison, Figures E3 and E4 also indicate the values of Γ predicted by the OD and Z3 magnetic field models (see Section 6.4). The minimum of the residual in each of the five curves is intermediate to the model predictions, as discussed in Chapter 6.

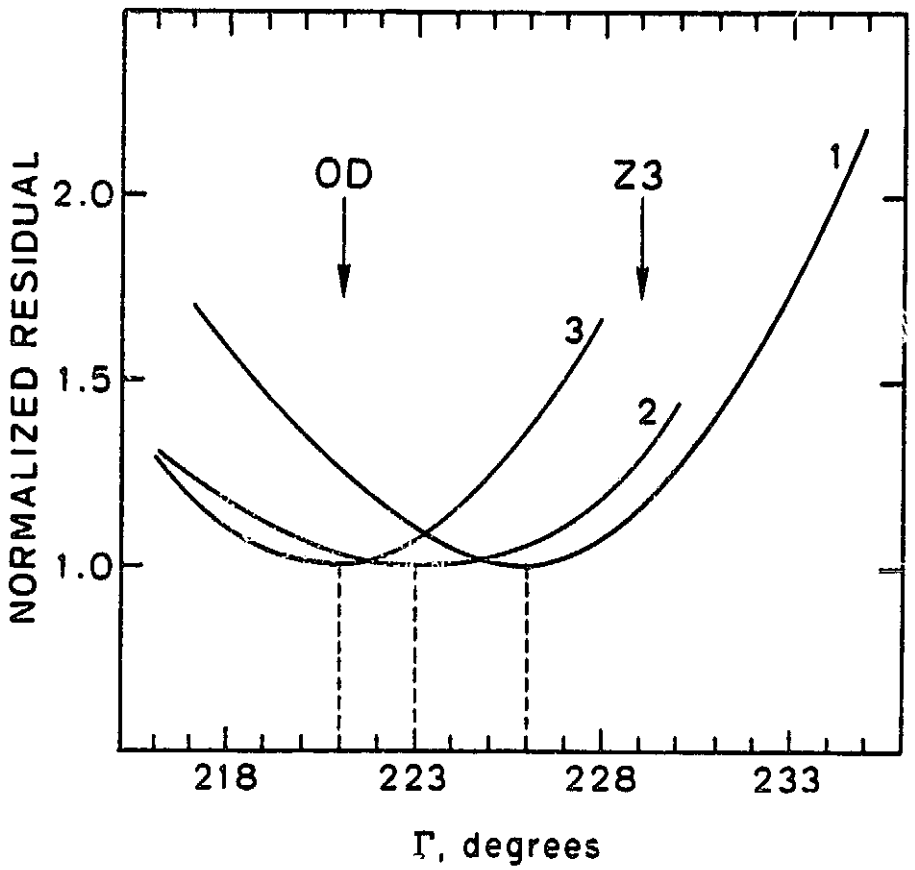

Figure E3 Normalized residual as a function of Γ. Curve 1 was derived from the 13-cm amplitude spectrum from region 2 of V2 emersion at Saturn (see Figures 5.4 and 5.5). To calculate one point in the curve, Γ (or equivalently γ) was assigned a fixed value and the other theoretical parameters (p, e/f, and Q) were adjusted in order to minimize the residual. The values at Γ = 217°, 226°, and 235° correspond to the three fits in Figure E2; the minimum at 226° indicates the least-squares solution for this parameter. When Γ is shifted by ±3σ away from the minimum, the residual increases by more than 70%. The curves corresponding to the 13-cm phase spectrum from region 2 (curve 2) and the 3.6-cm amplitude spectrum from region 3 (curve 3) of V2 emersion at Saturn are also shown, along with the angles predicted by the OD and Z3 magnetic field models.

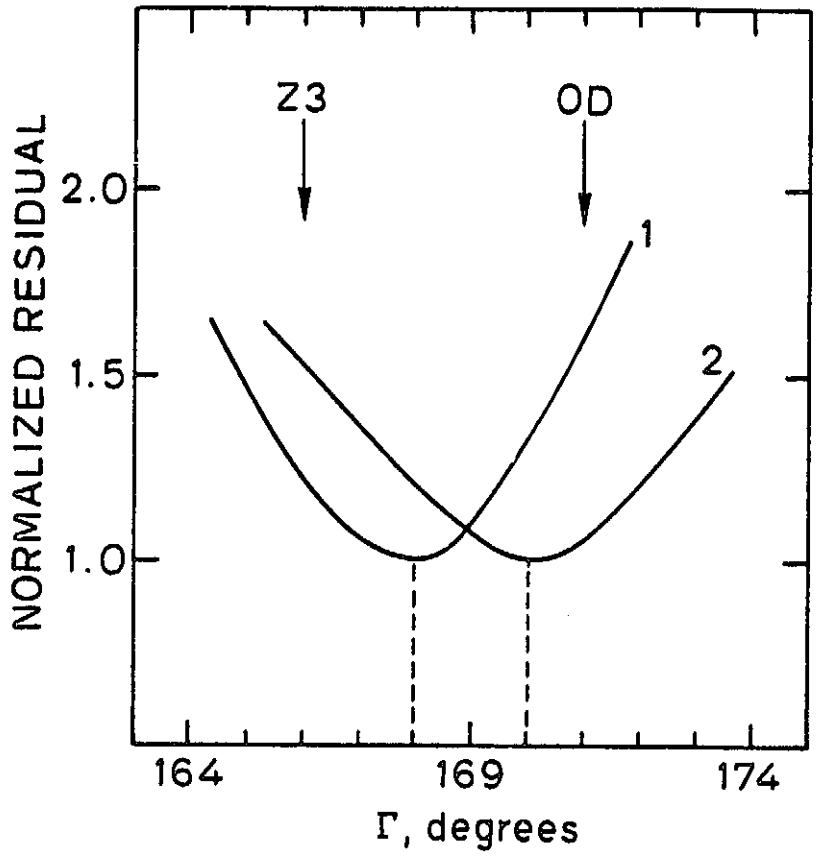

Figure E4 Normalized residual as a function of Γ for the 13-cm amplitude spectra measured in regions 1 and 2 of V1 immersion at Saturn. See Figure E3 for additional comments.

Validity of the Measurement Uncertainties

An empirical test of the uncertainties comes from the measurements of γ in Tables 4.2-4.4 and 5.2-5.3. These solutions for γ were obtained either from non-overlapping time segments of data, from phase and amplitude spectra measured over the same interval, or from measurements at different radio wavelengths, so that all the measurements at any one location are based on different data sets. As the magnetic field orientation at Jupiter or Saturn is not expected to vary appreciably with altitude over the ionospheric region of the observations, these measurements should be mutually consistent at any one location. Of the 19 measurements of γ at Jupiter and Saturn, 16 are within 1σ and all are within 2.5σ of the average value of γ at their respective locations. This result supports the accuracy of the uncertainties.

REFERENCES

Acuna, M. H., J. Connerney, and N. F. Ness (1982). Implications/ applications of the Z3 model magnetic field of Saturn, Conference presentation SM22A-02, EOS, 63, 1068.

Acuna, M. H., and N. F. Ness (1976). The main magnetic field of Jupiter, J. Geophys. Res., 81, 2917-2922.

Acuna, M. H., and N. F. Ness (1980). The magnetic field of Saturn: Pioneer 11 observations, Science, 207, 444-446.

Acuna, M. H., N. F. Ness, and J. Connerney (1980). The magnetic field of Saturn: Further studies of the Pioneer 11 observations, J. Geophys. Res., 85, 5675-5678.

Boischot, A., A. Lecacheux, M. L. Kaiser, M. D. Desch, J. K. Alexander, and J. W. Warwick (1981). Radio Jupiter after Voyager: An overview of the planetary radio astronomy observations, J. Geophys. Res., 86, 8213-8226.

Booker, H. G., J. A. Ratcliffe, and D. H. Shinn (1950). Diffraction from an irregular screen with applications to ionospheric problems, Phil. Trans. Roy. Soc. London, Ser. A, 242, 579-607.

Booker, H. G. (1979). The role of acoustic gravity waves in the generation of spread-F and ionospheric scintillation, J. Atmos. Terr. Phys., 41, 501-515.

Bramley, E. N. (1954). The diffraction of waves by an irregular refracting medium, Proc. Roy. Soc. London, Ser. A, 225, 515-518.

Bramley, E. N. (1977). The accuracy of computing ionospheric radio-wave scintillation by the thin-phase-screen approximation, J. Atmos. Terr. Phys., 39, 367-373.

Brandt, S. (1970). Statistical and Computational Methods in Data Analysis, North-Holland, Amsterdam.

Bretherton, F. P. (1969a). Momentum transport by gravity waves, Quart. J. R. Meteorol. Soc., 95, 213-243.

Bretherton, F. P. (1969b). Waves and turbulence in stably stratified fluids, Radio Sci., 4, 1279-1287.

Briggs, B. H. (1975). Ionospheric irregularities and radio scintillations, Contemp. Phys., 16, 469-488.

Broadfoot, A. L., M. J. S. Belton, P. Z. Takacs, and B. R. Sandel (1979). Extreme ultraviolet observations from Voyager 1 encounter with Jupiter, Science, 204, 979-982.

Brown, W. P. (1966). Validity of the Rytov approximation in optical propagation calculations, J. Opt. Soc. Amer., 56, 1045-1052.

Cadet, D., and H. Teitelbaum (1979). Observational evidence of internal inertia-gravity waves in the tropical stratosphere, J. Atmos. Sci., 36, 892-907.

Chenette, D. L., and L. Davis, Jr. (1982). An analysis of the structure of Saturn's magnetic field using charged particle absorption signatures, J. Geophys. Res., 87, 5267-5274.

Connerney, J. (1981). The magnetic field of Jupiter: A generalized inverse approach, J. Geophys. Res., 86, 7679-7693.

Connerney, J., N. F. Ness, and M. H. Acuna (1982). Zonal harmonic model of Saturn's magnetic field from Voyager 1 and 2 observations, Nature, 298, 44-46.

Crane, R. K. (1980). A review of radar observations of turbulence in the lower stratosphere, Radio Sci., 15, 177-193.

Davies, M. E., V. K. Abalakin, C. A. Cross, R. L. Duncombe, H. Masursky, B. Morando, T. C. Owen, P. K. Seidelmann, A. T. Sinclair, G. A. Wilkins, and Y. S. Tjuflin (1980). Report of the IAU working group on cartographic coordinates and rotational elements of the planets and satellites, Celestial Mech., 22, 205-230.

Desch, M. D., and M. L. Kaiser (1981). Voyager measurement of the rotation period of Saturn's magnetic field, Geophys. Res. Lett., 8, 253-256.

Dewan, E. M. (1979). Stratospheric wave spectra resembling turbulence, Science, 204, 832-835.

Dyer, J. W. (1980). Pioneer Saturn, Science, 207, 400-401.

Dyson, P. L., J. P. McClure, and W. B. Hanson (1974). In situ measurements of the spectral characteristics of F region ionospheric irregularities, J. Geophys. Res., 79, 1497-1502.

Einaudi, F., D. P. Lalas, and G. E. Perona (1978/79). The role of gravity waves in tropospheric processes, Pure Appl. Geophys., 117, 627-663.

Elliot, J. L. (1979). Stellar occultation studies of the solar system, Ann. Rev. Astron. Astrophys., 17, 445-475.

Eshleman, V. R. (1973). The radio occultation method for the study of planetary atmospheres, Planet. Space Sci., 21, 1521-1531.

Eshleman, V. R., G. L. Tyler, J. D. Anderson, G. Fjeldbo, G. S. Levy, G. E. Wood, and T. A. Croft (1977). Radio science investigations with Voyager, Space Sci. Rev., 21, 207-232.

Eshleman, V. R., G. L. Tyler, and W. T. Freeman (1979a). Deep radio occultations and "evolute flashes"; Their characteristics and utility for planetary studies, Icarus, 37, 612-626.

Eshleman, V. R., G. L. Tyler, G. E. Wood, G. F. Lindal, J. D. Anderson, G. S. Levy, and T. A. Croft (1979b). Radio science with Voyager 1 at Jupiter: Preliminary profiles of the atmosphere and ionosphere, Science, 204, 976-978.

Eshleman, V. R., G. L. Tyler, G. E. Wood, G. F. Lindal, J. D. Anderson, G. S. Levy, and T. A. Croft (1979c). Radio science with Voyager at Jupiter: Initial Voyager 2 results and a Voyager 1 measure of the Io torus, Science, 206, 959-962.

Eshleman, V. R., G. F. Lindal, and G. L. Tyler (1983). Is Titan wet or dry?, Science, 221, 53-55.

Essen, L., and K. D. Froome (1951). The refractive indices and dielectric constants of air and its principal constituents at 24000 Mc/s, Proc. Phys. Soc. London, B64, 862-875.

Fante, R. L. (1975). Electromagnetic beam porpagation in turbulent media, Proc. IEEE, 63, 1669-1692.

Fejer, A. J. (1953). The diffraction of waves in passing through an irregular refracting medium, Proc. Roy. Soc. London, Ser. A, 220, 455-471.

Fjeldbo, G. (1964). Bistatic-radar methods for studying planetary ionospheres and surfaces, Ph. D. thesis, Stanford Univ.

Fjeldbo, G., and V. R. Eshleman (1969). Atmosphere of Venus as studied with Mariner 5 dual radio-frequency occultation experiment, Radio Sci., 4, 879-897.

Fjeldbo, G., A. Kliore, B. Seidel, D. Sweetnam, and P. Woiceshyn (1976). The Pioneer 11 radio occultation measurements of the Jovian ionosphere, in Jupiter (T. Gehrels, editor), pp. 238-246, Univ. of Arizona Press, Tucson.

Flasar, F. M., R. E. Samuelson, and B. J. Conrath (1981). Titan's atmosphere: Temperature and dynamics, Nature, 292, 693-698.

Flatte, S. M., (Ed.) (1979). Sound Transmission Through a Fluctuating Ocean, Cambridge Univ. Press, Cambridge.

French, R. G., and P. J. Gierasch (1974). Waves in the Jovian Upper Atmosphere, J. Atmos. Sci., 31, 1707-1712.

French, R. G., J. L. Elliot, E. W. Dunham, D. A. Allen, J. H. Elias, J. A. Frogel, and W. Liller (1983). The thermal structure and energy balance of the Uranian upper atmosphere, Icarus, 53, 399-414.

Gage, K. S., and B. B. Balsley (1980). On the scattering and reflection mechanisms contributing to clear air radar echoes from the troposphere, stratosphere, and mesosphere, Radio Sci., 15, 243-257.

Gehrels, T. (Ed.) (1976). Jupiter, Univ. of Arizona Press, Tucson.

Gossard, E. E., and W. H. Hooke (1975). Waves in the Atmosphere, Elsevier, Amsterdam.

Green, J. L., and K. S. Gage (1980). Observations of stable layers in the troposphere and stratosphere using VHF radar, Radio Sci., 15, 395-405.

Hall, C. F. (1975). Pioneer 10 and Pioneer 11, Science, 188, 445-446.

Hanel, R., B. Conrath, F. M. Flasar, V. Kunde, W. Maguire, J. Pearl, J. Pirraglia, R. Samuelson, L. Herath, M. Allison, D. Cruikshank, D. Gautier, P. Gierasch, L. Horn, R. Koppany, and C. Ponnamperuma (1981). Infrared observation of the Saturnian system from Voyager 1, Science, 212, 192-200.

Harper, R. M., and W. E. Gordon (1980). A review of radar studies of the middle atmosphere, Radio Sci., 15, 195-211.

Haugstad, B. S. (1978a). Effects of the inhomogeneous background on radiation propagating through turbulent planetary atmospheres, Radio Sci., 13, 435-440.

Haugstad, B. S. (1978b). Turbulence in planetary occultations: I. A theoretical formulation, Icarus, 35, 121-138.

Haugstad, B. S. (1978c). Turbulence in planetary occultations: III. Effects on atmospheric profiles derived from intensity measurements, Icarus, 35, 422-435.

Haugstad, B. S. (1979). Turbulence in planetary occultations: IV. Power spectra of phase and intensity fluctuations, Icarus, 37, 322-335.

Haugstad, B. S. (1982). Turbulence in planetary occultations: A strong scattering formulation including an inhomogeneous background, Radio Sci., 17, 565-573.

Hewish, A. (1951). The diffraction of radio waves in passing through a phase-changing ionosphere, Proc. Roy. Soc. London, Ser. A, 209, 81-96.

Hide, R., and S. Malin (1979). The size of Jupiter's electrically conducting fluid core, Nature, 280, 42-43.

Hines, C. O. (1960). Internal atmospheric gravity waves at ionospheric heights, Can. J. Phys., 38, 1441-1481.

Hinson, D. P., and G. L. Tyler (1982). Spatial irregularities in Jupiter's upper ionosphere observed by Voyager radio occultations, J. Geophys. Res., 87, 5275-5289.

Hinson, D. P., and G. L. Tyler (1983). Internal gravity waves in Titan's atmosphere observed by Voyager radio occultation, Icarus, 54, 337-352.

Hinson, D. P. (1983). Magnetic field orientations in Saturn's upper ionosphere inferred from Voyager radio occultations, J. Geophys. Res., in press.

Holton, J. R., and R. S. Lindzen (1972). An updated theory for the quasi-biennial cycle of the tropical stratosphere, J. Atmos. Sci., 29, 1076-1080.

Hubbard, W. B., J. R. Jokipii, and B. A. Wilking (1978). Stellar occltations by turbulent planetary atmospheres: A wave-optical theory including a finite scale height, Icarus, 34, 374-395.

Hunt, J. L., J. D. Poll, D. Goorvitch, and R. H. Tipping (1983). Collision-induced absorption in the far infrared spectrum of Titan, Icarus, 55, 63-72.

Jenkins, G. M., and D. G. Watts (1968). Spectral Analysis and its Applications, Holden-Day, San Francisco.

Jordan, E. C., and K. G. Balmain (1968). Electromagnetic Waves and Radiating Systems, Prentice-Hall, Englewood Cliffs, N. J.

Kaiser, M. L., M. D. Desch, J. W. Warwick, and J. B. Pearce (1980). Voyager detection of nonthermal radio emission from Saturn, Science, 209, 1238-1240.

Kaiser, M. L., M. D. Desch, and A. Lecacheux (1981). Saturnian kilometric radiation: Statistical properties and beam geometry, Nature, 292, 731-733.

Kliore, A. J., and P. M. Woiceshyn (1976). Structure of the atmosphere of Jupiter from Pioneer 10 and 11 radio occultation measurements, in Jupiter (T. Gehrels, editor), pp. 216-237, Univ. of Arizona Press, Tucson.

Kohlhase, C. E., and P. A. Penzo (1977). Voyager Mission Description, Space Sci. Rev., 21, 77-101.

Kunde, V. G., A. C. Aikin, R. A. Hanel, D. E. Jennings, W. C. Maguire, and R. E. Samuelson (1981). C_4H_2, HC_3N and C_2N_2 in Titan's atmosphere, Nature, 292, 686-688.

Langel, R. A., R. H. Estes, G. D. Mead, E. B. Fabiano, and E. R. Lancaster (1980). Initial geomagnetic field model from Magsat vector data, Geophys. Res. Lett., 7, 793-796.

Lee, R., and J. Harp (1969). Weak scattering in random media, with applications to remote probing,, Proc. IEEE, 57, 375-406.

Lindal, G. F., G. E. Wood, G. S. Levy, J. D. Anderson, D. N. Sweetman, H. B. Hotz, B. J. Buckles, D. P. Holmes, P. E. Doms, V. R. Eshleman, G. L. Tyler, and T. A. Croft (1981). The atmosphere of Jupiter: An analysis of the Voyager radio occultation measurements, J. Geophys. Res., 86, 8721-8727.

Lindal, G. F., G. E. Wood, H. B. Hotz, D. N. Sweetnam, V. R. Eshleman, and G. L. Tyler (1983). The atmosphere of Titan: An analysis of the Voyager 1 radio occultation measurements, Icarus, 53, 348-363.

Lindzen, R. S., and J. R. Holton (1968). A theory of the quasi-biennial oscillation, J. Atmos. Sci., 25, 1095-1107.

Lipa, B., and G. L. Tyler (1979). Statistical and computational uncertainties in atmospheric profiles from radio occultation: Mariner 10 at Venus, Icarus, 39, 192-208.

MacDougall, J. W. (1981). Distributions of irregularities which produce ionospheric scintillations, J. Atmos. Terr. Phys., 43, 317-325.

Maguire, W. C., R. A. Hanel, D. E. Jennings, V. G. Kunde, and R. E. Samuelson (1981). C_3H_8 and C_3H_4 in Titan's atmosphere, Nature, 292, 683-686.

Marians, M. (1975). Computed scintillation spectra for strong turbulence, Radio Science, 10, 115-119.

Mason, B. J. (1971). The Physics of Clouds, Oxford Univ. Press (Clarendon), London/New York.

Nagpal, O. P. (1979). The sources of atmospheric gravity waves, Contemp. Phys., 20, 593-609.

Northrup, T. G., A. G. Opp, and J. H. Wolfe (1980). Pioneer 11 Saturn encounter, J. Geophys. Res., 85, 5651-5653.

Northrup, T. G., and J. R. Hill (1983). The inner edge of Saturn's B ring, J. Geophys. Res., 88, 6102-6108.

Opp, A. G. (1980). Scientific results from the Pioneer Saturn encounter: Summary, Science, 207, 401-403.

Phelps, A. D. R., and R. C. Sagalyn (1976). Plasma density irregularities in the high-latitude top side ionosphere, J. Geophys. Res., 81, 515-523.

Ratcliffe, J. A. (1956). Some aspects of diffraction theory and their application to the ionosphere, Reps. Prog. Phys., 19, 188-267.

Rino, C. L., and E. J. Fremouw (1977). The angle dependence of singly scattered wavefields, J. Atmos. Terr. Phys., 39, 859-868.

Rino, C. L. (1980). Numerical computations for a one-dimensional power law phase screen, Radio Science, 15, 41-47.

Rottger, J. (1980). Reflection and scattering of VHF radar signals from atmospheric refractivity structures, Radio Sci., 15, 259-276.

Rufenach, C. L. (1972). Power-law wavenumber spectrum deduced from ionospheric scintillation observations, J. Geophys. Res., 77, 4761-4772.

Rufenach, C. L. (1974). Wavelength dependence of radio scintillation: Ionosphere and interplanetary irregularities, J. Geophys. Res., 79, 1562-1566.

Rumsey, V. H. (1975). Scintillations due to a concentrated layer with a power-law turbulence spectrum, Radio Science, 10, 107-114.

Salpeter, E. E. (1967). Interplanetary scintillations: I. Theory, Astrophys. J., 147, 433-448.

Samuelson, R. E., R. A. Hanel, V. J. Kunde, and W. C. Maguire (1981). Mean molecular weight and hydrogen abundance of Titan's atmosphere, Nature, 292, 688-693.

Samuelson, R. E. (1983). Radiative equilibrium model of Titan's atmosphere, Icarus, 53, 364-387.

Seidelmann, P. K., and N. Divine (1977). Evaluation of Jupiter longitudes in System III (1965), Geophys. Res. Lett., 4, 65-68.

Singleton, D. G. (1970a). Dependence of satellite scintillations on zenith angle and azimuth, J. Atmos. Terr. Phys., 32, 789-803.

Singleton, D. G. (1970b). Saturation and focusing effects in radio-star and satellite scintillations, J. Atmos. Terr. Phys., 32, 187-208.

Smith, E. J., L. Davis, Jr., and D. E. Jones (1976). Jupiter's magnetic field and magnetosphere, in Jupiter, (T. Gehrels, editor), pp. 788-829, Univ. of Arizona Press, Tucson.

Smith, E. J., and S. Gulkis (1979). The magnetic field of Jupiter: A comparison of radio astronomy and spacecraft observations, Ann. Rev. Earth Planet. Sci., 7, 385-415.

Smith, E. J., L. Davis, Jr., D. E. Jones, P. J. Coleman, Jr., D. S. Colburn, P. Dyal, and C. P. Sonett (1980a). Saturn's magnetic field and magnetosphere, Science, 207, 407-410.

Smith, E. J., L. Davis, Jr., D. E. Jones, P. J. Coleman, Jr., D. S. Colburn, P. Dyal, and C. P. Sonett (1980b). Saturn's magnetosphere and its interaction with the solar wind, J. Geophys. Res., 85, 5655-5674.

Spencer, M. (1955). The shape of irregularities in the upper ionosphere, Proc. Phys. Soc. London, 68B, 493-503.

Spiegel, E. A., and G. Veronis (1960). On the Boussinesq approximation for a compressible fluid, Astrophys. J., 131, 442-447.

Stevenson, D. J. (1980). Saturn's luminosity and magnetism, Science, 208, 746-748.

Stone, E. C., and A. L. Lane (1979a). Voyager 1 encounter with the Jovian system, Science, 204, 945-948.

Stone, E. C., and A. L. Lane (1979b). Voyager 2 encounter with the Jovian system, Science, 206, 925-927.

Stone, E. C., and E. D. Miner (1981). Voyager 1 encounter with the Saturnian system, Science, 212, 159-163.

Stone, E. C., and E. D. Miner (1982). Voyager 2 encounter with the Saturnian system, Science, 215, 499-504.

Stull, R. B. (1976). Internal gravity waves generated by penetrative convection, J. Atmos. Sci., 33, 1279-1286.

Tatarskii, V. I. (1971). The Effects of the Turbulent Atmosphere on Wave Propagation, translated from Russian, National Technical Information Service, Springfield, Va.

Turner, J. S. (1973). Buoyancy Effects in Fluids, Cambridge Univ. Press, Cambridge.

Tyler, G. L., and H. T. Howard (1969). Refractivity of carbon dioxide under simulated Martian conditions, Radio Sci., 4, 899-904.

Tyler, G. L., V. R. Eshleman, J. D. Anderson, G. S. Levy, G. F. Lindal, G. E. Wood and T. A. Croft (1981a). Radio science investigations of the Saturn system with Voyager 1: Preliminary results, Science, 212, 201-206.

Tyler, G. L., J. F. Vesecky, M. A. Plume, H. T. Howard, and A. Barnes (1981b). Radio wave scattering observations of the solar corona: First-order measurements of expansion velocity and turbulence spectrum using Viking and Mariner 10 spacecraft, Astrophys. J., 249, 318-332.

Tyler, G. L., V. R. Eshleman, J. D. Anderson, G. S. Levy, G. F. Lindal, G. E. Wood, and T. A. Croft (1982). Radio science with Voyager 2 at Saturn: Atmosphere and ionosphere and the masses of Mimas, Tethys, and Iapetus, Science, 215, 553-558.

Uscinski, B. J. (1977). The Elements of Wave Propagation in Random Media, McGraw-Hill, New York.

Vargaftik, N. B. (1975). Tables on the Thermophysical Properties of Liquids and Gases, second ed., Wiley, New York.

Vinnichenko, N. K. (1970). The kinetic energy spectrum in the free atmosphere: 1 second to 5 years, Tellus, 22, 158-166.

Wallace, J. M. (1973). General circulation of the tropical lower stratosphere, Rev. Geophys. Space Phys., 11, 191-222.

Warwick, J. W., J. B. Pearce, A. C. Riddle, J. K. Alexander, M. D. Desch, M. L. Kaiser, J. R. Thieman, T. D. Carr, S. Gulkis, A. Boischot, C. C. Harvey, and B. M. Pedersen (1979a). Voyager 1 planetary radio astronomy observations near Jupiter, Science, 204, 995-998.

Warwick, J. W., J. B. Pearce, A. C. Riddle, J. K. Alexander, M. D. Desch, M. L. Kaiser, J. R. Thieman, T. D. Carr, S. Gulkis, A. Boischot, Y. Leblanc, B. M. Pedersen, and D. H. Staelin (1979b). Planetary radio astronomy observations from Voyager 2 near Jupiter, Science, 206, 991-995.

Warwick, J. W., J. B. Pearch, D. R. Evans, T. D. Carr, J. J. Schauble, J. K. Alexander, M. L. Kaiser, M. D. Desch, M. Pedersen, A. Lecacheux, G. Daigne, A. Boischot, and C. H. Barrow (1981). Planetary radio astronomy observations from Voyager 1 near Saturn, Science, 212, 239-243.

Warwick, J. W., D. R. Evans, J. H. Romig, J. K. Alexander, M. D. Desch, M. L. Kaiser, M. Aubier, Y. Leblanc, A. Lecacheux, and B. M. Pedersen (1982). Planetary radio astronomy observations from Voyager 2 near Saturn, Science, 215, 582-587.

Woo, R., and J. W. Armstrong (1980). Spectral broadening measurements of the ionospheres of Jupiter and Saturn, Nature, 287, 309-311.

Woo, R., J. W. Armstrong, and A. Ishimaru (1980a). Radio occultation measurements of turbulence in the Venus atmosphere by Pioneer Venus, J. Geophys. Res., 85, 8031-8038.

Woo, R., J. W. Armstrong, and A. J. Kliore (1982). Small-scale turbulence in the atmosphere of Venus, Icarus, 52, 335-345.

Woo, R., A. Ishimaru, and F.-C. Yang (1980b). Radio scintillations during occultations by turbulent planetary atmospheres, Radio Sci., 15, 695-703.

Woo, R., and F.-C. Yang (1976). Measurements of electron density irregularities in the ionosphere of Jupiter by Pioneer 10, J. Geophys. Res., 81, 3417-3422.

Woo, R., and F.-C. Yang (1978). Measurements of the magnetic field orientation in the Jovian ionosphere deduced from Pioneer 10 and 11 scintillation observations, J. Geophys. Res., 83, 5245-5255.

Yaglom, A. M. (1962). Introduction to the Theory of Stationary Random Functions, Dover, New York.

Yeh, K. C., and C.-H. Liu (1982). Radio wave scintillations in the ionosphere, Proc. IEEE, 70, 324-360.

Young, A. T. (1976). Scintillations during occultations by planets: I. An approximate theory, Icarus, 27, 335-357.